Polygonal planforms and phyllotaxis on plants

P.D. Shipman*, A.C. Newell

Department of Mathematics, University of Arizona, Tucson, AZ 85721, USA

Abstract

We demonstrate how phyllotaxis (the arrangement of leaves on plants) and the ribbed, hexagonal, or parallelogram planforms on plants can be understood as the energy-minimizing buckling pattern of a compressed sheet (the plant's tunica) on an elastic foundation. The key idea is that the elastic energy is minimized by configurations consisting of special triads of periodic deformations. We study the conditions that lead to continuous or discontinuous transitions between patterns, state testable predictions, and suggest experiments to test the theory.
© 2005 Elsevier Ltd. All rights reserved.

Keywords: Phyllotaxis; Pattern formation; Biomechanics

1. Introduction and overview

1.1. Overview

Our goal is to understand the processes that lead to polygonal planforms and phyllotaxis on plants. In this overview, we set out the main ideas in a narrative form which uses a minimum amount of mathematical jargon and symbols. In the subsequent sections, we supply a historical and descriptive background of the challenge, the reasons behind our choice of model, a more detailed analysis of the model, support for the key ideas introduced in this overview, and a discussion of what one can reasonably conclude. This work is the promised extension of the ideas first presented in Shipman and Newell (2004).

We use the term *polygonal planform* to connote the tiling of the plant surface into irregular polygons which are usually manifested as ribs, parallelograms, hexagons,

and what we call staircase parallelograms. These cases are illustrated in Fig. 1. Plant phyllotaxis refers to the arrangement (*taxis*) of phylla (leaves, florets, bracts on a pinecone, or stickers) on the plant surface. In Fig. 2(a), we show such an arrangement where the phylla, located at the maxima in the surface deformation, all lie on three families of spirals, three clockwise, five anticlockwise, and eight slightly clockwise, but almost radial. The fact that the integers 3, 5, 8 happen to be a sequential triplet in the Fibonacci sequence 1, 1, 2, 3, 5, 8, 13, ... is no accident. The occurrences of Fibonacci sequences in plants has intrigued natural scientists since the time of Kepler.

As the plant grows, the pattern will change. Indeed, we will find that one important parameter is a non-dimensional measure of the plant's radius, which we call Γ. In Fig. 9 we illustrate transitions between patterns on plants. Some plants, as they grow, will follow a regular Fibonacci sequence such as $(2, 3, 5) \rightarrow (3, 5, 8) \rightarrow (5, 8, 13) \rightarrow (8, 13, 21) \rightarrow \cdots$ (Fig. 9(c–f)). Other plants will follow a non-Fibonacci sequence such as $(2, 3, 5) \rightarrow (3, 3, 6) \rightarrow (3, 4, 7) \rightarrow \cdots$ (Fig. 9(a and b)). We would like to understand what circumstances lead to the different kinds of transitions.

Transitions come in four potential types. The first two types involve what physicists call a first-order (I) phase

*Corresponding author. Present address: Max Planck Institut für Mathematik in den Naturwissenschaften, Inselstrasse 22, 04103 Leipzig, Germany. Tel.: +49 341 9959 861; fax: +49 341 9959 658.

E-mail addresses: schiffmann@mis.mpg.de (P.D. Shipman), anewell@math.arizona.edu (A.C. Newell).

transition, where some parameter (called an order parameter), which measures the shape of the pattern, undergoes a sudden and discontinuous change. If that change involves a transition from one triad to another in which only one integer is shared (e.g. $(2, 3, 5) \rightarrow (3, 3, 6)$) we denote the transition as (I,1). If the triads share two integers, we call the transition (I,2). In a plant which undergoes a first-order (sudden) phase transition, we

Fig. 1. (a) Ribs on a saguaro cactus, (b) hexagons on a pine cone, (c) parallelograms on a cactus, and (d) staircase parallelograms on a cactus.

will observe the different states will be separated by point singularities. The second type of phase transition, called a second-order phase transition (II) is one in which the order parameter changes continuously as the plant size Γ increases, although its rate of change with respect to Γ will usually be discontinuous. If the transition between two triads is continuous and shares two integers, we denote it as (II,2). Transitions of type (II,1) seem not to be observed and those of type (I,2) are rare. There are circumstances, such as the presence of prior bias (called geometric imperfection by Koiter (1963)), in which second-order phase transitions can be smooth, namely involve no discontinuity in the rate of change. The idea is simple to explain. Suppose that one were to compress a beam along its vertical axis and constrain any deformation to be planar. Think of the beam as having a rectangular cross section, with one side much longer than the other. At sufficient loading, the compressed beam will become unstable and bow to the left or to the right. If there is no initial bias, either direction is equally likely. But, if the beam is slightly bowed to begin with, say to the left, then the leftward deformation will be amplified continuously as soon as the load is applied, although the amplification will accelerate significantly near the critical buckling load, namely that load at which the uniformly compressed beam becomes unstable to a left or right deflection in the unbiased case. Bias will be one of the important ingredients in our overall picture.

In recent years, there have been two directions of inquiry which have attempted to provide quantitative rationales for plant phyllotaxis. These are discussed in detail in Section 2; here, we sketch the main ideas and
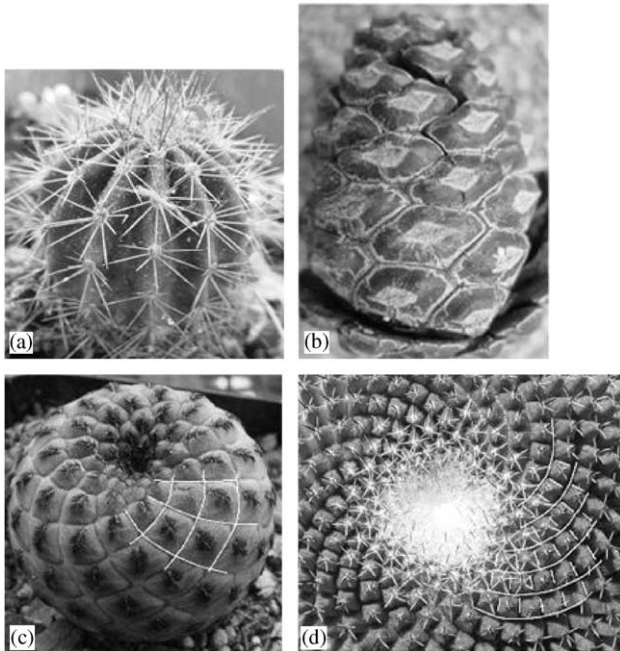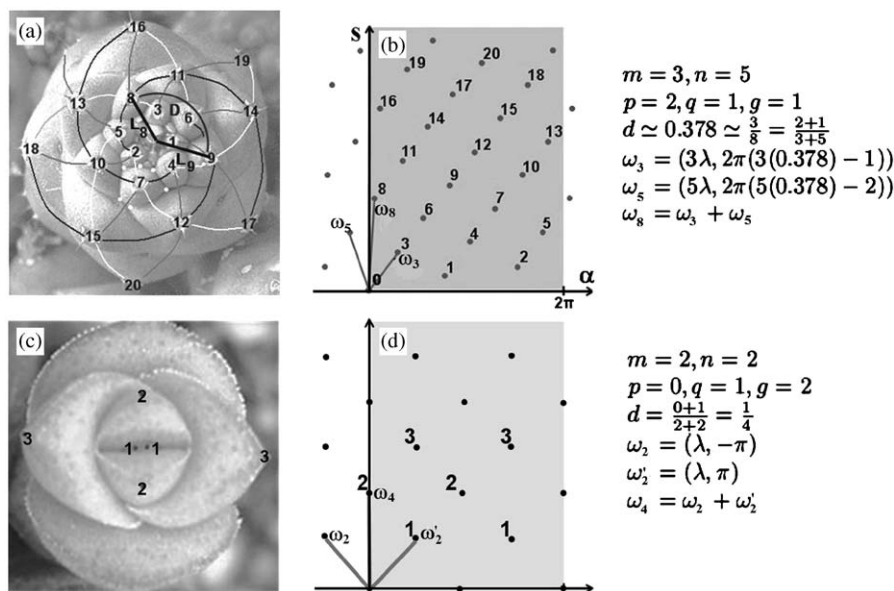

Fig. 2. The phylla of the cactus (a) and succulent (c) are numbered according to their distance from the center. (b,d) In radial s and angular α coordinates, the numbered points form lattices.

the roles they have had in our thinking. In a series of papers in the 1990s, Douady and Couder (1992, 1996a–c) (DC), motivated by the rules of Hofmeister (1868) of a century before, created an ingenious magneto-mechanical paradigm accessible to experiment. The experiment involved configurations of mutually repelling dipoles introduced at regular intervals to the pattern in an applied magnetic field which meant that the dipole, once placed, would travel radially outwards at an exponential rate. DC showed how energy-minimizing configurations followed Fibonacci rules. The second direction of inquiry was pioneered by the late Paul Green and colleagues C. Steele, J. Dumais, S. Rennich and L. Hernández (GSDRH) at Stanford. Their idea was that compressive stresses are set up due to differential growth in the plant's tunica (the skin) and its corpus (the squishy fibrous material of the body). They argued that these stresses, more circumferential than radial, are sufficiently large in an annular region circumscribing the plant's shoot apical meristem (SAM) to cause buckling of the tunica. Their picture was that the buckling configuration would give rise to the plant's pattern. However, their model only exhibited patterns similar to those observed when they forced the boundaries in special ways (Green et al., 1998).

The model we suggest was informed and inspired by both of these approaches. On the one hand, we agree with GSDRH that induced mechanical forces and compressive stresses are the mechanisms for producing plant surface deformations near the SAM. What we suggest that is new, however, and how our idea connects with that of DC, is that the observed plant patterns and phyllotaxis occur naturally, intrinsically, as those deformations which minimize the elastic energy of the annular region of the tunica supported by the corpus, which plays the role of an elastic foundation. These deformations will form naturally, independent of boundary conditions. The key realization, and a fact known to Koiter (1963) many years ago, is that the shapes of surface deformations of curved elastic shells on elastic foundations are determined to a large extent by quadratic nonlinear interactions in the Föppl–von Kármán–Donnell (FvKD) equations. These terms emerge from the strain energy of the shell and, in particular, from terms which are cubic in the amplitude of the deformation and arise as the product of the Airy stress F (a tensor potential for the in-plane stresses) and the Gaussian curvature, which is quadratic in the normal deformation w to the surface.

The argument in its simplest form goes like this. If the annulus is big enough (the jargon is *spatially extended*) so that the ratios of its width and circumference to the intrinsic buckling wavelength are large, then deformations $w(r, \alpha)$ (r radial, α circumferential coordinates) can be written as linear combinations of periodic functions

(cosines) in the form

$$\omega(r, \alpha) = \sum a(l, m) \cos(lr + m\alpha), \tag{1}$$

where the summation goes over all vectors $\vec{k} = (l, m)$ which live in the active set, and the circumferential wavenumber m is an integer. The active set is the set of all such shapes which are either amplified or only weakly damped. Quadratic products of such terms will produce cosines and sines of sums and differences of the phases, namely $(\pm l_1 \pm l_2)r + (\pm m_1 \pm m_2)\alpha$. Most of these new shapes will be heavily damped, but a few will belong to the active set. This leads to the identification of wavevector triplets

$$\vec{k}_m = (l_m, m), \quad \vec{k}_n = (l_n, n),$$
$$\vec{k}_{m+n} = \vec{k}_m + \vec{k}_n = (l_m + l_n, m + n), \tag{2}$$

each of which belongs to the active set, which strongly reinforce each other. For plants, it turns out that the magnitudes of these quadratic interactions is directly proportional to C, a non-dimensional measure of the curvatures of the tunica surface before buckling. It is such interactions which are responsible for the appearance of hexagonal planforms near the threshold of instability in many pattern-forming systems (which share the common symmetry of rotational invariance) from convection in the horizontal layers of fluids (Busse, 1967) to the buckling patterns seen on collapsing spherical shells subject to radial inward pressure (Lange and Newell, 1971, 1974). For these situations, the magnitude of the quadratic interaction is directly proportional to a parameter which measures how close the system is to an up-down ($\omega \to -\omega$) symmetry. The further from this symmetry that the system is, the stronger is the quadratic interaction. In our model, this distance is measured by C.

The first key idea is that deformations $\omega(r, \alpha)$ of the tunica surface consist of linear combinations of triads or sets of triads whose normal deformation $\omega(r, \alpha)$ is given by

$$\omega(r, \alpha) = \sum (a_m \cos(l_m r + m\alpha) + a_n \cos(l_n r + n\alpha)$$
$$+ a_{m+n} \cos((l_m + l_n)r + (m + n)\alpha)), \tag{3}$$

where the symbol $\sum$ denotes that there may be more than one such set. Already we see a hint of Fibonacci rules. The circumferential wavenumbers $m, n, m + n$, namely the numbers of spiral arms in the deformation (3), add according to the Fibonacci rule $(m) + (n) = m + n$. But, of course, this is not the whole story, because, for example, $2 + 5 = 7$ and $(2, 5, 7)$ is not a triplet in the regular Fibonacci sequence.

The second key idea uses the fact that, for reasons we discuss in Section 2, the circumferential stress in the annular region is larger than the radial stress. Therefore, when the stress exceeds a critical value, the most unstable shape is purely circumferential, with

wavevector $\vec{k} = (O, \Gamma)$, where Γ, you recall, is the radius of the annular region. Now, it could be that the shape $\cos(\Gamma\alpha)$ simply grows until it reaches a saturation level determined, for example, by the hard spring properties of the plant's corpus. However, for situations in which quadratic products are important, this configuration is unstable to an r-dependent deformation which consists of modes with wavevectors

$$\vec{k}_m = (-l, m), \quad \vec{k}_n = (l, n), \quad \vec{k}_{m+n} = (0, m+n),$$

where $m + n \simeq \Gamma$. So, for plants whose tunicas in the compressed region have large values of C—that is, large curvature—the purely circumferential mode gives way to a deformation involving a triad of modes. For low-C plants, such as the saguaro cactus, the quadratic terms are small and circumferential ridges dominate the pattern.

For simplicity of argument, let us take Γ to be an integer. If $\Gamma = 2N$, then we show that the energy associated with the deformation $w = a_m \cos(-lr + m\alpha) + a_n \cos(lr + n\alpha) + a_{m+n} \cos(2N\alpha)$ is minimized at the choices $m = n = N$, the radial wavenumber l is a chosen value of order one and the amplitudes are roughly equal. Such deformations look roughly hexagonal (see Fig. 5(b)). For $\Gamma = 2N + 1$, the corresponding radial wavenumber and amplitudes are approximately the same, but this time $m = N$ and $n = N + 1$. So, imagine that we begin with $\Gamma = 2N$ and denote the resulting energy-minimizing deformation by its circumferential wavenumber triplet $(N, N, 2N)$. Such objects are known as N-whorls, the most prevalent of which in nature is the 2-whorl (or *decussate*) pattern. As the plant size increases (we will imagine it does this in integer steps) to $2N + 1$, the N-whorl $(N, N, 2N)$ will undergo a (I,1) transition to a $(N, N + 1, 2N + 1)$-spiral pattern. For example, it is often observed that an alternating 2-whorl $(2,2,4)$ becomes a $(2, 3, 5)$ pattern whose phylla lie on families of two, three, or five spirals. The question is: what happens next? What happens as Γ increases beyond $2N + 1$ (here 5)?

The third key idea draws on observations of what actually happens as a plant grows. Its tunica (skin) grows because of new material emanating from the SAM. As it moves away from the SAM, it hardens (a process which may also add to the induced stress) and buckling takes place in an annular hardened region. The rates at which the tunica spreads and at which the overall plant grows may be different. If the former is larger, then the buckled pattern formed in the annular region moves radially outwards relative to the growing plant (and the radial distance Γ to the center of the compressed band) into a subcritically compressed region. Subsequent buckling in the compressed region will be different. Firstly, the plant size Γ is larger, so, potentially, slightly different shapes can be amplified. Secondly, there is bias because the previously produced pattern, which is now on the outer fringes of the

buckling region, will discriminate amongst several possible choices of minimizing configurations for the next buckling pattern. The key again is quadratic interactions. Suppose the $(N, N + 1, 2N + 1)$ pattern has moved to the outer fringe of the new buckling region. The possible quadratic interactions will produce the following possibilities: (i) $N + (N + 1) = 2N + 1$, which is already present; (ii) $N + (2N + 1) = 3N + 1$, and (iii) $(N + 1) + (2N + 1) = 3N + 2$. What we show is that, of the latter two possibilities, (iii) is more important. The reasons for this depend on the structure of the parameters $\sigma(l, m)$, $\tau(m, n, m + n)$ of our model, which measure linear growth and the strength of quadratic interactions. For simplicity, let us look at which modes in a $\{2, 3, 5, 7 = 2 + 5, 8 = 3 + 5\}$-sequence will lead to energy minimization. The quadratic interaction producing the 7 involves the product $a_2 a_5$, but, at this stage, the 2-mode is already quite heavily damped. Also, its coefficient $\tau(2, 5, 7)$ peaks at a different radial wavenumber than does $\tau(3, 5, 8)$, which multiplies the product $a_3 a_5$. The upshot is that the latter wins. The new energy-minimizing configuration will be a linear combination of the four modes with circumferential wavenumbers N, $N + 1$, $2N + 1$ and $3N + 2$ with appropriately chosen amplitudes and radial wavenumbers. As Γ continues to increase, and as this configuration moves to the outer edge of the pattern-generating region, it will provide a bias for the next buckling pattern. The bias will favor the existing modes with circumferential wavenumbers $N, N + 1, 2N + 1, 3N + 2$ which are already present, and the new possibilities $3N + 1$, $4N + 2$, $4N + 3$ and $5N + 3$. For reasons similar to those given earlier for choosing the $3N + 2$ ($= 8$ for $N = 2$) mode over the $3N + 1$ mode, it is the last, namely $5N + 3$, which enters the next energy-minimizing buckling configuration. This is exactly the recipe for the regular Fibonacci sequence. The preferred next circumferential wavenumber to be excited as Γ increases is the sum of the last two. Continuing this rule, we obtain that, as the plant grows, its dominant circumferential (spiral) wavenumbers run through the Fibonacci sequence $\{N, N + 1, 2N + 1, 3N + 2, \ldots, f_{n+1}N + f_n\}$, where f_n is the nth Fibonacci number. We shall also see in Section 4 that this leads to a choice of golden divergence angle.

Moreover, our analysis allows us to compute more than energy minima. This is important because there are typically many minima in the energy landscape function and the task is to determine not just which states minimize the energy, but which among them can be dynamically realized beginning from various configurations. What we find is that the minimum realized is not always the one with lowest energy, but the one in whose basin of attraction the starting configuration lies; this is a point which Douady and Couder (1996b, c) also make. We can follow the dynamics by solving the

time-dependent amplitude equations for the modes involved; we include the effects of bias by adding to those equations calculable constants. Using this approach, one can readily see why it is that the system tends to land in the minima corresponding to circumferential wavenumbers of the Fibonacci sequence.

Consider next the envelope of corresponding amplitudes

$$\{a_N, a_{N+1}, a_{2N+1}, a_{3N+2}, a_{5N+3}, \ldots, a_{f_{n+1}N+f_n}\} \tag{4}$$

as Γ grows. At first, the envelope is supported on the first three, i.e. $a_N \simeq a_{N+1} \simeq a_{2N+1}$, and $a_r \simeq 0$ for $r > 2N + 1$. This leads to irregular hexagonal shapes. As we move up the sequence, however, the envelope is more likely to contain four or five non-zero amplitudes; this will produce parallelogram or staircase-parallelogram planforms. For reasons that we shall later explain, it is unlikely for the envelope to support more than five sequential modes at any one value of Γ. In fact, the shape of the envelope is more or less the same for all $\Gamma \geqslant 5$ (see Fig. 4).

This analysis assumes, of course, that the quadratic coefficient $\tau(m, n, m + n)$ which is proportional to the original tunica curvature C, is of order one. For C very small, the triads are ridge-dominated, and the plant evolves by adding a new ridge every time Γ increases by an integer. The dislocations joining these ridge patterns can be seen on all saguaro cacti.

In summary, then, the template which forms the patterned surface of plants is provided by the buckling of a compressed and curved annular region of the tunica near the SAM into its intrinsic energy-minimizing configurations. The normal deformation to the plant surface consists of linear combinations of overlapping triads of cosines with phases $lr + m\alpha$, where the sequence of chosen circumferential wavenumbers m often follows Fibonacci rules, and where radial wavenumbers also follow a triad addition rule $l_{n+2} = l_n + l_{n+1}$.

But, a glance at a mature plant will show that the story cannot end there. The primordia (bumps) and phylla (stickers) at their maxima are far larger than the tunica skin thickness which, according to the buckling shell theory, is the magnitude of the surface deformation. To reach the mature state, we surmise that the plant pattern which has moved away from the compressed region undergoes further growth due to the combined influences of local stress and local growth. We shall show that, after buckling, the stress field is non-uniform and largest at the maxima of the surface deformation. It is documented that there is a close and symbiotic relationship between growth and stress in plants; thus, we suggest that this extra local stress will lead to a non-uniform distribution of the growth hormone auxin and lead to a local amplification of the deformations. This, in turn, will increase the stress there and create an even more non-uniform distribution of

auxin. But, we emphasize again that the character of the deformation has already been set by mechanical forces.

Before going into more details, it is important to emphasize another crucial point. Patterns are macroscopic objects whose behaviors are governed more by common symmetries that systems share and less by their microscopic details. Pattern textures, both the planforms (ribs, hexagons, parallelograms) and their defects (dislocations, penta–hepta pairs) are canonical and universal. For this reason, one has to be careful about falling victim to looks-like science. Any microscopic model we might propose to explain plant patterns which shares the overall symmetry properties of the model we shall introduce will produce macroscopically similar results. Therefore, we must be cautious about making the inference that because our model produces patterns which appear to have a similar character to those observed, it must be correct. What we have to do is to look at the details. In our case, the signatures of the microscopic model are contained in the growth rate $\sigma(l, m)$ and quadratic coupling coefficient $\tau(m, n, m + n)$. It is their structures, peculiar to our elastic buckling model, and their dependence on plant size and curvature, which make our case plausible.

1.2. Phyllotactic parameters and coordinates: The physical and Fourier space dual lattices

In the previous section, we described both the positions of phylla on the plant surface and the polygonal tiling of the plant surface. The purpose of this section is to develop natural coordinates in which to state the positions of phylla, and then to establish the relationship to the polygonal shapes.

In Figs. 2(a and c), phylla are numbered according to their distance from the centers of the plants. This allows us to illustrate the following three standard parameters used to describe phyllotactic patterns:

1. *The whorl number g*: Each phyllo on a plant is a member of a whorl of g phylla that are evenly spaced about a circle centered at the center of the plant. The number g is locally constant. For the example of Fig. 2(c), $g = 2$, as one sees pairs of phylla that are equidistant from the center of the plant. For the cactus of Fig. 2(a), $g = 1$.
2. *The divergence angle $D = 2\pi d$*: The angle between consecutively numbered phylla is taken to be the angle between the rays from the center of the plant to the centers of those phylla; see Fig. 2(a). It is an observation that the angle between any two consecutively numbered phylla is locally constant on any plant; this constant is called the *divergence angle*, $D = 2\pi d$. There is a natural ambiguity in the measurement of the angle, as one can either measure clockwise or counterclockwise. If the two measurements are not

equal, the plant shows a *handedness* and $D = 2\pi d$ is taken to be the smaller of the two measurements; thus, $0 < d \leqslant \frac{1}{2}$. In our Fig. 2(a) example, the divergence angle is roughly $D = 2\pi(0.382)$ measured clockwise, and for the example of Fig. 2(c), $D = \frac{2\pi}{4}$ measured either counterclockwise or clockwise.

3. *The plastochrone ratio* λ: Call the length of the ray from the center of the plant to the center of the nth-numbered phyllo L_n; see Fig. 2(b). The standard claim of the phyllotactic literature is that on most plants, at least for phylla close the center, the ratio $\frac{L_{n+1}}{L_n}$ is locally independent of n. That ratio is called the *plastochrone ratio*. It seems that on many cacti it is the difference $L_{n+1} - L_n$ that is constant. For such plants that difference we shall call the *plastochrone difference*. We will denote this parameter by λ.

The observations leading to parameters g, d and λ tell us that the arrangement of phylla on plants is a lattice. To see this pictorially, put radial and angular coordinates (r, α) on the cactus of Fig. 2 and then transfer the result to Fig. 2(b), where dots represent the centers of phylla, and the vertical axis is $s = \log(r)$ if the plant exhibits the plastochrone ratio and $s = r$ if the plant exhibits the plastochrone difference. We choose the direction of increasing α to be the direction determined by the clockwise or counterclockwise handedness. If the plant has whorl number g, divergence angle $D = 2\pi d$ and plastochrone ratio λ, in the (s, α)-plane the plant's phylla are part of a lattice $\Omega(\vec{\omega}_{\lambda,d}, \vec{\omega}_g)$ that is the integer span of the vectors $\vec{\omega}_{\lambda,d} = (\lambda, 2\pi d)$ and $\vec{\omega}_g = (0, \frac{2\pi}{g})$ where λ equals $\log(\lambda)$ or λ if λ is a plastochrone ratio or difference, respectively. The bases of $\Omega(\vec{\omega}_{\lambda,d}, \vec{\omega}_g)$ are exactly the linear combinations

$$\alpha\vec{\omega}_{\lambda,d} + \beta\vec{\omega}_g = \left(\alpha\lambda, 2\pi\left(d\alpha + \frac{\beta}{g}\right)\right)$$
$$= \frac{1}{g}(g\alpha\lambda, 2\pi(g\alpha d + \beta)),$$

$$\gamma\vec{\omega}_{\lambda,d} + \delta\vec{\omega}_g = \left(\gamma\lambda, 2\pi\left(d\gamma + \frac{\delta}{g}\right)\right)$$
$$= \frac{1}{g}(g\gamma\lambda, 2\pi(g\gamma d + \delta)), \tag{5}$$

where α, β, γ, and δ are integers such that $\alpha\delta - \beta\gamma = \pm 1$. Setting $m \doteq g\alpha$, $n \doteq g\gamma$, $p \doteq \delta$, $q \doteq \beta$, we have that all of the bases of the lattice $\Omega(\vec{\omega}_{\lambda,d}, \vec{\omega}_g)$ are given by

$$\vec{\omega}_m = \frac{1}{g}(m\lambda, 2\pi(md - q)),$$

$$\vec{\omega}_n = \frac{1}{g}(n\lambda, 2\pi(nd - p)), \tag{6}$$

where m, n, p, q are any integers such that $pm - qn = \pm g = \pm\gcd(m, n)$; $\gcd(m, n)$ means the greatest common divisor of m and n.
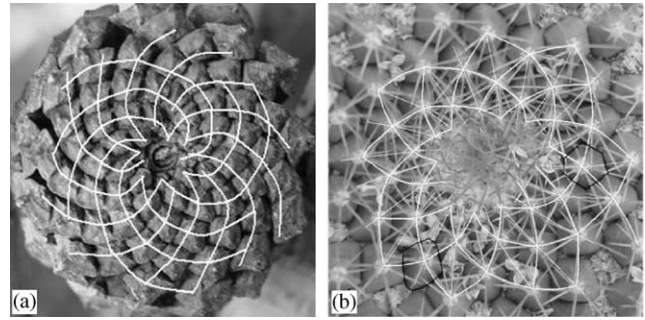

Fig. 3. (a) Parallelograms on a pine cone giving families of 8 counterclockwise and 13 clockwise spirals. (b) Hexagons on a cactus, giving familes of 8 counterclockwise and 13 clockwise spirals, and a third family of $21 = 8 + 13$ counterclockwise spirals (marked by thinner lines).

There are an infinite number of possible choices for (m, n) that give generators (6) for a lattice determined by g, d and λ. Typically, however, there is a natural choice for a given plant; this choice is called the *parastichy pair*. Consider, for example, the pine cone in Fig. 3(a). The white lines connect the centers of bracts that touch each other. Each bract is parallelogram-shaped and touches four other bracts; one thus obtains two families of spirals, (eight) 13 emanating (counter)clockwise from the center of the cone. With the choice of $d \simeq 0.378$, we choose $m = 8, n = 13$ in stating the lattice generators and say that the cone exhibits the parastichy pair $(8, 13)$. The lattice generators describing the plant's phyllotaxis are thus

$$\vec{\omega}_8 = (8\lambda, 2\pi(8d - 3)),$$
$$\vec{\omega}_{13} = (13\lambda, 2\pi(13d - 5)) \tag{7}$$

with $d \simeq 0.378$. Now consider the cactus of Fig. 3(b). In this case, the plant is tiled by hexagons, and there are thus three families of spirals that connect neighboring groups of stickers (called *aeroles*). Thus, we will describe the plant with *three* generators

$$\vec{\omega}_8 = (8\lambda, 2\pi(8d - 3)),$$
$$\vec{\omega}_{13} = (13\lambda, 2\pi(13d - 5)),$$
$$\vec{\omega}_{21} = (21\lambda, 2\pi(21d - 8)), \tag{8}$$

where again $d \simeq 0.378$. Looking closely at the pine cone of Fig. 3(a), seen again in Fig. 4, one notices that besides the strongly marked families of 8 clockwise and 13 counterclockwise spirals that mark out the parallelograms, ridges along the diagonals of each bract mark out families of $5 = 13 - 8$ counterclockwise and $21 = 13 + 8$ clockwise spirals. Thus, one may desire to state instead of just the two generators (7), the four lattice generators $\vec{\omega}_5 = \vec{\omega}_{13} - \vec{\omega}_8$, $\vec{\omega}_8$, $\vec{\omega}_{13}$, and $\vec{\omega}_{21} = \vec{\omega}_8 + \vec{\omega}_{13}$; the shape of the bracts, however, indicates that the two vectors $\vec{\omega}_5$ and $\vec{\omega}_{21}$ have somewhat less weight than their middle colleagues.

The discussion has thus led us to a description of the *shape* of the plant surface deformations and a need to assign weights to the descriptive lattice generators. To further establish the connection between the shapes and positions of phylla, examine Fig. 5, where functions of the form

$$\omega(s, \alpha) = \sum_{j=1}^{N} a_j \cos(\vec{k}_j \cdot \vec{x}) \tag{9}$$

for wavevectors $\vec{k}_j = (l_j, m_j)$, $\vec{x} = (s, \alpha)$ and $\vec{k}_j \cdot \vec{x} = l_j s + m_j \alpha$ are plotted for various choices of the amplitudes a_j and wavevectors $\vec{k}_j$. We will show in Section 4 how our model dictates the choices of wavevectors and corresponding values of the amplitudes; we will find that

(i) patterns with dominant ridges are produced by a sum $\omega(s, \alpha) = \sum_{j=1}^{3} a_j \cos(\vec{k}_j \cdot \vec{x})$ in which $\vec{k}_1 + \vec{k}_2 = \vec{k}_3$ and $a_3 > a_1 \simeq a_2$ (Fig. 5(a)),

(ii) hexagonal planforms are produced by a sum $\omega(s, \alpha) = \sum_{j=1}^{3} a_j \cos(\vec{k}_j \cdot \vec{x})$ in which $\vec{k}_1 + \vec{k}_2 = \vec{k}_3$ and all amplitudes a_j are approximately equal (Fig. 5(b)),

(iii) parallelogram planforms are produced by a sum $\omega(s, \alpha) = \sum_{j=1}^{4} a_j \cos(\vec{k}_j \cdot \vec{x})$ in which $\vec{k}_1 + \vec{k}_2 = \vec{k}_3$, $\vec{k}_2 + \vec{k}_3 = \vec{k}_4$ and $a_1 \simeq a_4 < a_2 \simeq a_3$ (Fig. 5(c)), and

(iv) staircase parallelogram planforms are produced by a sum $\omega(s, \alpha) = \sum_{j=1}^{5} a_j \cos(\vec{k}_j \cdot \vec{x})$ in which $\vec{k}_1 + \vec{k}_2 = \vec{k}_3$, $\vec{k}_2 + \vec{k}_3 = \vec{k}_4$, $\vec{k}_3 + \vec{k}_4 = \vec{k}_5$, and $a_1 \simeq a_5 < a_2 \simeq a_4 < a_5$ (Fig. 5(d)).

For each of the functions plotted in Fig. 5, the wavevectors $\vec{k}_j$ are integer combinations of two wavevectors $\vec{k}_m = (l_m, m)$ and $\vec{k}_n = (l_n, n)$, and the maxima of each function lie on a lattice determined by the choice of $\vec{k}_m, \vec{k}_n$. Indeed, the maxima of Eq. (9) lie at the intersections of the families of the lines in the (s, α)-plane (spirals in the (x, y)-plane) $l_m s + m\alpha = 2\pi Q$, $l_n s + n\alpha = 2\pi P$, where P and Q are integers; that is, the maxima lie at the points

$$(s, \alpha) = P\vec{\omega}'_m - Q\vec{\omega}'_n$$
$$= \frac{2\pi}{nl_m - ml_n} (Pm - Qn, Pl_n - Ql_m), \tag{10}$$

where

$$\vec{\omega}'_m = \frac{2\pi}{nl_m - ml_n} (m, l_m), \quad \vec{\omega}'_n = \frac{2\pi}{nl_m - ml_n} (n, l_n). \tag{11}$$

The numbered points in Fig. 2(b) correspond to the maxima of the plant in Fig. 2(a) and therefore to the points (10). Fig. 6 demonstrates the description of the plant in Fig. 2 as a sum of the form (9) and the lattice (10) in the (s, α) plane. To establish the relationship between l_m and l_n and the phyllotactic coordinates g, d, λ, we solve $\vec{\omega}'_m = \vec{\omega}_m$ and $\vec{\omega}'_n = \vec{\omega}_n$, where $\vec{\omega}_m, \vec{\omega}_n$ are given by Eq. (6), for l_m and l_n and obtain that

$$l_m = \frac{2\pi}{\lambda} (q - md), \quad l_n = \frac{2\pi}{\lambda} (p - nd),$$
$$nl_m - ml_n = \frac{2\pi g}{\lambda}. \tag{12}$$

Fig. 4. Besides the families of 8 counterclockwise and 13 clockwise spirals marked in (a), one notes ridges along the diagonals of the parallelogram-shaped bracts. These mark out families of $13 - 8 = 5$ clockwise and $8 + 13 = 21$ counterclockwise spirals.
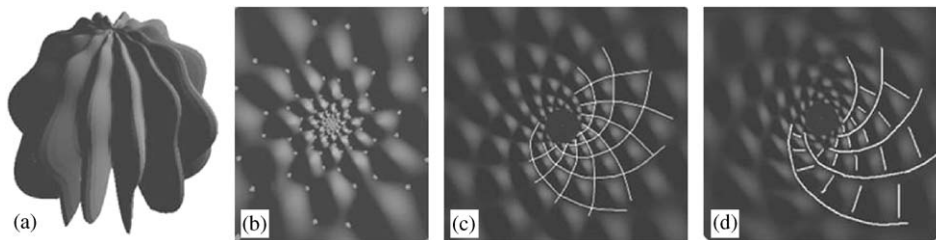
Fig. 5. A preview of the results of Section 4. (a) The result of the experiment of Fig. 22 gives a configuration in which only one amplitude in a function of the form (9) is large; this results in a rib pattern. (b) The result of Section 4.4 gives a hexagonal pattern when three amplitudes of (9) are large. (c,d) The results of the experiment of Fig. 21 show (c) a parallelogram planform when four amplitudes of (9) are large or (d) a staircase parallelogram planform when five amplitudes of (9) are large.

(a)

(b)
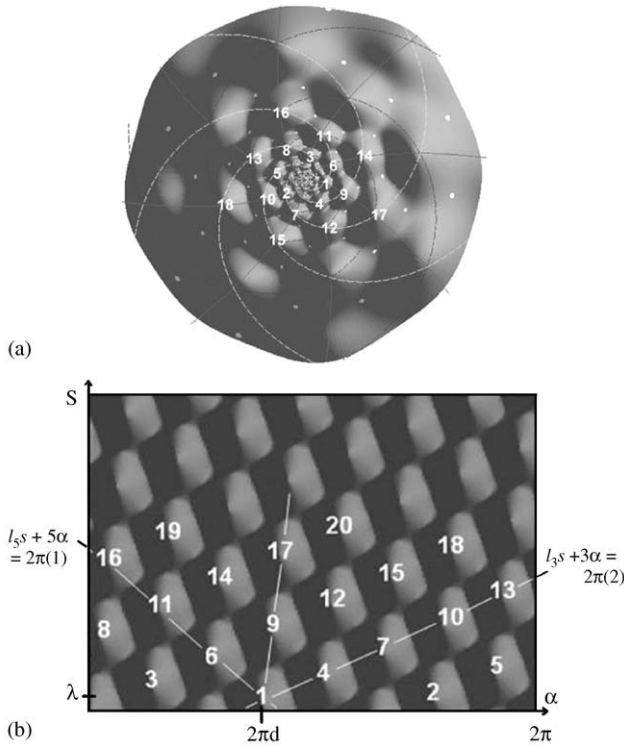
Fig. 6. (a) A deformation of the sphere given by the function $w(r, \alpha) = a_3 \cos(l_3 \ln(r) + 3\alpha) + a_5 \cos(l_5 \ln(r) + 5\alpha) + a_8 \cos(l_8 \ln(r) + 8\alpha)$, where $l_3 + l_5 = l_8 \simeq 0$. (b) The same deformation plotted in the (s, α)-plane, where $s = r$.

Thus, the maxima of the deformation (9), where each wavevector is an integer combination of

$$\vec{k}_m = (l_m, m) = \left(\frac{2\pi}{\lambda}(q - md), m\right),$$

$$\vec{k}_n = (l_n, n) = \left(\frac{2\pi}{\lambda}(p - nd), n\right), \tag{13}$$

for given choices of d, λ, m, n and p, q such that $pm - qn = \pm g$, occur on a lattice spanned by the generators of phyllotactic lattices given by Eq. (6), namely

$$\vec{\omega}_m = \frac{1}{g}(\lambda m, 2\pi(md - q)),$$

$$\vec{\omega}_n = \frac{1}{g}(\lambda n, 2\pi(nd - p)). \tag{14}$$

The relationship between a pair of wavevectors (13) and the dual pair (14) of lattice generators can be expressed by defining the matrices

$$K = \begin{pmatrix} \vec{k}_n \\ \vec{k}_m \end{pmatrix} = \begin{pmatrix} \dfrac{2\pi}{\lambda}(p - nd) & n \\[2mm] \dfrac{2\pi}{\lambda}(q - md) & m \end{pmatrix},$$

$$\Omega = (\vec{\omega}_m, \vec{\omega}_n) = \frac{1}{g}\begin{pmatrix} \lambda m & \lambda n \\[2mm] 2\pi(md - q) & 2\pi(nd - p) \end{pmatrix}$$

such that

$$K\Omega = \pm 2\pi I.$$

There is an important difference between stating the phyllotactic lattice generators or the dual wavevectors that is central to this paper and is illustrated by the difference between Figs. 2(b) and 6(b). These figures show the same phyllotactic lattices, but only Fig. 6(b) also describes the shape of the phylla. Recall that a choice of g, d, λ determines a lattice, and the infinite number of bases of this lattice are given by Eq. (6) for any choice of m, n and p, q such that $pm - nq = \pm g$. Although a different choice of m, n, p, q determines the same phyllotactic lattice, a different choice of m, n, p, q in the statement of the wavevectors (13) yields a different orientation and shape (side lengths) of the (possibly irregular) hexagons or parallelograms. Also, given m, n, there is a preferred choice of integers p, q such that $pm - qn = \pm \gcd(m, n)$. The point 1 in Fig. 2(b) is a point in the set (10) with the minimal s-coordinate and thus the minimal value of $|Pm - Qn|$, which is the greatest common division $g = \gcd(m, n)$ of m and n. Of the infinitely many pairs (P, Q) such that $Pm - Qn = \pm g$, we define (p, q) to be that pair such that the point 1 is located at $(s, \alpha) = (\lambda, 2\pi d) = p\vec{\omega}_m - q\vec{\omega}_n$ (there may be two such points, as in Fig. 2(c,d), but the two points yield the choices $(p, q) = (0, 1)$ or $(1, 0)$). For this choice of p, q, $0 < \frac{p+q}{m+n} \leqslant \frac{1}{2}$; we will see how this ratio is related to the choice of divergence angle d.

Consider the spiral $l_m s + m\alpha = 2\pi q$. We have chosen (p, q) so that its intersection with $l_n s + n\alpha = 2\pi p$ is $(\lambda, 2\pi d)$ (see Fig. 6(b)). The intersection of $l_m s + m\alpha = 2\pi q$ with the next spiral $l_n s + n\alpha = 2\pi(p \pm 1)$ in the second family has s-coordinate $s_{next} = \lambda(1 \mp \frac{m}{g})$. The next phyllo on the $l_m s + m\alpha = 2\pi q$ spiral is therefore $\frac{m}{g}\lambda$ units away. For example, if $m = 3, n = 5$, as in Fig. 2, then $g = 1$ and the three clockwise spirals join the points $1, 4, 7, \ldots; 2, 5, 8, \ldots; 3, 6, 9, \ldots$ in the ordering scheme. Likewise, the spiral $l_n s + n\alpha = 2\pi p$ joins the phylla $\frac{n}{g}$ apart in the ordering scheme.

A description of the plant in terms of these deformations allows us to assign amplitudes to the periodic cosines, each having an argument $ls + m\alpha$, where m is a parastichy number. The amplitude sizes determine the relative importance of each mode. However, the amplitudes can be difficult to determine just by looking at the plant; we will show how they naturally emerge from the theory.

1.3. The formation of the patterns and the area of a new primordium

As a plant grows, most new material is added at regions of active cell growth and division called *meristems*. Meristems are found at the tip of a plant shoot (called the *apex*) and at the tips of roots. Here, we

will be primarily interested in the meristems found at the plant tip, called the *shoot apical meristem*. The SAM at the tip of a cactus is illustrated in Fig. 7, where one sees the inside (Fig. 7(c)) and outside (Fig. 7(b)) of a cactus. The inside of the plant, the *corpus*, is wet and porous. This squishy part is covered by a stiffer, more organized, outer layer called the *tunica*. Both the tunica and the corpus grow during plant growth, but growth occurs differently in different regions of the growth tip. Hernández et al. (1991) provide a description of the growth behavior of epidermal cells in the flower of *Anagallis*, and Dumais and Kwiatkowska (2001) have developed a non-destructive technique for following patterns of cell expansion and division in the tunica and used it to study the geometry and expansion of a shoot apex surface (Kwiatkowska and Dumais, 2003). These and similar studies lead to thinking of the SAM as having three zones as depicted in the schematic representation of Fig. 8. The SAM consists of Regions 1, 2, and 4 in the diagram. The tunica region of the SAM (Regions 1 and 2) is distinguished from the corpus (Region 4) is that tunica cells divide primarily in the plane of the plant surface, whereas corpus cells divide in any direction (Sachs, 1991). The tunica Regions 1 and 2 are distinguished from each other in that cells of Region 1 grow slowly and divide infrequently, whereas cells of Region 2 grow relatively quickly and divide more frequently.

It is in the Region 2 that phylla form as bumps (or localized regions of oriented cell division; see Section 2.3) called *primordia*; thus, we will call Region 2 the *generative region*. After their formation, these primordia develop further in shape so that they become, for example, leaves or florets; that is, they become *phylla*. Meanwhile, new material emanating from the inner part of the SAM becomes the material of the generative region and new primordia form. The relative positions of the phylla do not change as the plant grows; that is, the angular coordinate of a phylla and the difference between the radial coordinates of any two phylla remain constant. Thus, the phyllotactic pattern is set by the positions at which primordia form in the generative

region. We will henceforth refer to those phylla located in the generative region as primordia.

It is essential to emphasize that the pictures that we show in this introduction are not microscopic images restricted to the generative region. Although the phyllotactic pattern is set in the generative region, the polygonal planform that one observes on these plants is a product of both the original shape formed in the generative region and subsequent morphological changes as the phylla mature. We discuss this important point in more detail in Section 5.

It will be convenient to determine the area of a primordium in terms of the phyllotactic lattice parameters. For this, we call the mean radius of the annular generative region R (see Fig. 8). Then, approximating the radial distance of any primordium from the center by R, the area of the parallelogram determined by the two vectors $\omega_m = \frac{1}{g}(\lambda m, 2\pi R(md - q))$, $\omega_n = \frac{1}{g}(\lambda n, 2\pi R(nd - p))$ is the area of a primordium. This area is the determinant of the matrix

$$\Omega' = (\omega_m'^t \omega_n'^t)$$

$$= \frac{1}{g}\begin{pmatrix} \lambda m & \lambda n \\ 2\pi R(md - q) & 2\pi R(nd - p) \end{pmatrix}, \tag{15}$$
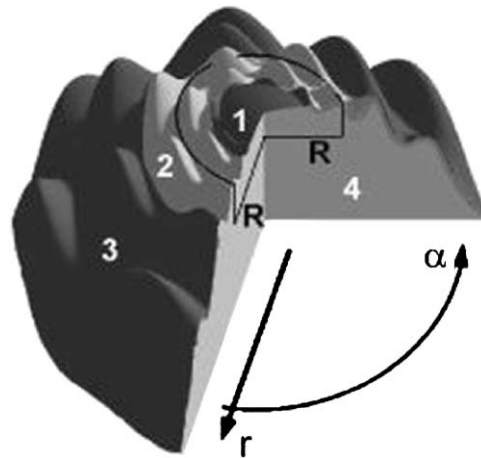

Fig. 8. Schematic representation of the SAM.
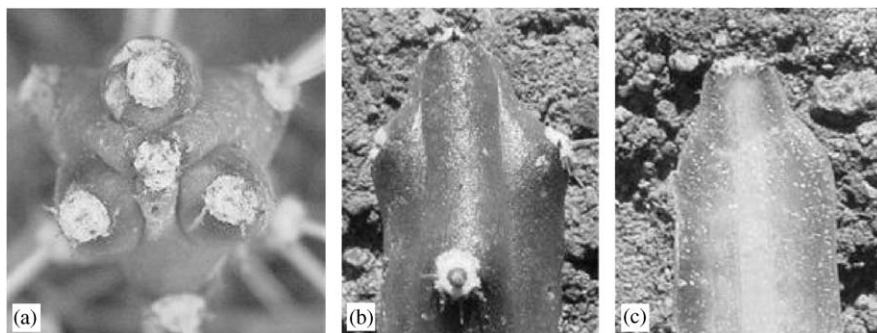
Fig. 7. What a cactus with an alternating 3-whorl ($g = 3$, $d = \frac{1}{6}$) pattern looks like (a) from the top, (b) from the side, and (c) inside.

that is, the area of a primordium is given by $A = \det \Omega' = 2\pi \frac{\lambda}{g} R$. Notice that this area is independent of the divergence angle.

1.4. The parameters found in nature

We have described phyllotactic patterns as lattice patterns that form at the boundary of the SAM and have introduced natural lattice parameters, the whorl number g, the divergence angle $D = 2\pi d$, the plastrochrone ratio λ. Also, we have defined the parastichy pair (m, n) and the area $A = 2\pi \frac{\lambda}{g} R$ of a primordium. It turns out that some values and combinations of these parameters are more prevalent in nature than others. There are two key observations in this regard.

The first observation relates the divergence angle to the parastichy pair. Given a triad of lattice generators (and the dual triad of wavevectors)

$$\vec{\omega}_m = \frac{1}{g}(m\lambda, 2\pi(md - q)),$$

$$\vec{\omega}_n = \frac{1}{g}(n\lambda, 2\pi(nd - p)),$$

$$\vec{\omega}_{m+n} = \frac{1}{g}((m+n)\lambda, 2\pi((m+n)d - (p+q))),$$

$$\vec{k}_m = \left(\frac{2\pi}{\lambda}(q - md), m\right),$$

$$\vec{k}_n = \left(\frac{2\pi}{\lambda}(p - nd), n\right), \qquad (16)$$

$$\vec{k}_{m+n} = (2\pi((p+q) - (m+n)d), m+n),$$

where $pm - nq = \pm g = \gcd(m, n)$, the divergence angle is observed to be equal to or approximately equal to the value $D = 2\pi d = 2\pi\frac{p+q}{m+n}$ that makes the third radial wavenumber zero; that is, the triads read

$$\vec{\omega}_m \simeq \frac{1}{g}\left(m\lambda, 2\pi\frac{\mp g}{m+n}\right), \quad \vec{k}_m \simeq \left(\frac{2\pi}{\lambda}\frac{\pm g}{n+m}, m\right),$$

$$\vec{\omega}_n \simeq \frac{1}{g}\left(n\lambda, 2\pi\frac{\pm g}{m+n}\right), \quad \vec{k}_n \simeq \left(\frac{2\pi}{\lambda}\frac{\mp g}{n+m}, n\right),$$

$$\vec{\omega}_{m+n} \simeq \frac{1}{g}((m+n)\lambda, 0), \qquad \vec{k}_{m+n} \simeq (0, m+n).$$

(17)

For the example of Fig. 2(a), choosing $m = 3, n = 5$, we find that $2(3) - 1(5) = 1$, so that $d \simeq \frac{1+2}{3+5} = \frac{3}{8}$. Indeed, $\frac{3}{8}$ is approximately the value 0.378 introduced earlier as the divergence angle. An example of a cactus that shows the same lattice parameters as the cactus of Fig. 2(a) except that d is exactly equal to the value $\frac{3}{8}$ that makes the third family of spirals purely radial is shown in Fig. 9(c); note the eight radial ridges.

The second observation concerns the area $A = 2\pi\frac{\lambda}{g}R$ of a newly formed primordium. As a plant grows from a seedling to a big adult plant, the parameter R will increase. The area A, however, is often observed to remain constant (Rutishauser, 1998; Kwiatkowska, 1995; Kwiatkowska and Florek-Marwitz, 1999). This can be achieved either by increasing the number g of primordia in a whorl or by decreasing the plastochrone ratio λ. Both of these approaches are found in nature, and both lead to changes in the parastichy numbers (m, n) as described below. Thus, the pattern that is observed at any time on a plant is the result of the initial pattern formed when the plant begins to develop phylla and the transitions from this pattern that occur as the plant grows in size. Note that, as g is an integer, it cannot be continuously changed to counteract changes in R; in contrast, the plastochrone ratio λ is a continuous parameter. This difference will be apparent as we discuss transitions between patterns.

For some plants, most notably the sunflower, the parameter R decreases during a portion of the pattern formation, but the area A is still constant. Thus, on a sunflower head, one often observes, for example, a (8,13,21)-spiral pattern on the outer edge of the disk and a (5,8,13)-spiral pattern in the more recently formed center of the disk. Transitions involve moving up the Fibonacci sequence as a function of Γ but down the Fibonacci sequence as time evolves.

1.5. Transitions between patterns

It is well known that under the change of stress parameters, patterns can undergo bifurcations or phase transitions. In the most typical phase transition, as the stress parameter is increased above a certain critical value, the pattern makes a discontinuous jump from one state to another. Decreasing the same stress parameter leads to a reverse jump from the new to the original state, but this occurs at a different value of the stress parameter. The difference is called hysteresis. This type of bifurcation is referred to as a *first-order* phase transition; examples include the change from ice to water at 0°C, or the onset of a hexagonal pattern from the uniform state in Rayleigh–Bénard convection. In contrast, *second-order* phase transitions, such as the onset of a roll pattern in Rayleigh–Bénard convection, are continuous. Both first (I) and second (II)-order phase transitions are observed in plant patterns (Meicenheimer and Zagorska-Marek, 1989; Meicenheimer, 1998).

Transitions between patterns on various cacti are exhibited in Fig. 9. In Fig. 9(a–d) one observes defects as new ridges are added; these are examples of sudden transitions and are thus Type I transitions. In Fig. 9(e and f) a cactus with a parastichy pair (3,5) grows continuously into a cactus with parastichy pair
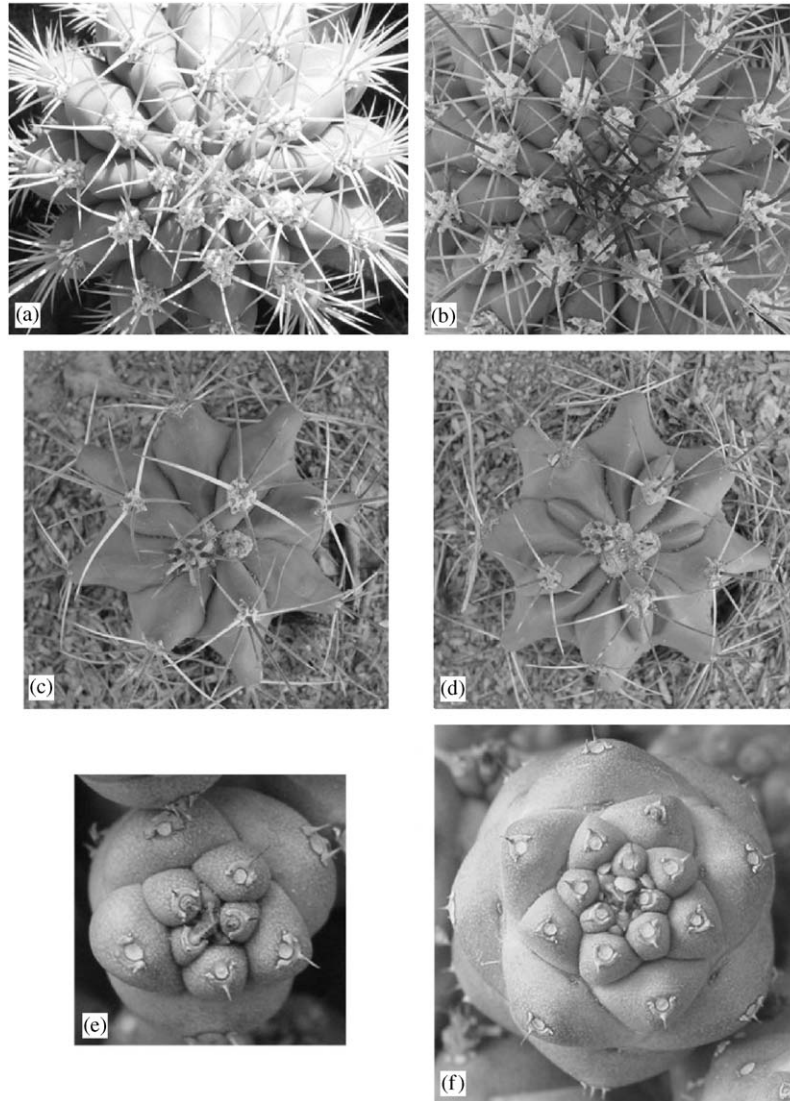
Fig. 9. Transitions between patterns. (a,b) An Argentinian saguaro with (a) 12 ribs adds (b) a new rib, producing a dislocation defect. This is a Type (I,1) transition. (c,d) A barrell cactus with (c) eight ribs adds (d) five new ribs, as marked by the five dislocations. This is a (I,2) transition. (e,f) A cactus with (e) a (2,3,5)-spiral pattern evolves into one with a (3,5,8)-spiral pattern as the cactus grows larger. No defect is observed; this is a (II,2) transition.

(5,8); no defect is observed, so this is a Type II transition.

These transitions can be described using the framework of the triad

$$\vec{\omega}_m = \frac{1}{g}(m\lambda, 2\pi(md - q)),$$

$$\vec{\omega}_n = \frac{1}{g}(n\lambda, 2\pi(nd - p)),$$

$$\vec{\omega}_{m+n} = \omega_m + \omega_n$$
$$= \frac{1}{g}((m+n)\lambda, 2\pi((m+n)d - (p+q))) \tag{18}$$

of lattice generators and its wavevector dual

$$\vec{k}_m = \left(\frac{2\pi}{\lambda}(q - md), m\right),$$

$$\vec{k}_n = \left(\frac{2\pi}{\lambda}(p - nd), n\right),$$

$$\vec{k}_{n+m} = \vec{k}_m + \vec{k}_n = \left(\frac{2\pi}{\lambda}(p + q + (m+n)d), m+n\right). \tag{19}$$

1.5.1. Type (I,1) transitions

The cactus of Fig. 9(a) exhibits a pattern with $m = n = 6$ and $d = \frac{1+0}{6+6} = \frac{1}{12}$ so that the descriptive triads are

$$\vec{\omega}_6 = \frac{1}{6}(6\lambda, \pi), \qquad \vec{k}_6 = \left(-\frac{\pi}{\lambda}, 6\right),$$

$$\vec{\omega}'_6 = \frac{1}{6}(6\lambda, -\pi), \qquad \vec{k}'_6 = \left(\frac{\pi}{\lambda}, 6\right), \tag{20}$$

$$\vec{\omega}_{12} = \frac{1}{6}(12\lambda, 0), \qquad \vec{k}_{12} = (0, 12),$$

the third members of the triad telling us that the cactus exhibits 12 ridges. In Fig. 9(b), the cactus has added a new ridge, so that it now has a 13th ridge, added where one sees a dislocation in the lower left of the picture. The new pattern is described by the parameters $m = 6, n = 7$, $d = \frac{2}{13}$, so that the triads describing the new pattern read

$$\vec{\omega}_6 = \left(6\lambda', \frac{2\pi}{13}\right), \qquad \vec{k}_6 = \left(\frac{2\pi}{13\lambda'}, 6\right),$$

$$\vec{\omega}_7 = \left(7\lambda', -\frac{2\pi}{13}\right), \qquad \vec{k}_7 = \left(-\frac{2\pi}{13\lambda'}, 7\right), \tag{21}$$

$$\vec{\omega}_{13} = (13\lambda', 0), \qquad \vec{k}_{13} = (0, 13).$$

This is a first-order transition (as there is an abrupt change in the number of ribs), and one angular wavenumber was retained. We thus call it a (I,1) transition, the first numeral denoting the type of phase transition, and the second number denoting the number of angular wavenumbers in a triad that are retained. For a (I,1) transition, it is, in fact, observed that it is not just an angular wavenumber that is retained, but an entire wavevector. This is illustrated in Fig. 10, which shows the side view of a cactus that has undergone a (I,1) transition. As the cactus increases its number of ribs by one, two families of spirals, including the family of purely radial spirals, form dislocations,

and where the dislocations meet a defect is seen. This defect is called a penta–hepta defect as it consists of a heptagon and a pentagon in the otherwise hexagonal planform. However, the third family of spirals does not change, indicating that the transition has not affected the associated wavevector. In the example of the transition from Eq. (20) to Eq. (21), the vector $\vec{k}'_6$ of Eq. (20) equals the vector $\vec{k}_6$ of (21); that is, $\frac{\pi}{\lambda} = \frac{2\pi}{13\lambda'}$, or $\lambda' = \frac{2\lambda}{13}$. This is consistent with the second observation of Section 1.4; if the transition from Eq. (20) to Eq. (21) occurs as the mean radius changes slightly from $R = 12$ to $R' = 13$, then $\lambda' = \frac{2\lambda}{13}$ implies that the area $A = 2\pi\frac{\lambda}{g}R$ associated with the pattern (20) equals the area $A' = 2\pi\lambda'R'$ associates with the pattern (21). We will discuss this in more detail in Section 4.

The Argentinian saguaro of Fig. 11 has made a sequence of (I,1) transitions, changing from having $N = 10, 11, 12, 13$ ridges. This sequence of transitions is commonly observed on cacti that show strong ridge configurations.

Plants that follow a sequence of Type (I,1) transitions exhibit an alternating whorl configuration when they have an even number of ribs. The *alternating g-whorl* consists of groups of g leaves that alternate in angle. In general, an alternating g-whorl is described by the lattice generators

$$\vec{\omega}_g = \frac{1}{g}(g\lambda, 2\pi(gd - 1)),$$

$$\vec{\omega}'_g = \frac{1}{g}(g\lambda, 2\pi(gd - 0)),$$

$$\vec{\omega}_{2g} = \omega_g + \omega'_g = \frac{1}{g}(2g\lambda, 2\pi(2gd - 1)),$$
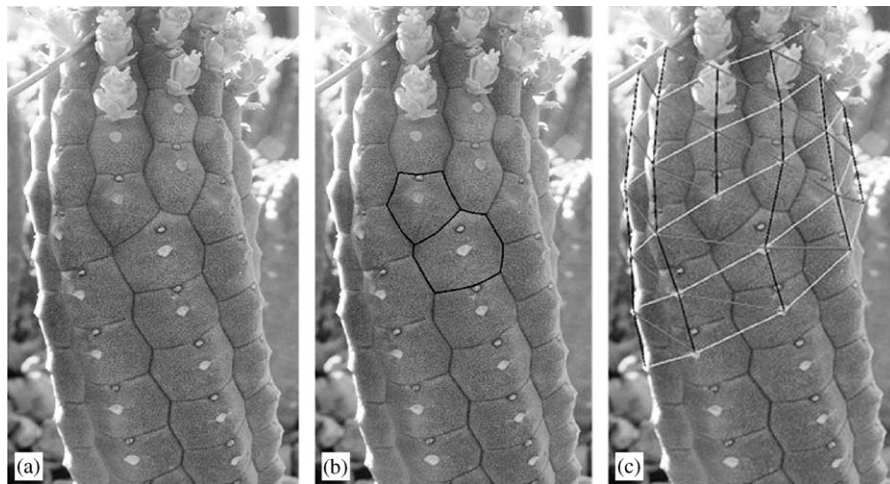
Fig. 10. A penta–hepta defect on a cactus is formed by two dislocations; one wavevector is retained in this (I,1) transition. (a) The cactus has a hexagonal planform, except that (b) there is a penta–hepta defect. (c) Connecting opposite sides of hexagons, one obtains the three sets of ridges that form the hexagonal pattern. Two sets (marked in black and gray) have dislocation defects; the third set (marked in white) has no defect.
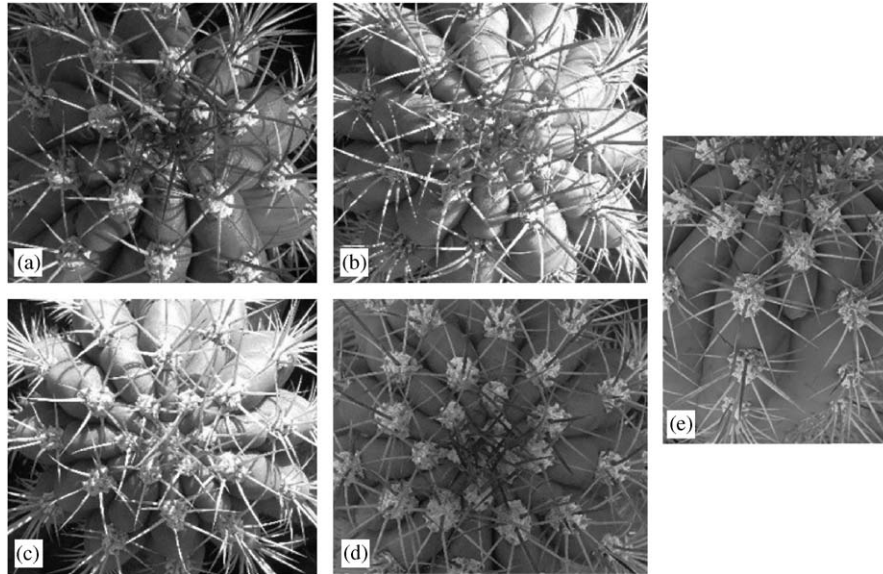
Fig. 11. This Argentinian saguaro has (a) 10 ridges, (b) 11 ridges, (c) 12 ridges, and (d) is about to form a 13 ridge, thus obtaining a defect (e).

$$\vec{k}_g = \left(\frac{2\pi}{\lambda}(1 - gd), g\right),$$

$$\vec{k}'_g = \left(\frac{2\pi}{\lambda}(-gd), g\right),$$

$$\vec{k}_{2g} = \left(\frac{2\pi}{\lambda}(1 - 2gd), 2g\right)$$

with $d = \frac{1}{2g}$; that is,

$$\vec{\omega}_g = \frac{1}{g}(g\lambda, -\pi), \qquad\qquad \vec{k}_g = \left(\frac{\pi}{\lambda}, g\right),$$

$$\vec{\omega}'_g = \frac{1}{g}(g\lambda, \pi), \qquad\qquad \vec{k}'_g = \left(-\frac{\pi}{\lambda}, g\right),$$

$$\vec{\omega}_{2g} = \omega_g + \omega'_g = \frac{1}{g}(2g\lambda, 0), \quad \vec{k}_{2g} = (0, 2g).$$

Examples of alternating 1-, 2- and 3-whorls are shown in Fig. 12, and the example of Fig. 13(e) is an alternating 6-whorl. A much more rare pattern is the *superposed g-whorl*; this pattern consists of groups of g leaves that do not alternate in angle. An example of a superposed 2-whorl is shown in Fig. 12(b).

1.5.2. Type (I,2) transitions

The cactus of Fig. 9(c) exhibits a pattern with $m = 3, n = 5$ and $d = \frac{1+2}{3+5} = \frac{3}{8}$ so that the descriptive triads are

$$\vec{\omega}_3 \simeq \left(3\lambda, \frac{\pi}{4}\right), \qquad \vec{k}_3 \simeq \left(-\frac{\pi}{\lambda}, 3\right),$$

$$\vec{\omega}_5 \simeq \left(5\lambda, -\frac{\pi}{4}\right), \quad \vec{k}_5 \simeq \left(\frac{\pi}{\lambda}, 5\right), \qquad\qquad (22)$$

$$\vec{\omega}_8 \simeq (8\lambda, 0), \qquad \vec{k}_8 \simeq (0, 8),$$

the third members of the triad telling us that the cactus exhibits 8 ridges. In Fig. 9(d), the cactus has added five new ridges, so that it now has a thirteen ridges, a new ridge added at each of the five dislocations. The new pattern is described by the parameters $m = 5, n = 8$, $d = \frac{2+3}{5+8} = \frac{5}{13}$, so that the triads describing the new pattern read

$$\vec{\omega}_5 \simeq \left(5\lambda, \frac{2\pi}{5}\right), \qquad \vec{k}_5 \simeq \left(-\frac{\pi}{4\lambda}, 5\right),$$

$$\vec{\omega}_8 \simeq \left(8\lambda, -\frac{2\pi}{8}\right), \quad \vec{k}_8 \simeq \left(\frac{\pi}{4\lambda}, 8\right), \qquad (23)$$

$$\vec{\omega}_{13} \simeq (13\lambda, 0), \qquad \vec{k}_{13} \simeq (0, 13).$$

In this transition, two angular wavenumbers (5 and 13) are retained and the corresponding radial wavenumbers are slightly changed. Thus, we will refer to this type of transition as a (I,2) transition; it is a discontinuous (Type I) transition in which 2 angular wavenumbers are preserved.

1.5.3. Type (II,2) transitions

In contrast to the rational divergence angles values of d in the first two cacti of Fig. 9, the cactus of Fig. 9(e and f) exhibits irrational values of d. In Fig. 9(e), the cactus exhibits the values $m = 2, n = 3$, and d, although irrational, is approximately equal to $\frac{1+2}{2+3} = \frac{2}{5}$. At this point, we describe the normal deformation of $w(s, \alpha)$ of a plant as the sum

$$w(s, \alpha) = \sum_{j=2,3,5,8} a_j \cos(\vec{k}_j \cdot \vec{x}), \quad \vec{x} = (s, \alpha), \qquad (24)$$
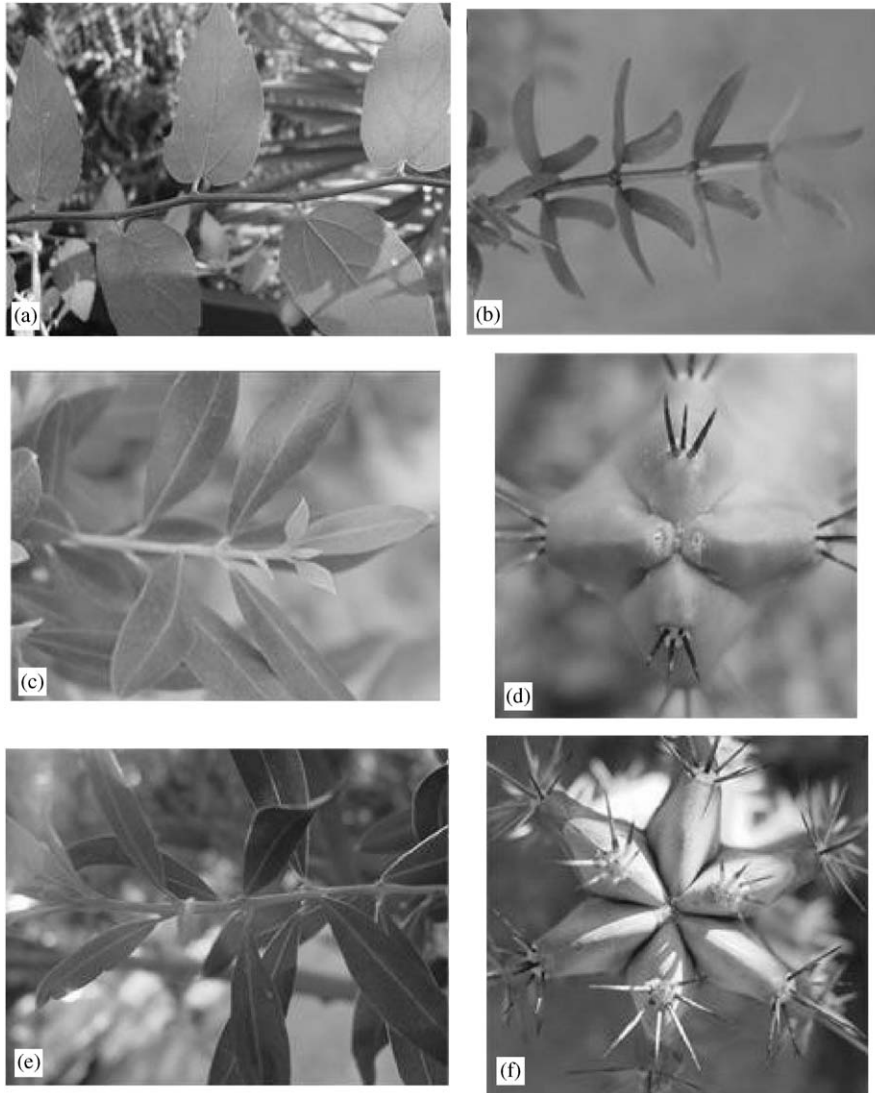
Fig. 12. Whorls. (a) An alternating 1-whorl, (b) a superposed 2-whorl, (c,d) alternating 2-whorls, (e,f) alternating 3-whorls.

where

$$\vec{k}_2 = \left(\frac{2\pi}{\lambda}(1 - 2d), 2\right),$$

$$\vec{k}_3 = \left(\frac{2\pi}{\lambda}(1 - 3d), 3\right),$$

$$\vec{k}_5 = \vec{k}_2 + \vec{k}_3,$$

$$\vec{k}_8 = \vec{k}_3 + \vec{k}_5,$$

where $d \simeq \frac{2}{5}$ is irrational. As the plant increases in size, so that the radius R increases, the amplitude a_2 of the mode with radial wavenumber 2 decreases continuously as the amplitude a_8 of a mode with wavevector $\vec{k}_8$ increases in amplitude; the divergence angle d changes slightly, moving closer to the value $d \simeq \frac{3}{8}$ that makes the wavevector $\vec{k}_8 \simeq (0, 8)$.

This type of transition involves the continuous change in the divergence angle $2\pi d$ and plastochrone ratio λ so that as the pattern dominated by the spiral families (2,3,5) evolves into that dominated by the spiral families (3,5,8). The two angular wavenumbers 3 and 5 are invariant in the transition, and the associated radial wavenumbers only change slightly. We will show in Section 4 how λ changes so as to keep the primordium area $A = 2\pi\frac{\lambda}{g}R$ constant, and also how the amplitudes a_2, a_3, a_5, a_8 also change smoothly, a_2 decreasing and a_8 increasing with increasing R. As this is a continuous (Type II) transition in which two angular wavenumbers are preserved, we will call it a (II,2) transition.

1.5.4. (I,1) vs. (II,2) transitions and (I,0) transitions

What determines the type of transition that a plant will undergo? One clue lies in the following observation
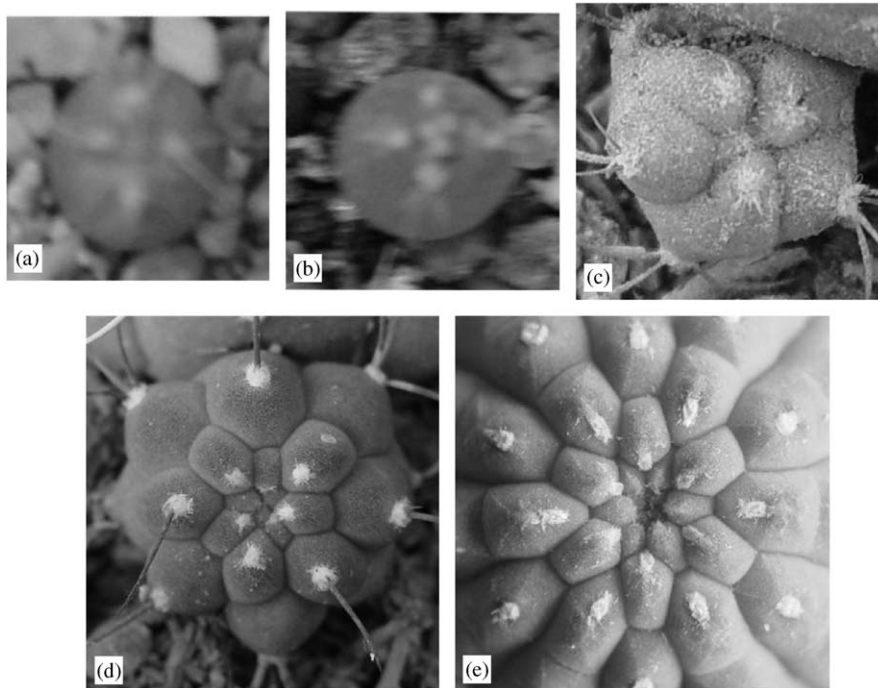
Fig. 13. As it grows up, this cactus of the genus *Matucana* shows (a) an alternating 2-whorl pattern, (b) a transition to (2,3,5)-spiral pattern, (c) a (2,3,5)-spiral pattern, (d) a (3,5,8)-spiral pattern, and (e) an alternating 6-whorl pattern.

of cacti: cacti that show strong rib configurations (such as saguaro cacti) tend to undergo (I,1) transitions, while cacti that show parallelogram or staircase parallelogram configurations tend to undergo (II,2) transitions. Cacti with hexagonal configurations may undergo either type of transition. (These are the authors' observations; we suggest in Section 5 a closer experimental study of the relationship between shape and transition type.) In Section 4, we will show how the surface curvature of the plant tunica in the generative region may determine the choice between the various planforms and transition types; larger curvature will be shown to favor triad configurations with more than one large amplitude.

Plants may exhibit (I,1) or (II,2) transitions at different points in their lives. An example is given by the cactus of Fig. 13. The alternating 2-whorl pattern is observed in Fig. 13(a). The cactus begins a transition to a different pattern in Fig. 13(b), the pattern is eventually seen in Fig. 13(c) to be the Fibonacci pattern with generators ω_3, ω_4 of the SPLGS evaluated at $d \simeq \frac{2}{5}$. This is a (I,1) transition. The pattern later gradually shifts to one with generators ω_4, ω_5 of the SPLGS evaluated at $d = \frac{3}{8}$ and as pictured in Fig. 13(d). This is a (II,2) transition. Eventually, the Fibonacci sequence is lost again as the cactus begins to make Type (I,1) transitions; in Fig. 13(e) the cactus has 12 (not a Fibonacci number) ribs; the triads of angular wavenumbers moved up the sequence $(3, 5, 8)$, $(4, 5, 9)$, $(5, 5, 10)$, $(5, 6, 11)$, $(6, 6, 12)$. This behavior of eventually shifting back to Type (I,1) transitions is particularly prominant in cacti in which

radial ridges become the prominant feature. There is no published data giving answers to questions that we have here—for example, what percentage of plants that exhibit the Fibonacci sequence start out with the alternating 2-whorl pattern? Nevertheless, the alternating 2-whorl is a common originating pattern, and the transition from the alternating 2-whorl to (2,3,5) spiral phyllotaxis stated by Meicenheimer (1998) to be the most common Type I transition.

Kwiatkowska (1995) studies the changes of phyllotaxis in *Angagallis Arvensis* L. She shows that the alternating 2-whorl (decussate) phyllotaxis is always the initial pattern and is typically followed by (I,1) transitions. However, in rare cases, instead of this $(2, 2, 4) \rightarrow (2, 3, 5) \rightarrow (3, 3, 6) \rightarrow \cdots$ sequence, the plant undergoes a transition $(2, 2, 4) \rightarrow (3, 3, 6)$. In the terminology presented here, this would be a $(I, 0)$ transition.

1.6. Outline

The outline of this paper is as follows: in Section 2, we discuss the historical background of attempts to understand plant forms, describe the more recent ideas of DC and Green and his colleagues, and formulate our model. Section 3, which may be skipped on a first reading, contains the details of the elastic energy of the compressed zone, the FvKD equations, the linear stability analysis of the uniformly compressed state, and the weakly nonlinear analysis describing the competition between planforms. Section 4 discusses

the properties of important coefficients and shows how and why certain energy-minimizing configurations are preferred. This section can be read without having first read Section 3. Section 5 addresses three questions; (1) What postdictions, namely explanations of behaviors already observed, and what predictions are consistent with and arise from our theory? (2) What observations should we encourage experimentalists to make? (3) How could, and to what degree should, our picture, and the model used to capture its essential ingredients, be improved? Finally, in the appendix, we give more details on the wavevector description of (II,2) transitions.

2. Historical background and models

In this section, we present a short background of phyllotactic investigations which have dealt with observations and mathematical descriptions of plant patterns, kinematic descriptions of the formation of these patterns over time, and studies into possible mechanisms for the formation of phylla. Finally, we present our model. More information on the history of phyllotactic research and observations can be found in Barabé et al. (1997).

2.1. Observational phyllotaxis and mathematical description

The occurrence of Fibonacci numbers—those in the sequence $1, 1, 2, 3, 5, 8, \ldots$—on plants has long been noted. The first recorded observation of the prevalence of Fibonacci numbers on plants is due to Johannes Kepler, who explained his observation of the number 5 as so (Livio, 2002):

"I see the number five in almost all blossoms which lead the way for a fruit, that is, for creation, and which exist, not for their own sake, but for that of the fruit to follow. Almost all tree blossoms can be included here; I must perhaps exclude lemons and orange; although I have not seen their blossoms and am judging from the fruit or berry only which are not divided into five, but rather into seven, eleven, or nine cores. But in geometry, the number five, that is the pentagon, is constructed by means of the divine proportion which I wish [to assume to be] the prototype for the creation."

The "divine proportion" is the Golden Ratio; that is, the positive root of the quadratic equation $x^2 - x - 1 = 0$ which describes the condition on the ratio x of the sides of a rectangle so that, upon removing a square from the rectangle, the sides of the remaining smaller rectangle have the same ratio of lengths.

Kepler's observations of numbers on plants were extended into a account of various types of phyllotactic patterns by Charles Bonnet in his 1754 treatise *Recherches sur l'Usage des Feuilles dans les Plantes* (Bonnet, 1754). Further mathematical descriptions of phyllotaxis were made in the 1830s by Schimper (1830, 1836), who defined the divergence angle and Braun (1831) who noted Fibonacci numbers on pine cones. Also in the 1830s, the Bravais brothers (Bravias and Bravais, 1837) showed that if a spiral of phylla is a member of a family of n spirals, then the numbers associated to those phylla (as in Fig. 2) increase by n as the spiral proceeds from the center of the plant out. The idea of the plastochrone ratio took longer to appear; it was introduced by Richards in 1948 (Richards, 1948, 1951). This set of works allows us to describe the phyllotactic pattern that we may find on a plant. The pattern, however, is formed over time, with phylla closer to the tip of the plant having been formed later than those far from the tip.

2.2. Dynamical description and electromechanical paradigm

As far back as 1868, Hofmeister (1868) proposed a set of rules that provide a kinematic description of the formation of phyllotactic patterns. As quoted from Douady and Couder (1996a), these rules read

1. The stem apex is axisymmetric.
2. The primordia are formed at the periphery of the apex (Region 2 in Fig. 8), and, due to the shoot's growth, they move away from the center with a radial velocity $V(r)$ which may depend on their radial location.
3. New primordia are formed at regular times intervals (the plastochrone time T).
4. The incipient primordium forms in the largest available space left by the previous ones.
5. Outside of a region of radius R there is no further reorganization leading to changes in the angular position of the primordium.

Motivated by the Hofmeister rules, Douady and Couder (1992,1996a, b, c) built an ingenious experimental device in which ferromagnetic droplets choose a divergence angle and therefore a phyllotaxis-like lattice. Earlier theoretical work of Levitov (1991a, b) showed that phyllotactic patterns and Fibonacci sequences can arise in layered superconductors that minimize a global interaction energy. Energy minimization also played a central role in the experiment of DC. The basic device is a plate with a small central dome in the middle; this is to represent to the plant with the apex at the tip. The plate is placed in a vertical magnetic field that is stronger at the edges of the plate than in the middle, and ferromagnetic drops (representing primordia) are periodically dropped onto the center of the central dome

(representing the apex). The drops fall to the perimeter of the central dome and then move radially outward, following the gradient of increasing magnetic strength. The magnetic field is chosen so that the velocity $V(r)$ in an exponentially increasing function of the radius. After choosing a radial direction in which to fall from the top of the central dome, the drops do not change their angular coordinate. How the drops initially choose their angular coordinate is of interest, and here the central point is that the drops form repelling magnetic dipoles. A drop that falls on the central dome moves to the position on the boundary of the dome as determined by the repulsions of the drops that recently formed and are moving away from the center, and the experimental result is that a there is constant divergence angle between the angular coordinates of successively dropped drops. Denoting the radius of the central dome by R, the initial speed of the drops after falling to the boundary of the dome by V_0, and the time period in which drops are dropped onto the central dome by T, the plastochrone ratio of the resulting pattern is $G \doteq \frac{V_0 T}{R}$. G is a parameter chosen by the experimenter. As DC decrease G, the resulting divergence angle approaches the golden angle, and the pattern appears as one with a Fibonacci parastichy pair. The suggestion of this experiment is that simple dynamical rules as suggested by Hofmeister are at the center of the phyllotactic process.

As it only allows one drop to form at a time, the electromechanical paradigm does not allow for the formation of whorl patterns. In subsequent numerical simulations, Douady and Couder (1996b, c), following a modification of Hofmeister's rules as suggested by Snow and Snow (1952), replaced the T-periodic formation of primordia with a new parameter—the space needed for a new primordium to form. In these experiments, primordia are represented as disks that form at a generative circle of radius R surrounding the pole of a parabolic shape representing the apex. The disks then move radially outward. DC define an energy function on the generative circle which is designed so that the energy decreases below a threshold value whenever a new primordium of fixed radius d_0 can form without overlapping with previously formed primordia. Primordia that have formed and moved away from the generative circle thus have an inhibitory action on the generative circle that decreases as the primordia move radially outward. The role of $G = \frac{V_0 T}{R}$ was taken by a parameter $\Gamma = \frac{d_0}{R}$ (equivalent to the inverse of the parameter Γ we introduce below); Douady and Couder refer to Γ as van Iterson's parameter, as van Iterson (1907) used a similar parameter in a description of plant patterns. In these numerical paradigms, phyllotactic lattice patterns form, with increasing parastichy pair parameters as Γ decreases. Furthermore, the parastichy pairs may change in either (I,1) or (II,2) transitions. Douady and Couder (1996c) show that (I,1) transitions

are preferred unless the parameter Γ is decreased quickly enough so that the system does not have enough time to adjust and shift to the next mode in a Type I transition, in which case (II,2) transitions occur.

As a way of understanding the results, Douady and Couder (1996b) offer an explanation in terms of optimization of "packing compacity." The idea is as follows: All of the primordia (disks) that form at the generative circle and move radially outward in a given time interval ΔT will be contained in an annulus of inner radius R and width depending on ΔT. The ratio β of the area of this annulus to the sum of the areas of the disks gives a measure of how compactly the primordia are arranged on the apex, and DC calculate that the most stable modes in their model are those that minimize β—i.e., those that optimize the packing.

The DC paradigms rely on the positions of previously formed primordia of a given size and shape to form an energy functional on the generative circle, and Douady and Couder (1996c) suggest that the crucial components of the physiological process that it (i) creates primordia of a well-defined, finite size, and (ii) gives the primordia a repulsive or inhibitory interaction. As described above, however, phyllotaxis is intimately related to polygonal planforms, and, as it assumes that primordia will form, the DC model does not encompass the spectrum of shapes that range from ridges (with no or poorly defined primordia) to hexagons and parallelograms. In the mechanical model that we present below, we will show the determination of a finite area for primordia is essential and how the interaction of *elementary periodic deformations* instead of *primordia* allows us to consider polygonal planforms and phyllotaxis in one picture.

2.3. Mechanisms for primordia formation

So far, we have described plant patterns and the kinematics of how they form. Why do patterns form at all? What is the mechanism for the formation of primordial bumps at SAMs? The answer is not clear, but there is experimental evidence that both chemistry and biophysics play some role—both chemical signals, such as growth hormones, and physical signals, such as growth forces on the apical material, have been linked to primordium formation.

The role of biophysics was first studied in the late 1800s by the Swiss botanist Simon Schwendener (the predecessor to Hofmeister as the curator of the botanical garden at Basel) (Schwendener, 1874, 1878, 1883, 1909). Schwendener studied the material properties of plants with the aim of building a foundation upon which to understand how these properties may affect plant form. His work, however, did not directly demonstrate a connection between pattern formation and the material properties. In the 1980s and 1990s,

Green (1992a, b) and Green et al. (1998), Hernández et al. (1991) and Steele (2000) investigated the possibility that the growth forces that lead to buckling of the plant tunica are primarily responsible for determining phyllotaxis. Various papers suggest observations indicating that the mechanics of the plant plays a role in the pattern-forming process. Some of these are as follows:

1. Hernández and Green (1993) grew a sunflower head between two fixed parallel bars. This resulted in an amplification of undulations parallel to the bars, and phyllotaxis followed this pattern. This external mechanical influence also changed the identity of the sunflower bracts.
2. Green (1999) induced a new row of leaves to form on an expanding meristem by using a glass frame to apply a mechanical constraint.
3. Steele (2000) noted that the turgor pressure inside plant cells is between 7 and 10 atmospheres, and that this large pressure can hardly be ignored in the phyllotactic process. Also, in this paper, Steele notes a linear relationship between the size of primordia and the thickness of the tunica.
4. Dumais and Steele (2000) showed sunflowers cut along a diameter. The two sides of the cut stick together only in the region of the surface where the pattern formation is occurring, indicating that the compressive force keeping the cut closed is related to the pattern formation.
5. Fleming et al. (1997) were able to induce primordia on tomato plants by locally applying the protein expansin; some of these primordia then developed into leaf-like structures. The known effect of the extracellular expansin proteins is to increase cell wall extensibility, thus changing the mechanical properties of the plant material.

An overview of the role of mechanics in leaf initiation and development is found in Green's review (1999). Green points out that pattern formation is occurring at different space scales on a plant, and that these processes interact with each other. On the large-scale, there is the formation of primordia in special phyllotactic lattices and the determination of primordia shape. On the small-scale—that is, at the level of the individual cells—there are patterns of cell division and reinforcement of cell walls by cellulose. Green's overall picture of biophysical effects in plant pattern formation is this: compressive physical stresses that arise during plant growth leads to large-scale buckling of the tunica. This provides curvature variation in the tunica, and both curvature and strains influence the orientation of cellulose microfibrils in the cell walls. This alters the mechanical properties of the cell walls, reinforcing the pattern and influencing the direction of further growth and cell divisions, and thus influencing the pattern of growth stresses that develops. The resulting stress fields then in turn reinfluence the cellulose orientation. There is thus a feedback mechanism that generates form.

Dumais and Steele (2000) review two possible sources of compressive stress in the tunica that could lead to buckling. One possibility is that of *differential growth*—either the tunica is growing faster than the inner corpus, as suggested by Schüpp (1914) and Priestly (1928), or, as proposed by Green (1992b), there is a variation of growth intensity within the tunica layer. The excess growth of the tunica, in this theory, leads to compressive stresses and ultimately results in buckling. The second possibility, as suggested by Selker et al. (1992), Steucek et al. (1992), and Steele (2000), views the tunica as a *pressurized shell*. In this case, it is the corpus that is growing faster than the tunica shell upon which it exerts pressure. If the tunica is a spherical shell as depicted in Fig. 14, the tunica would then be under *tensile* stress rather than the *compressive* stress that is necessary to induce buckling. However, the geometry of the apex in the generative region is observed to be an inverted sphere or hyperbolic, as discussed in Section 2.4. For these geometries, there would be compressive stress in the pressurized shell.

Other work suggests that chemical signals play an important role in primordium formation. For example, the work of Reinhardt et al. (2003) demonstrates the relation of the plant hormone auxin to the formation of new primordia. The distribution of auxin, according to this work, is influenced by existing primordia, which act as auxin sinks, thus depleting the surrounding region of auxin. This work suggests a reason for Hofmeister's fourth rule—a new leaf forms in the largest space available as this space is least deprived of auxin.
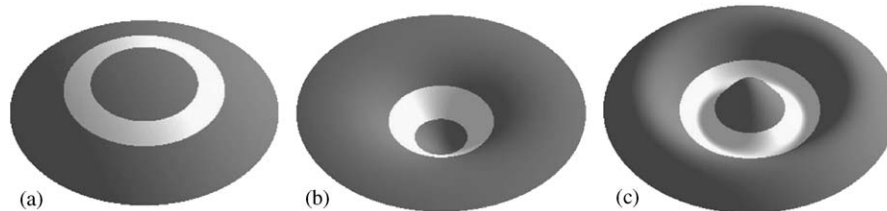

Fig. 14. (a) Spherical (R_α, $R_r > 0$), (b) inverted spherical (R_α, $R_r < 0$), and (c) hyperbolic ($R_\alpha > 0$, $R_r < 0$) geometries of the generative region, denoted by light shading.

These sets of observations involving chemical and biophysical mechanisms do not contradict each other. The study of Fleming et al. (1997), for example, suggests that chemical signals are involved in producing the biophysical properties that can lead to shell buckling. The question, however, is this: what mechanism or mechanisms set the pattern? Does, for example, a pattern of varying expansin concentration develop and thus set the phyllotactic pattern, or is the pattern set first by the buckling tunica? Or, are these two mechanisms linked together? This question has not been clearly answered by experiments or observations. It is possible that one mechanism may play a larger role for some plants and another mechanism for other plants.

Various mathematical models have attempted to show that various mechanisms are possible sources of the patterns. Until the early 1990s most models of phyllotaxis were based on chemical diffusion and reaction in the plant. Examples of these models are, for example, in Meinhardt et al. (1998), Harrison (1987) and Turing (1952). Green et al. (1998) have studied the von Kármán equations to demonstrate that shell buckling can produce primordial bumps, but were only able to produce spiral patterns by the imposition of special boundary conditions. These models have not addressed (i) primordia shape (i.e., ridges, hexagons, or parallelograms) or (ii) what conditions can give rise to (I,1) or (II,2) transitions. The biophysical model that we present below will test the ability of shell buckling to produce phyllotactic patterns, transitions between these patterns, and the various ridge or polygonal configurations. A similar shell-buckling model for the formation of fingerprint patterns was studied by Kücken and Newell (2004).

2.4. Biophysical model

In Section 1.3, we described how patterns in plants form at SAM where phylla first form as bumps called primordia in the annular generative region at the boundary of the SAM. We now formulate a model to test the hypothesis that it is the buckling of the tunica due to forces from plant growth that produce the primordia and thus set the phyllotactic pattern. This model only deals with the large-scale determination of the pattern; the interaction of biophysics with biochemistry is not included; see Section 5.

It is essential for our model to consider the geometry of the plant apex. Three possible geometries are shown in Fig. 14; the light-colored annular region in each picture represents the annular generative region, which we will henceforth denote by the letter M. In Fig. 14(a), M is part of a sphere, the corpus being attached to the inner part of the sphere. This, however, is not the typical shape of the region M; examining, for example, Fig. 1(c), one sees, at the plant tip, a geometry as depicted in Fig. 14(b). In this picture, M is again part of a sphere, but the corpus is attached to the outer part of the sphere. Another possibility is as depicted in Fig. 14(c); the region M surrounds a central dome. A comprehensive study of these various geometries is not available in the plant literature, although we observe the geometry of Fig. 14(b) on cacti, and microscopic images of sunflowers reveal either the geometry of Fig. 14(b) (Palmer, 1998) (Fig. 15(a)) or the geometry of Fig. 14(c) (Fig. 15(c)) (Steele, 2000). Our model will include all possibilites.

We model the generative region as a thin elastic shell of mean radius R (the tunica) attached to an elastic foundation (the corpus) and under compressive stress (due to plant growth and/or the hardening of the tunica material). The various geometries are described via *signed radii of curvature* that give the direction and magnitude of the shell's curvature. For this, we introduce a coordinate system on M by giving at any point the radial and angular coordinates of the shell's projection onto the plane, as depicted in Fig. 16, and state the radii of curvature R_r and R_α along the r and α coordinate lines. Choosing the normal vector to the surface to always point away from the inner corpus, we take the radius of curvature to be positive (respectively, negative) if the surface curves away from (respectively, towards) the normal vector. Thus, the spherical geometry is described by two positive radii of curvature ($R_\alpha, R_r > 0$), the inverted sphere is described by two negative radii of curvature ($R_r, R_\alpha < 0$), and the hyperbolic geometry is described by $R_\alpha > 0$ and $R_r < 0$; see Fig. 17.
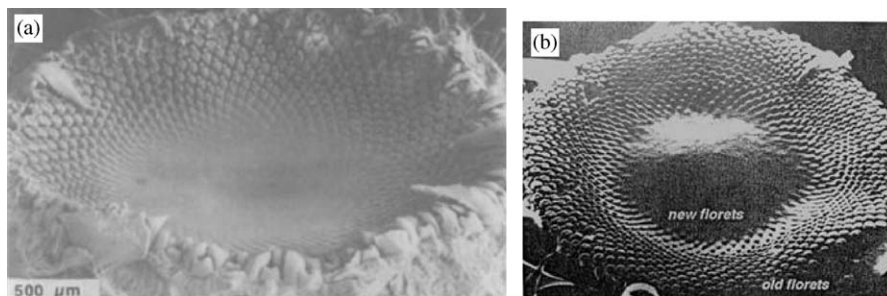

Fig. 15. Microscopic images of the generative region of a sunflower reveal either (a) an inverted disk (taken from Palmer (1998)) or (b) a hyperbolic geometry (taken from Steele (2000)).

As a consequence of the compressive stresses induced by growth, the annular shell M buckles. In this initial model, we assume that the shell is elastic so that the configuration into which the shell buckles is that which minimizes the elastic energy. Elastic materials are those for which deformations are reversible. A true plant will have plastic or viscoelastic influences that produce an irreversibility. In this model, we include irreversibility by simply treated the elastic shell as being strongly over-damped. Our goal now is to identify those buckling configurations which minimize the elastic energy.

Once we have identified the energy-minimizing con-figurations, we will have expressions for the normal deflection $\omega(r, \alpha)$ of the tunica shell in the generative region and the corresponding stress distribution. The deformation ω is our theoretical computation of the primordial ridges or bumps that subsequently develop into phylla. The primordial deformation ω will be periodic in the radial coordinate r. If we assume that the pattern formed in the generative region remains the same as the buckled tunica hardens and moves away from the plant tip, then the pattern that develops on the plant is given by plotting the function $\omega(s, \alpha)$ over numerous periods. Here, s is defined to be $s = r$ or $s = \ln(r)$, depending on whether the movement of the phylla from the apex is constant or exponential. If $s = r$, the plant exhibits the plastochrone difference, and if $s = \ln(r)$, the plant exhibits the plastochrone ratio. We will henceforth use r to represent the radial coordinate if we

are restricting our attention to the generative region (i.e., in Section 3) and use s when we are considering the pattern beyond the generative region.

Besides the growth that leads to the movement of phylla away from the apex, there is another growth that is essential to our model—the growth in the width of the apex, as measured by R, the inner radius of the generative region. Thus, a graph of $\omega(s, \alpha)$ will only represent the pattern formed on a plant if R remains constant. Otherwise, $\omega(s, \alpha)$ will also depend on R; typically, R increases as the plant gets older, so the larger values of s correspond to lower values of R. Finally, we emphasize, as do Dumais and Steele (2000), that, although the energy-minimizing buckling config-uration can serve as a guide to the patterns we expect to see, it is not correct to equate this configuration with the plant pattern. The amplitude of ω is of the order of the tunica thickness, and, as the primordial bumps grow into phylla, the stress distributions change and other biological processes come into play. For some plants more than for others, the primordia formed in the generative region will continue to develop further in shape. We will discuss this further in Section 5. A larger discussion of factors that are involved in SAM development is found in the well written review of Kwiatkowska (2004).

3. Analysis of the shell-buckling model

This section presents mathematical details, the ex-pression for the elastic energy of a curved annular shell tied to an elastic foundation, the FvKD equations, the linear stability analysis of the uniformly compressed shell solution, and finally the weakly nonlinear analysis governing the competition between all feasible plan-forms in which we identify energy-minimizing config-urations. The reader may wish to skip this section on a first reading of the paper. The following Section 4, in which we present arguments for our picture of plant patterns, should be accessible without having digested the details of Section 3. The outline of this section is as follows: In Section 3.1, we state the elastic energy and
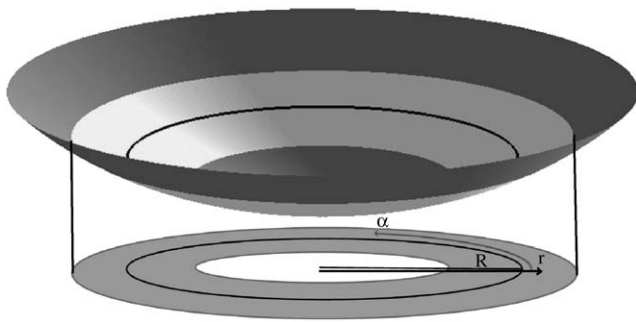
Fig. 16. Projecting the generative region to the plane, we define radial r and angular α coordinates.
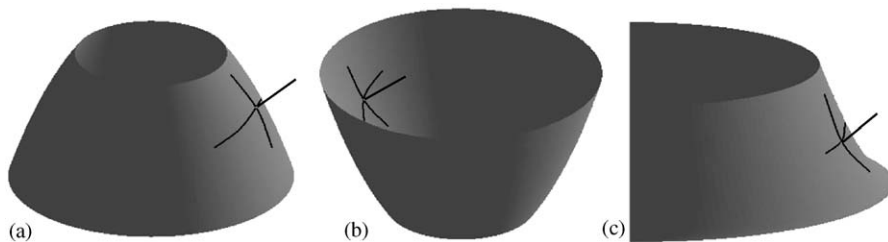
Fig. 17. The radii of curvature. The sign of the radius is taken to be positive if the surface curves towards the inner corpus and negative if it curves away from the inner corpus. Hence, (a) for the sphere $R_\alpha > 0$, $R_r > 0$, (b) for the inverted sphere, $R_\alpha < 0$, $R_r < 0$, and (c) for the hyperbolic region, $R_\alpha > 0$, $R_r < 0$.

the FvKD equations which are the Euler–Lagrange equations for this energy. We then find, via linear stability analysis in Section 3.2, the set of *active modes* which are unstable or weakly damped for large enough compressive stress. Finally, in Section 3.3, we study the nonlinear competition between the active modes. This allows us to reduce the elastic energy to a polynomial function of the amplitudes of the active modes; it is this reduced energy that we study in Section 4 to find energy-minimizing configurations.

3.1. The elastic energy and the FvKD equations

In Section 2.4, we described our model of the region of pattern formation on a plant as a thin annular shell M of mean radius R attached to an elastic foundation and under compressive stress due to growth. We coordinatized M with radial r and angular α coordinates and described the curvature of the shell via radii of curvature R_r and R_α. The elastic energy is a functional of in-plane stresses and the normal deflection $\omega(r, \alpha)$ of the shell. Assuming that the stresses are constant through the width of the shell, we solve for the tensor $N_{ij} = h\sigma_{ij}$, where σ_{ij} is the tensor of in-plane stresses and h is the width of the tunica shell. We can introduce a potential $F(r, \alpha)$ for the tensor N_{ij}, called the Airy stress function, and defined so that

$$N_{\alpha\alpha} = \frac{\partial^2 F}{\partial r^2}, \quad N_{\alpha r} = -\frac{1}{R}\frac{\partial^2 F}{\partial r \partial \alpha}, \quad N_{rr} = \frac{1}{R^2}\frac{\partial^2 F}{\partial \alpha^2}. \quad (25)$$

Assuming that the radius R is large compared to the buckling wavelength, we approximate the Laplacian on the manifold M by the Euclidean Laplacian $\Delta \equiv \partial_r^2 + \frac{1}{R^2}\partial_\alpha^2$. Working with this translationally invariant approximation does not compromise the results and greatly simplifies the analysis because the eigenfunctions of the Euclidean Laplacian are sines and cosines. The elastic energy as a functional of ω and F then reads

$$\mathfrak{E} = \int_M \left[\begin{array}{l} \frac{D}{2}\{(\Delta\omega)^2 - (1-\mu)[w, w]\} + V(\omega) \\[6pt] -\frac{1}{2Eh}\{(\Delta F)^2 - (1+\mu)[F, F]\} \\[6pt] + F\left(\Delta_c\omega - \frac{1}{2}[\omega, \omega]\right) \end{array} \right] R\,dr\,d\alpha, \quad (26)$$

where $\Delta_c \equiv \frac{1}{R_\alpha}\partial_r^2 + \frac{1}{R_r}\frac{1}{R^2}\partial_\alpha^2$, and $R^2[F, \omega] = F_{rr}\omega_{\alpha\alpha} + F_{\alpha\alpha}\omega_{rr} - 2F_{\alpha r}\omega_{r\alpha}$. The energy consists of the following terms: the first term in Eq. (26) resists buckling and is the bending energy of the shell. The bending modulus is $D = \frac{Eh^3}{12(1-\mu^2)}$, where E is Young's modulus and μ is Poisson's ratio. $V(\omega)$ is a potential energy coming from the elastic foundation and an applied stress from tunica growth; we take $V(\omega) = \frac{\kappa}{2}\omega^2 + \frac{\gamma}{4}\omega^4 - p\omega$ for spring constants κ and γ and applied pressure p. The third term is the energy of the in-plane stresses, and the remaining term is a strain energy which is equal to the product of the Airy stress function and the change in Gaussian curvature of the shell due to buckling.

We assume that the tunica is an overdamped shell and thus ignore the inertial accelerations ω_{tt} compared to the damping ω_t. The variation $\zeta\omega_t = -\frac{\delta\mathfrak{E}}{\delta\omega}$ (where ζ is an inverse time constant) of the energy with respect to ω yields the force equilibrium equation

$$\zeta\omega_t + D\Delta^2\omega + V'(\omega) + \Delta_c F - [F, \omega] = 0 \quad (27)$$

and the variation $0 = \frac{\delta\mathfrak{E}}{\delta F}$ yields the compatibility condition

$$\frac{1}{Eh}\Delta^2 F - \Delta_c\omega + \frac{1}{2}[\omega, \omega] = 0. \quad (28)$$

We call Eqs. (27) and (28) the overdamped FvKD equations; see, for example (Atanakovich, 2000; Gould, 1999) for further details.

3.2. Linear stability analysis and non-dimensionalization

We now study the linear stability of the prebuckling, stressed tunica, given by the stationary solution

$$\omega_s = \text{constant}, \quad (29)$$

$$F_s = \frac{1}{2}N_{\alpha\alpha}r^2 + \frac{1}{2}N_{rr}R^2\alpha^2 \quad (30)$$

of Eqs. (27) and (28), where $N_{\alpha\alpha}$ and N_{rr} are such that $\frac{1}{R_\alpha}N_{\alpha\alpha} + \frac{1}{R_r}N_{rr} = -V'(\omega_s)$. The variations of ω about ω_s and F about F_s are found by substituting

$$\omega = \omega_s + w, \quad (31)$$

$$F = F_s + f \quad (32)$$

into Eqs. (27) and (28), and obtaining

$$\zeta w_t + D\Delta^2 w + V'(w) + \Delta_c F \\ - [F_s + f, \omega_s + w] = 0, \quad (33)$$

$$\frac{1}{Eh}\Delta^2 f - \Delta_c w + \frac{1}{2}[\omega_s + w, \omega_s + w] = 0, \quad (34)$$

where

$$[F_s + f, \omega_s + w] = [F_s, w] + [f, w] = N_{\alpha\alpha}\frac{1}{R^2}w_{\alpha\alpha} \\ + N_{rr}w_{rr} + [f, w]. \quad (35)$$

Defining $\chi \doteq \frac{N_{rr}}{N_{\alpha\alpha}}$, $\Delta_\chi \doteq \chi\partial_r^2 + \frac{1}{R^2}\partial_\alpha^2$, $\rho \doteq \frac{R_\alpha}{R_r}$, $\Delta_\rho \doteq \partial_r^2 + \frac{\rho}{R^2}\partial_\alpha^2$, and $N \doteq -N_{\alpha\alpha}$, the equations (33),(34) read

$$\zeta w_t + D\Delta^2 w + V'(w) + N\Delta_\chi w \\ - [f, w] + \frac{1}{R_\alpha}\Delta_\rho f = 0, \quad (36)$$

$$\frac{1}{Eh}\Delta^2 f - \frac{1}{R_\alpha}\Delta_\rho w + \frac{1}{2}[w, w] = 0. \quad (37)$$

We test the stability of the $w = f = 0$ solution by setting

$$w = \hat{w}e^{\sigma t}e^{i\vec{k}\cdot\vec{x}}, \tag{38}$$

$$f = \hat{f}e^{\sigma t}e^{i\vec{k}\cdot\vec{x}}, \tag{39}$$

where $\vec{k} = (l, m), \vec{x} = (r, \alpha)$, in (33),(34) and retaining only the linear terms. We obtain

$$\zeta\hat{w}\sigma + D\hat{\Delta}^2\hat{w} - N\hat{\Delta}_\chi\hat{w} + \kappa\hat{w} - \frac{1}{R_\alpha}\hat{\Delta}_\rho\hat{f} = 0, \tag{40}$$

$$\frac{1}{Eh}\hat{\Delta}^2\hat{f} + \frac{1}{R_\alpha}\hat{\Delta}_\rho\hat{w} = 0, \tag{41}$$

where $\hat{\Delta} = l^2 + \frac{1}{R^2}m^2$, $\hat{\Delta}_\rho = l^2 + \frac{\rho}{R^2}m^2$, and $\hat{\Delta}_\chi = \chi l^2 + \frac{1}{R^2}m^2$. Solving (41) for $\hat{f}$ and replacing the result into Eq. (40) yields the dispersion relation

$$\zeta\sigma(l, m) = -D\hat{\Delta}^2 + N\hat{\Delta}_\chi - \kappa - \frac{Eh}{R_\alpha^2}\frac{\hat{\Delta}_\rho^2}{\hat{\Delta}^2} \tag{42}$$

which gives the growth rate $\sigma(\vec{k}) = \sigma(l, m)$ of a perturbation (38),(39). Only for N above a critical value N_c are there modes (l, m) with positive growth rates. To find the value N_c, note that N_c is the smallest value of N for which there is a set of modes (l, m) for which $\sigma(l, m) = 0$. That is, N_c is the minimum of

$$N = \frac{1}{\hat{\Delta}_\chi}\left(D\hat{\Delta}^2 + \kappa + \frac{Eh}{R_\alpha^2}\frac{\hat{\Delta}_\rho^2}{\hat{\Delta}^2}\right) \tag{43}$$

as a function of $\vec{k} = (l, m)$. In the isotropic case $\chi = 1, \rho = 1$, the minimum value $N_c = 2\sqrt{D}\sqrt{\kappa + \frac{Eh}{R_\alpha^2}}$ is achieved for $\hat{\Delta} = \sqrt{\frac{\kappa + \frac{Eh}{R_\alpha^2}}{D}}$. We call the modes with zero growth rates for $N = N_c$ the critical modes, and k_c, where $k_c^2 = \sqrt{\frac{\kappa + \frac{Eh}{R_\alpha^2}}{D}}$ the critical wavenumber. Thus, as the stress parameter N increases above N_c, it is modes of wavelength $2\pi\Lambda = \frac{2\pi}{k_c}$ that are first excited. The *natural wavelength* is $2\pi\Lambda$, where

$$\Lambda^4 = \frac{D}{\kappa + \frac{Eh}{R_\alpha^2}}. \tag{44}$$

In subsequent analysis, we will work with non-dimensionalized FvKD equations with scales determined by the natural wavelength for the isotropic case $\chi = 1$, $\rho = 1$. We define $v^2 \doteq \frac{1}{12(1-\mu^2)}$, $\Gamma \doteq \frac{R}{\Lambda}$, $C \doteq \frac{\Lambda^2}{R_\alpha hv}$, $P \doteq -\frac{N_\alpha\Lambda^2}{Eh^3v^2}$, and $T = \frac{\Lambda^4\zeta}{Eh^3v^2}$ and write $f = vEh^3f'$, $w = hw'$, $r = \Lambda r'$, $t = Tt'$, $\kappa = \frac{Eh^3v^2}{\Lambda^4}\kappa'$, $\gamma = \frac{Ehv^2}{\Lambda^4}\gamma'$. Upon dropping the primes, the FvKD equations are
$$w_t + \Delta^2 w + \kappa w + \gamma w^3 + P\Delta_\chi w$$
$$+ C\Delta_\rho f - \frac{1}{v\Gamma^2}[f, w] = 0, \tag{45}$$

$$\Delta^2 f - C\Delta_\rho w + \frac{1}{2v\Gamma^2}[w, w] = 0, \tag{46}$$

where $\Delta = \partial_r^2 + \frac{1}{\Gamma^2}\partial_\alpha^2$, $\Delta_\rho = \partial_r^2 + \frac{\rho}{\Gamma^2}\partial_\alpha^2$, and $\Delta_\chi = \chi\partial_r^2 + \frac{1}{\Gamma^2}\partial_\alpha^2$. Note that the parameter Γ can be hidden in the equations by scaling $\alpha \mapsto \frac{1}{\Gamma}\alpha$. Also, by definition, $C^2 + \kappa = \frac{\Lambda^4}{Eh^3v^2}(\kappa + \frac{Eh}{R_\alpha^2}) = 1$. The equations in Section 3.2 are the variational equations $\zeta w_t = -\frac{\delta\mathfrak{E}}{\delta w}$, $0 = -\frac{\delta\mathfrak{E}}{\delta F}$ of the energy

$$\mathfrak{E}(w,f) = \int \left[\begin{array}{l} \frac{1}{2}(\Delta w)^2 + V(w) - \frac{1}{2}P\left(\chi\partial_r w + \frac{1}{\Gamma^2}\partial_\alpha w\right)^2 \\ + f\left(C\Delta_\rho w - \frac{1}{2v\Gamma^2}[w, w]\right) - \frac{1}{2}(\Delta f)^2 \end{array} \right]$$
$$\times \, dr \, d\alpha, \tag{47}$$

where $V(w) = \frac{\kappa}{2}w^2 + \frac{\gamma}{4}w^4$. The dispersion relation for the non-dimensionalized equations (Section 3.2) reads

$$\sigma(l, m) = -\hat{\Delta}^2 + P\hat{\Delta}_\chi - \kappa - C^2\frac{\hat{\Delta}_\rho^2}{\hat{\Delta}^2}, \tag{48}$$

where now $\hat{\Delta} = (l^2 + \frac{1}{\Gamma^2}m^2)$, $\hat{\Delta}_\chi = (\chi l^2 + \frac{1}{\Gamma^2}m^2)$, and $\hat{\Delta}_\rho = (l^2 + \frac{\rho}{\Gamma^2}m^2)$. For the isotropic case $\chi = \rho = 1$, σ first becomes positive on the locus

$$l^2 + \frac{1}{\Gamma^2}m^2 = 1 \tag{49}$$

at the stress value $P = P_c = 2$. For the case that we are most interested in, namely $\rho = 1$ and $\chi < 1$, $\sigma(l, m)$ first becomes positive for $\vec{k}_c = (0, \Gamma)$ at the value $P = P_c = 2$. For $P > P_c$, there is a set of modes in the (l, m)-plane for which $\sigma(l, m) > 0$. We shall call the set of modes for which $\sigma(l, m)$ is greater than a small negative number the set $\mathfrak{A}$ of *active modes*; see the discussion in Section 4.3. In Section 4 we will describe how the set of active modes depends on the parameters. In particular, we distinguish between two cases, namely ρ positive, corresponding to M's being elliptic, as in Fig. 14(a and b), and ρ negative, corresponding to M's being hyperbolic, as is Fig. 14(c).

If, for the linearization of the equations (36),(37), we write

$$w = \sum_{\vec{k} \in A}(A_{\vec{k}}(t)e^{i\vec{k}_j\cdot\vec{x}} + \text{c.c}), \quad \vec{k} = (l, m),$$

$$f = \sum_{\vec{k} \in A}\left(-C\frac{(l^2 + \frac{\rho}{\Gamma^2}m^2)}{(l^2 + \frac{1}{\Gamma^2}m^2)^2}A(t)e^{i\vec{k}\cdot\vec{x}} + \text{c.c}\right), \tag{50}$$

we obtain the linear equations

$$\frac{dA_{\vec{k}}}{dt} = \sigma(\vec{k})A_{\vec{k}} \tag{51}$$

for the amplitudes $A_{\vec{k}}(t)$, where $\sigma(\vec{k}) = \sigma(l, m)$ is as given by Eq. (48). To see this, write the linearization of the

equations (36),(37) as

$$
L\begin{pmatrix} w \\ f \end{pmatrix} = \begin{pmatrix} \Delta^2 + \kappa + P\Delta_\chi & C\Delta_\rho \\ -C\Delta_\rho & \Delta^2 \end{pmatrix} \begin{pmatrix} w \\ f \end{pmatrix}
$$

$$
= -\begin{pmatrix} w_t \\ 0 \end{pmatrix}. \tag{52}
$$

For each wavevector $\vec{k} = (l, m) \in A$, define $P_c(\vec{k})$ to be the minimum value of P for which $\sigma(l, m)$ is zero. Note that $P_c = \min_{\vec{k}} P_c(\vec{k})$. For example, when $\rho = 1, \chi < 1$, the mode $\vec{k}_c = (0, \Gamma)$ has a corresponding $P_c(\vec{k}_c) = P_c = 2$. Now write $\hat{w}_{\vec{k}} = A_{\vec{k}}$ and $f_{\vec{k}} = -C\frac{\Delta_\rho}{\Delta^2} A_{\vec{k}}$, and note that

$$
\hat{L}_{\vec{k}}\begin{pmatrix} \hat{w}_{\vec{k}} \\ \hat{f}_{\vec{k}} \end{pmatrix} = \begin{pmatrix} \hat{\Delta}^2 + \kappa - P_c(\vec{k})\hat{\Delta}_\chi & -C\hat{\Delta}_\rho \\ C\hat{\Delta}_\rho & \hat{\Delta}^2 \end{pmatrix} \begin{pmatrix} \hat{w}_{\vec{k}} \\ \hat{f}_{\vec{k}} \end{pmatrix}
$$

$$
= \begin{pmatrix} 0 \\ 0 \end{pmatrix}, \tag{53}
$$

where $\vec{k} = (l, m)$, $\hat{\Delta} = (l^2 + \frac{1}{\Gamma^2}m^2)$, $\hat{\Delta}_\rho = (l^2 + \frac{\rho}{\Gamma^2}m^2)$, and $\hat{\Delta}_\chi = (\chi l^2 + \frac{1}{\Gamma^2}m^2)$. The right eigenvector of $\hat{L}_{\vec{k}}$ corresponding to the eigenvalue 0 is $(1, -C\frac{\hat{\Delta}_\rho}{\hat{\Delta}^2})$. The left eigenvector is $(1, C\frac{\hat{\Delta}_\rho}{\hat{\Delta}^2})$. Now, for each mode $e^{i\vec{k}\cdot\vec{x}}$, write Eq. (53) as

$$
\hat{L}_{\vec{k}}\begin{pmatrix} \hat{w}_{\vec{k}} \\ \hat{f}_{\vec{k}} \end{pmatrix} = \begin{pmatrix} (P - P_c(\vec{k}))\hat{\Delta}_\chi & 0 \\ 0 & 0 \end{pmatrix} \begin{pmatrix} \hat{w}_{\vec{k}} \\ \hat{f}_{\vec{k}} \end{pmatrix}
$$

$$
- \begin{pmatrix} \hat{w}_{\vec{k}t} \\ 0 \end{pmatrix}. \tag{54}
$$

Multiply by the left eigenvector of $L_{\vec{k}}$ to obtain

$$
(P - P_c(\vec{k}))\left(\chi l^2 + \frac{1}{\Gamma^2}m^2\right) A_{\vec{k}} = A_{\vec{k}t} \tag{55}
$$

with growth rate $\sigma(\vec{k}) = P\hat{\Delta}_\chi - P_c(\vec{k})(\chi l^2 + \frac{1}{\Gamma}m^2)$, which, by definition of $P_c(\vec{k})$, is $\sigma(l, m)$.

3.3. Nonlinear analysis

We now ask what happens when the compressive stress P is supercritical;

$$
P = P_c(1 + \varepsilon P'),
$$

where $0 < \varepsilon \ll 1$, $P' > 0$, and several of the active modes begin to interact with each other via the quadratic and cubic terms in Section 3.2. The important quadratic interactions are those between triads of modes $e^{i\vec{k}_j\cdot\vec{x}}$, $j = 1, 2, 3$, $\vec{k}_j = (l_j, m_j)$ for which $\vec{k}_1 + \vec{k}_2 + \vec{k}_3 = 0$. These interactions lead to a set of nonlinear equations for the amplitudes $A_j(t)$ of those modes $e^{i\vec{k}_j\cdot\vec{x}}$ which we include in the representation of the deformation $w(r, \alpha, t)$. The included modes $\vec{k}_j$ belong to the set $\mathfrak{A}$ of modes for

which the corresponding growth rate $\sigma(\vec{k}_j)$ is greater than a small (order ε) negative number. This means that $\mathfrak{A}$ includes amplified, neutral and weakly damped modes. The reason the latter should be included is that sometimes, because of quadratic nonlinear interactions which involve excited modes, these weakly damped modes can be nonlinearly driven and play a role in determining the final configuration of the deformation.

The analysis proceeds formally as follows: we define a slow time-scale $t_1 = \varepsilon t$, and represent w and f by asymptotic series in ε as

$$
w(r, \alpha, t_1) = \varepsilon w_0 + \varepsilon^2 w_1 + \varepsilon^3 w_2 + \cdots,
$$

$$
f(r, \alpha, t_1) = \varepsilon f_0 + \varepsilon^2 f_1 + \varepsilon^3 f_2 + \cdots, \tag{56}
$$

where w_0 and f_0 are given by Eq. (50). The equations for the iterates w_1, f_1 are determined by substituting the expansions (56) in Section 3.2 and equating powers of ε. To order ε^2, we find that

$$
L\begin{pmatrix} \varepsilon w_0 + \varepsilon^2 w_1 \\ \varepsilon f_0 + \varepsilon^2 f_1 \end{pmatrix} = -\begin{pmatrix} \varepsilon^2 w_{t_1} \\ 0 \end{pmatrix}
$$

$$
+ \varepsilon^2 \begin{pmatrix} \frac{1}{v\Gamma^2}[f_0, w_0] \\ -\frac{1}{2v\Gamma^2}[w_0, w_0] \end{pmatrix}. \tag{57}
$$

Noting that, for each $\vec{k} \in A$,

$$
\begin{pmatrix} \Delta^2 + \kappa + P_c(\vec{k})\Delta_\chi & C\Delta_\rho \\ -C\Delta_\rho & \Delta^2 \end{pmatrix}
$$

$$
\times \begin{pmatrix} 1 \\ -C\frac{\hat{\Delta}_\rho}{\hat{\Delta}^2} \end{pmatrix} e^{i\vec{k}\cdot\vec{x}} = \begin{pmatrix} 0 \\ 0 \end{pmatrix}, \tag{58}
$$

we can rewrite Eq. (57) as

$$
L\begin{pmatrix} w_1 \\ f_1 \end{pmatrix} = \sum_{k \in A} \begin{pmatrix} \frac{1}{\varepsilon}(P - P_c(\vec{k}))\Delta_\chi(A_{\vec{k}}e^{i\vec{k}\cdot\vec{x}}) - (A_{\vec{k}t_1}e^{i\vec{k}\cdot\vec{x}}) \\ 0 \end{pmatrix}
$$

$$
+ \frac{1}{2v\Gamma^2}\begin{pmatrix} 2[f_0, w_0] \\ -[w_0, w_0] \end{pmatrix}. \tag{59}
$$

Since P is within ε of $P_c(\vec{k})$ for all $\vec{k} \in A$, the solution to Eq. (59) will be of order ε^{-1} unless we apply a solvability condition to the RHS of Eq. (59). That solvability condition is that, for all terms of the form $\vec{v}_{\vec{k}}e^{i\vec{k}\cdot\vec{x}}$ on the RHS of Eq. (59), the vector $\vec{v}_{\vec{k}}$ must be orthogonal to the left eigenvector of $\hat{L}_{\vec{k}}$, namely $(1, C\frac{l^2 + \frac{\rho}{\Gamma^2}m^2}{(l^2 + \frac{1}{\Gamma^2}m^2)^2})$. The

quadratic terms in Eq. (59) are computed to be

$[f_0, w_0] = -C$

$$\times \begin{pmatrix} \text{terms} & (l_r m_s - l_s m_r)^2 \frac{l_r^2 + \frac{\rho}{\Gamma^2} m_r^2}{(l_r^2 + \frac{1}{\Gamma^2} m_r^2)^2} A_r A_s e^{i(\mathbf{k}_r + \mathbf{k}_s) \cdot \mathbf{x}} \\ \text{of the} & (l_r m_s - l_s m_r)^2 \frac{l_r^2 + \frac{\rho}{\Gamma^2} m_r^2}{(l_r^2 + \frac{1}{\Gamma^2} m_r^2)^2} A_r A_s^* e^{i(\mathbf{k}_r - \mathbf{k}_s) \cdot \mathbf{x}} \\ \text{form} & (l_r m_s - l_s m_r)^2 \frac{l_r^2 + \frac{1}{\Gamma^2} m_r^2}{(l_r^2 + \frac{1}{\Gamma^2} m_r^2)^2} A_r^* A_s^* e^{i(-\mathbf{k}_r - \mathbf{k}_s) \cdot \mathbf{x}} \\ & r, s \in \{1, 2, 3\} \end{pmatrix},$$

$$[w_0, w_0] = \begin{pmatrix} \text{terms} & (l_r m_s - l_s m_r)^2 A_r A_s e^{i(\mathbf{k}_r + \mathbf{k}_s) \cdot \mathbf{x}} \\ \text{of the} & (l_r m_s - l_s m_r)^2 A_r A_s^* e^{i(\mathbf{k}_r - \mathbf{k}_s) \cdot \mathbf{x}} \\ \text{form} & (l_r m_s - l_s m_r)^2 A_r^* A_s^* e^{i(-\mathbf{k}_r - \mathbf{k}_s) \cdot \mathbf{x}} \\ & r, s \in \{1, 2, 3\} \end{pmatrix}.$$

$$(60)$$

Applying the solvability condition to Eq. (59), we therefore obtain

$$A_{\vec{k}t_1} = \frac{1}{\varepsilon} \sigma(\vec{k}) A_{\vec{k}} + \sum_{\vec{k}_r + \vec{k}_s + \vec{k} = 0} \tau(\vec{k}_r, \vec{k}_s, \vec{k}) A_r^* A_s^*, \quad (61)$$

where

$$\tau(\vec{k}_1, \vec{k}_2, \vec{k}_3 = -\vec{k}_1 - \vec{k}_2) = -\frac{C}{v \Gamma^2} (l_1 m_2 - l_2 m_1)^2 \\ \times \sum_{j=1}^3 \frac{l_j^2 + \frac{\rho}{\Gamma^2} m_j^2}{(l_j^2 + \frac{1}{\Gamma^2} m_j^2)^2}. \quad (62)$$

Since $\vec{k}_1 + \vec{k}_2 + \vec{k}_3 = 0$, $l_1 m_2 - l_2 m_1 = l_2 m_3 - l_3 m_2 = l_3 m_1 - l_1 m_3$. Eq. (61) have no finite attracting fixed points. The reason for this is that the quadratic terms only transfer energy delivered to the deformation by the supercritical stress. Saturation is achieved by cubic terms, principally from the term γw^3 from the nonlinear foundation. We take γ sufficiently large so that $\varepsilon\gamma$ is of the same order as $\frac{1}{\varepsilon}\sigma$, namely of order unity. Then additional terms must be added to Eq. (61) to give (after scaling $A_j \mapsto \frac{1}{\varepsilon} A_j$)

$$A_{\vec{k}t} = \sigma(\vec{k}) A_{\vec{k}} + \sum_{\vec{k}_r + \vec{k}_s + \vec{k} = 0} \tau(\vec{k}_r, \vec{k}_s, \vec{k}) A_r^* A_s^* \\ - 3\gamma A_{\vec{k}} \left(|A_{\vec{k}}|^2 + 2 \sum_{\vec{k}_l \neq \vec{k}} |A_l|^2 \right). \quad (63)$$

The amplitude equations (63) are a gradient system;

$$\frac{\partial A_{\vec{k}}}{\partial t} = -\frac{\delta \mathfrak{E}}{\delta A_{\vec{k}}}, \quad (64)$$

where the scaled and non-dimensional elastic energy, projected onto the modes $e^{i\vec{k} \cdot \vec{x}}$, $\vec{k} \in A$, is

$$\mathfrak{E}(\vec{k} \in A, A_{\vec{k}}) \\ = -\sum_{\vec{k} \in A} \sigma(\vec{k}) A_{\vec{k}} A_k^* - \sum_{\vec{k}_r + \vec{k}_s + \vec{k}_j = 0} \tau(\vec{k}_r, \vec{k}_s, \vec{k}_j) \\ \times (A_r A_s A_j + A_r^* A_s^* A_j^*) \\ + 3\gamma \left(\sum_{\vec{k}_j \in A} \frac{1}{2} |A_j|^2 + 2 \sum_{k_l \neq k_j} |A_j|^2 |A_l|^2 \right). \quad (65)$$

As Eq. (63) is a gradient flow, all the attracting solutions are fixed points. These fixed points are minimizers of the elastic energy (65). We will discuss these fixed points and the elastic energy landscape as a function of the physical parameters and the phyllotactic coordinates $2\pi d$, λ, m, and n in Section 4. Here, we will simply recall some properties of Eq. (63) in the case where $\mathfrak{A}$ contains three modes $\vec{k}_1, \vec{k}_2, \vec{k}_3$, where $\vec{k}_1 + \vec{k}_2 + \vec{k}_3 = 0$ or four modes $\vec{k}_1, \vec{k}_2, \vec{k}_3, \vec{k}_4$, where $\vec{k}_1 + \vec{k}_2 = \vec{k}_3$ and $\vec{k}_2 + \vec{k}_3 = \vec{k}_4$.

3.4. Solutions of the amplitude equations

3.4.1. Amplitude equations including three modes

In this section, we discuss stability of solutions of the amplitude equations (63) in the simplest case in which there are only three active modes $A_1 e^{i\vec{k}_1 \cdot \vec{x}}$, $A_2 e^{i\vec{k}_2 \cdot \vec{x}}$, and $A_3 e^{i\vec{k}_3 \cdot \vec{x}}$ such that $\vec{k}_1 + \vec{k}_2 = \vec{k}_3$. The amplitude equations then read

$$\zeta \frac{\partial A_1}{\partial t} = \sigma(\vec{k}_1) A_1 + \tau(\vec{k}_1, \vec{k}_2, \vec{k}_3) A_2^* A_3 \\ - 3\gamma A_1 (A_1 A_1^* + 2 A_2 A_2^* + 2 A_3 A_3^*),$$

$$\zeta \frac{\partial A_2}{\partial t} = \sigma(\vec{k}_2) A_2 + \tau(\vec{k}_1, \vec{k}_2, \vec{k}_3) A_1^* A_3 \\ - 3\gamma A_2 (A_2 A_2^* + 2 A_1 A_1^* + 2 A_3 A_3^*),$$

$$\zeta \frac{\partial A_3}{\partial t} = \sigma(\vec{k}_3) A_3 + \tau(\vec{k}_1, \vec{k}_2, \vec{k}_3) A_1 A_2 \\ - 3\gamma A_3 (A_3 A_3^* + 2 A_1 A_1^* + 2 A_2 A_2^*). \quad (66)$$

The system (66) has the following stationary solutions in the case $\sigma(\vec{k}_1) = \sigma(\vec{k}_2) = \sigma(\vec{k}_3) \doteq \sigma$ that are stable for certain choices of the ratio $\xi = \frac{\sigma\gamma}{\tau^2}$:

I. *Zero solution*: $A_1 = A_2 = A_3 = 0$,

stable for $\xi < 0$, unstable for $\xi > 0$.

II. *Ridge solutions*: $A_1 = \pm\sqrt{\frac{\sigma}{3\gamma}}$, $A_2 = 0 = A_3$,

$$A_2 = \pm\sqrt{\frac{\sigma}{3\gamma}}, \quad A_1 = 0 = A_3,$$

$$A_3 = \pm\sqrt{\frac{\sigma}{3\gamma}}, \quad A_1 = 0 = A_2,$$

stable for $\xi > 1$, unstable for $\xi < 1$.

III. *Hexagon solutions*: $A_j = a\mathrm{e}^{\phi_j}, \phi_1 + \phi_2 + \phi_3 = n\pi,$
$n \in \mathbf{Z}, a^{\pm} = \frac{\tau \pm \sqrt{\tau^2 + 60\sigma\gamma}}{30\gamma}$

for even n, a^+ is stable for $\xi < \frac{4}{3}$.

for odd n, a^- is stable for $\xi < \frac{4}{3}$.

In the following, we will be interested in the case $\sigma(\vec{k}_1) = \sigma(\vec{k}_2) < \sigma(\vec{k}_3)$ so that $\xi_1 = \xi_2 \doteq \xi < \xi_3$, where $\xi_j = \frac{\sigma(k_j)\gamma}{\tau^2}$. The stability of ridge and hexagon solutions in this case is as follows; details can be found in (Kücken, 2004):

I. *Ridge solution type* I: $A_1 = \pm\sqrt{\frac{\sigma}{3\gamma}}, A_2 = 0 = A_3$,

$A_2 = \pm\sqrt{\frac{\sigma}{3\gamma}}, \quad A_1 = 0 = A_3,$

stable for $\xi > \frac{1 + \xi_3}{2}$.

This solution is of little interest as it is not reached in the context of plants.

II. *Ridge solution type* II: $A_3 = \pm\sqrt{\frac{\sigma_3}{3\gamma}}, A_1 = 0 = A_2$,

stable for $\xi < 2\xi_3 - \sqrt{\xi_3}$.

This is one of the two most interesting solutions. It corresponds to a purely circumferential mode $a_3 \cos \Gamma\alpha$, where Γ is an integer. It is stable if the quadratic coupling coefficient τ is small, a situation which is obtained when the tunica curvature is small.

III. *Hexagon solutions*: $A_j = a_j\mathrm{e}^{\phi_j}, \phi_1 + \phi_2 + \phi_3 = 0$,

$a^2 = \frac{\sigma + \tau a_3 - 2\gamma a_3^2}{3\gamma},$

$5\gamma^2 a_3^3 - 6\tau\gamma a_3^2 + (3\gamma\sigma_3 - 4\gamma\sigma + \tau^2)a_3 + \tau\sigma = 0,$

stable for $10a_3^3 - 6a_3^2 < \xi < 2a_3^2 + a_3$.

This is the second interesting solution. It corresponds to the case when the quadratic coupling coefficient is strong enough to destabilize the purely circumferential mode which is, linearly, amplified the most. The solution has a deformation which is shown in Fig. 5(b) and is hexagonal in shape.

3.4.2. Amplitude equations including four modes

We have argued in the overview, and will expand our discussion in Section 4, that bias will lead to solutions consisting of two (or even three) overlapping wavevector triads $\vec{k}_1, \vec{k}_2, \vec{k}_3 = \vec{k}_1 + \vec{k}_2$ and $\vec{k}_2, \vec{k}_3, \vec{k}_4 = \vec{k}_2 + \vec{k}_3$ (and $\vec{k}_3, \vec{k}_4, \vec{k}_5 = \vec{k}_3 + \vec{k}_4$). The amplitude equations (65) for a deformation which is a linear combination of four modes read

$$\zeta \frac{\partial A_1}{\partial t} = \sigma(\vec{k}_1)A_1 + \tau_1 A_2^* A_3 - 3\gamma A_1(A_1 A_1^* + 2A_2 A_2^*$$
$$+ 2A_3 A_3^* + 2A_4 A_4^*),$$

$$\zeta \frac{\partial A_2}{\partial t} = \sigma(\vec{k}_2)A_2 + \tau_1 A_1^* A_3 + \tau_2 A_3^* A_4 - 3\gamma A_2(A_2 A_2^*$$
$$+ 2A_1 A_1^* + 2A_3 A_3^* + 2A_4 A_4^*),$$

$$\zeta \frac{\partial A_3}{\partial t} = \sigma(\vec{k}_3)A_3 + \tau_1 A_1 A_2 + \tau_2 A_2^* A_4 - 3\gamma A_3(A_3 A_3^*$$
$$+ 2A_1 A_1^* + 2A_2 A_2^* + 2A_4 A_4^*),$$

$$\zeta \frac{\partial A_4}{\partial t} = \sigma(\vec{k}_4)A_4 + \tau_2 A_2 A_3 - 3\gamma A_4(A_4 A_4^* + 2A_1 A_1^*$$
$$+ 2A_2 A_2^* + 2A_3 A_3^*). \tag{67}$$

In the case $\sigma(\vec{k}_1) = \sigma(\vec{k}_2) = \sigma(\vec{k}_3) = \sigma(\vec{k}_4)$, this system has a solution in which the outer modes have equal amplitude $A_1 = A_4$ which are roots of $63\gamma^2 x^3 - 36\gamma\tau x^2 + (2\tau^2 - 3\sigma\gamma)x + \tau\sigma$ and the inner two modes have equal amplitudes $A_2 = A_3 = \pm\frac{1}{3}\sqrt{\frac{\sigma + 2\tau A_1 - 2\gamma A_1^2}{\gamma}}$; an example of such a deformation is shown in Fig. 5(c).

The exact solutions discussed here serve as guides. In most cases, however, the growth rates $\sigma(\vec{k}_j)$ are not equal, and we must solve Eqs. (66), (67) using a Runga–Kutta 4 scheme. For example, we will be interested in the case $\sigma_2 \simeq \sigma_3 > \sigma_1 \simeq \sigma_4$ in Eq. (67), in which case we will find numerically solutions of the form $|A_2| \simeq |A_3| > |A_1| \simeq |A_4|$.

4. Energy-minimizing configurations

In the previous section, we analysed the elastic energy associated to a deformation $w = \sum_{\vec{k}} A_{\vec{k}} \mathrm{e}^{i\vec{k}\cdot\vec{x}} + \mathrm{c.c.}$ of the tunica surface in the generative region, where, for radial r and angular α coordinates, $\vec{x} = (r, \alpha)$ and $\vec{k}_j = (l_j, m_j)$, and $\vec{k}_j$ belongs to a set $\mathfrak{A}$ of active modes to be determined in Section 4.2 (recall that we use the coordinate r when our attention is restricted to the generative region and s otherwise). That energy, when averaged over the compressed annular band of the tunica, has the form of a real polynomial in the complex amplitudes A_j whose coefficients depend on certain dimensionless material and geometric parameters introduced in Section 3.2;

$$\mathfrak{E}(\vec{k} \in \mathfrak{A}, A_{\vec{k}})$$
$$= -\sum_{\vec{k} \in \mathfrak{A}} \sigma(\vec{k})A_{\vec{k}}A_{\vec{k}}^*$$
$$- \sum_{\vec{k}_r + \vec{k}_s = \vec{k}_j} \tau(\vec{k}_r, \vec{k}_s, \vec{k}_j)(A_r A_s A_j^* + A_r^* A_s^* A_j)$$
$$+ 3\gamma \left(\sum_{\vec{k}_j \in A} \frac{1}{2}|A_j|^2 + 2\sum_{k_l \neq k_j} |A_j|^2 |A_l|^2 \right). \tag{68}$$

The goal now is to find those deformations (that is, those wavevectors and associated amplitudes) that

minimize this elastic energy and how the minimizing deformations depend on the parameters. The relaxational dynamics of the amplitudes A_j and how they reach their energy-minimizing states is governed by the amplitude equations

$$\frac{\mathrm{d}A_j}{\mathrm{d}t} = -\frac{\partial \mathfrak{E}}{\partial A_j^*} = \sigma(\vec{k}_j)A_j + \sum_{\vec{k}_r+\vec{k}_s=\vec{k}_j} \tau(\vec{k}_r,\vec{k}_s,\vec{k}_j)A_rA_s$$
$$- 3\gamma\left(|A_j|^2 + 2\sum_{l \neq j}|A_l|^2\right)A_j. \qquad (69)$$

The effects of the bias of a previous pattern which has moved out of the generative region on the pattern about to form is captured by adding constants $\bar{A}_j$ to the amplitude equations for those modes which share circumferential wavenumbers with those of the previous pattern. These terms arise from the projection of the outer edge boundary conditions onto the set of active modes. They will add terms $\bar{A}_jA_j^* + \bar{A}_j^*A_j$ to the elastic energy (68). We use the dynamical equations (69) to follow the evolution of the amplitudes in order to be able to confirm that a particular minimizing configuration is accessible from the initial conditions. The pattern history, captured by the initial bias and the initial conditions which reflect the fading presence of the former pattern, determines which of the many possible minima the new pattern will realize. It will be a local minimum but may not be the absolute minimum. We will find, for example, that whereas configurations involving triads with angular wavenumbers $(N, N, 2N)$ or $(N, N+1, 2N+1)$ have the lowest minima, other combinations of triads are often realized.

Before we begin, we remind the reader of the warning issued in the overview. The expressions (68) and (69) are generic in the sense that almost every near-onset model sharing some overall symmetries with the picture we propose will give similar normal forms. From the pioneering work of Koiter (1963) on shell buckling and Busse (1967) on convection, it is known that, in overdamped situations, the system will relax to minima of an energy functional which is a polynomial in the amplitudes A_j of the fundamental shapes $\mathrm{e}^{\mathrm{i}\vec{k}_j\cdot\vec{x}}$ common to translationally invariant (read large aspect ratio; the wavelength to macroscopic length scale ratio is small) systems. It is also widely appreciated that, barring symmetries, such as $w \rightarrow -w$, which make the coupling coefficient τ zero, the triad interactions will dominate. For example, in systems which are also locally rotationally invariant, the preferred planform near onset consists of regular hexagons. Therefore, if we are to connect our model, based on the elastic deformation of an annular region of the tunica, to what is observed, we have to show that the particular coefficients $\sigma(\vec{k}_j)$ and $\tau(\vec{k}_r, \vec{k}_s, \vec{k}_{r+s} = \vec{k}_r + \vec{k}_s)$ have the properties which lead to the choices of phyllotactic lattices, transitions between lattices, and phylla shapes that are observed in nature.

As an outline of how the model gives rise to the various polygonal planforms and phyllotaxis, we summarize the results of the following subsections.

4.1: We begin by discussing the dimensionless parameters, which include material parameters describing properties of the tunica and corpus, stress parameters, and geometric parameters describing the shape of the apex.

We describe how the coefficients σ and τ depend on the parameters in 4.2 (σ) and 4.3 (τ).

4.2: The coefficient $\sigma(\vec{k})$ gives both the most linearly unstable planform and the set of active modes.

As the circumferential stress due to growth is larger than the radial stress, the most linearly unstable mode has the form $a_c\cos(m_c\alpha) = A_c\mathrm{e}^{\mathrm{i}\vec{k}_c\cdot\vec{x}} + A_c^*\mathrm{e}^{-\mathrm{i}\vec{k}_c\cdot\vec{x}}$ ($\vec{k}_c = (0, m_c)$, $a_c = 2|A_c|$, phase of $A_c = 0$), where m_c is the closest integer to the ratio $\Gamma = \frac{R}{\Lambda}$ of the mean radius R of the generative region to the natural wavelength Λ, determined by material properties of the tunica. Thus, purely circumferential ridges (as seen, for example, on a pumpkin) constitute the most linearly preferred planform.

The set $\mathfrak{A}$ of active modes is defined after examining the constant growth rate curves $\sigma(l, m)$ in the (l, m)-plane. This set must be allowed to include all modes which can possibly participate in the nonlinear competition. Some will even be linearly damped; that is, their growth rates will be weakly negative. They can still play vital roles as they can be nonlinearly driven via triad interactions with modes that are linearly amplified.

4.3: The cubic coupling coefficient $\tau(\vec{k}_1, \vec{k}_2, \vec{k}_3)$ is proportional to a parameter C measuring the curvature of the apex. Also, writing the wavevectors $\vec{k}_j$ in terms of the phyllotactic parameters d and λ, we show that τ is a sensitive function of d and a decreasing function of λ.

4.4: For curvature C above some critical value, the purely circumferential mode with wavevector $\vec{k}_c = (0, m_c)$ is unstable to a triad of modes $\vec{k}_N = (l, N)$, $\vec{k}_N = (l, N)$, $\vec{k}_c = (0, m_c = 2N)$ or $\vec{k}_N = (l, N)$, $\vec{k}_N = (l, N+1)$, $\vec{k}_c = (0, m_c = 2N+1)$ and positive amplitudes; this choice of wavevectors and amplitudes depends on the coefficients σ and τ. The case $m = 2N$ gives rise to the *alternating N-whorl* in which whorls of N primordia alternate in angle; for $N = 2$ this is the commonly observed decussate phyllotaxis (Fig. 2(c)).

For C just above the critical value at which ridges become unstable, the amplitude a_c of the mode with wavevector $\vec{k}_c$ is much larger than the amplitudes of the remaining two modes. In this case, the planform is almost that of purely circumferential ridges with small undulations; see Figs. 1(a) and 5(a). For larger C, the amplitudes of all three modes are close to the same value, and the planform is that of hexagons; see Figs. 1(b) and 5(b).

As Γ increases, the energy-minimizing triad configuration moves up the sequence of triads with radial wavenumbers $(N, N, 2N) \rightarrow (N, N+1, 2N+1) \rightarrow (N+1, N+1, 2(N+1)) \rightarrow \cdots$. These are sudden, Type I, transitions involving dislocations and penta–hepta defects (Fig. 24) in which only one radial wavenumber is preserved.

4.5: For large enough stress and curvature, more than one triad may be involved in the energy-minimizing configuration which is realizable. Imagine that we begin with a triad of modes with circumferential wavenumbers $(m, n, m + n)$ (e.g., (2,3,5)). We show how bias, namely the influence that a forming pattern feels from a previously formed pattern that has moved to the edge of the generative region favors the choice of the fourth mode $m + 2n$ over the mode $2m + n$ so that a configuration with amplitudes $|A_m|, |A_n|, |A_{m+n}|, |A_{m+2n}|$ is favored over one with amplitudes $|A_m|, |A_n|, |A_{m+n}|, |A_{2m+n}|$. This has the important consequence of giving rise to Fibonacci-like sequences as Γ increases. As Γ increases, the amplitude $|A_m|$ in a sequence $|A_m|, |A_n|, |A_{m+n}|, |A_{m+2n}|$ decreases as the amplitude $|A_{m+2n}|$ increases and a fifth amplitude $|A_{2m+3n}|$ becomes positive. Thus, for increasing Γ, the sequence of amplitudes moves up a Fibonacci-like sequence and usually contains four or five modes with the inner modes with larger amplitudes than the left, respectively, rightmost, modes diminishing (respectively, increasing) with Γ. This leads to Type II imperfect transitions, resulting in parallelogram shapes (Figs. 1(c) and 5(c)) when four modes are involved and staircase parallelograms (Figs. 1(d) and 5(d)) when five modes are involved.

Thus, we present a picture of how both bias and the presence of more than one triad are essential for Type II transitions. Without either of these effects, Type I transitions are preferred. Notice that this picture suggests that plants in which the dominant planform is that of ridges should undergo Type I transitions, whereas Type II transitions should be seen on plants that have overlapping triads and thus parallelogram planforms.

4.1. The parameters

The parameters introduced in Section 3 describe the material properties of the tunica and the corpus foundation, the stresses in the tunica, and the geometry of the prebuckling, stressed tunica shell. More experimental work is needed to find the values of these parameters for plants; here we review the information that is available.

A number of the non-dimensionalized parameters derived in Section 3.2 are expressed in terms of the *natural wavelength* $2\pi\Lambda$ of the shell, where

$$\Lambda^4 = \frac{Eh^3v^2}{\kappa + \frac{Eh}{R_\alpha^2}}. \tag{70}$$

In this expression, E is the Young's modulus and h the thickness of the tunica shell, and $v^2 = \frac{1}{12(1-\mu^2)}$, where μ is the Poisson's ratio of the shell. The parameter κ is a linear spring constant measuring the strength of the corpus foundation. Dumais and Steele (2000) gathered the following experimentally determined values for these material parameters from the literature:

- *Young's modulus E*: Cellulose (the main component of cell walls) has a Young's modulus of 100 GPa. Wainwright et al. (1976) give a value of 1 GPa for *Nitella* cell walls. For their numerical calculations of stress distributions, Dumais and Steele adopt a value of 1 GPa, which equals 10^{-3} N/μm^2. For comparison, the Young's modulus values (in GPa) for various other materials are as follows:

Soft Cuticle of a Locust:	0.21
Rubber:	6.9
Shell Membrane of an Egg:	7.58
Human Cartilage:	24.13
Human Tendron:	551.6
Wood (along the Grain):	6895
Iron and Steel:	206,850

- *Poisson's ratio μ*: Hejnowicz and Sievers (1996) measured values of Poisson's ratio ranging from 0.15 to 0.5 in the sunflower capitulum. Dumais and Steele adopt values ranging from 0.3–0.5. A range of $\mu = 0.3$–0.5 gives a range of $v = 0.3$–0.333.
- *The tunica thickness h*: Steele (2000) cites data collected from the literature by C. Schmid and J. Dumais that give tunica thicknesses ranging from a few micrometer to close to 60 μm. For calculations, we take the value of h to be 10 μm.
- There is no experimentally determined value for κ.

A summary of the non-dimensional parameters in the FvKD equations that we analysed is as follows:
- Corpus foundation parameters:

$$\kappa' = \frac{\Lambda^4\kappa}{Eh^3v^2},$$

$$\gamma' = \frac{\Lambda^4\gamma}{Ehv^2}.$$

Positive values of these parameters mean that the corpus foundation provides a damping for unstable modes. In what follows, we will take these parameters to be positive, but we do not have good estimates for their exact values. In analysing the averaged energy, however, these parameters will get further absorbed into another ratio that determines the strength of the nonlinear interaction between active modes. In deriving Eq. (68), we have taken γ to be dominated by the hard spring response of the corpus foundation and large enough so that $\gamma(P - P_c)$ is of order unity, thereby ensuring a balance between all three terms in the energy.

- Stress parameters:

$$P = -\frac{N_\alpha \Lambda^2}{E h^3 v^2},$$

$$\chi = \frac{N_r}{N_\alpha}.$$

The analysis of Section 3 assumes that the stress parameter P is only slightly above the critical value at which unstable modes appear. There is no experimentally obtained value of this parameter, but it is reasonable to assume that plant patterns are initially produced once the stress becomes supercritical and that the resulting deformation relieves the system of excess mechanical stress. The results of Dumais and Steele (2000) indicate that it is in the circumferential, i.e., α, direction that stress is negative—that is, $P > 0$-and that N_r is either positive or negative with a magnitude less than that of N_α. Therefore, we take $\chi < 1$.

- Geometric parameters:

$$C = \frac{\Lambda^2}{R_\alpha h v},$$

$$\rho = \frac{R_\alpha}{R_r}.$$

These two parameters describe the intrinsic curvature of the plant apex in the region of pattern formation, as depicted in Fig. 14. The choice $\rho > 0$ describes an elliptic region, with $\rho = 1$, $C > 0$ describing the spherical apex of Fig. 14(a) and $\rho = 1$, $C < 0$ describing the inverted sphere of Fig. 14(b). The choices $C > 0$, $\rho < 0$ describe the hyperbolic geometry of Fig. 14(c).

$$\Gamma = \frac{R}{\Lambda}.$$

This parameter, expressing the ratio of the radius of the region of pattern formation to the natural wavelength, grows larger as the plant apex grows in size (so that R increases) while the material properties of the plant remain constant (so that Λ remains constant). We remind the reader, however, that R, and therefore Γ may decrease in size during a pattern-forming process, such as in the formation of a sunflower.

There is a constraint $C^2 + \kappa' = 1$. We thus have seven parameters (γ, P, χ, C, ρ, Γ, and v) that remain in the FvKD equations. We will show below how the analysis of the averaged elastic energy (65) allows for a further reduction in the number of parameters. In particular, for the case $\rho = 1$, we will be left with four parameters.

To express the area of a newly formed primordium in terms of these parameters, recall that we approximated this area by the parallelogram determined by the vectors $\omega_1' = \frac{1}{g}(\lambda m, 2\pi R(md - q))$, $\omega_2' = \frac{1}{g}(\lambda n, 2\pi R(nd - p))$, and note that we have now scaled the radial coordinate by Λ. The area is thus approximated by the parallelogram determined by the vectors $\omega_1'' = \frac{1}{g}(\lambda \Lambda m, 2\pi R(md -$

q)), $\omega_2'' = \frac{1}{g}(\lambda \Lambda n, 2\pi R(nd - p))$; that is, it is the absolute value of the determinant of the matrix

$$\Omega'' = \frac{1}{g} \begin{pmatrix} \lambda \Lambda m & \lambda \Lambda n \\ 2\pi R(md - q) & 2\pi R(nd - p) \end{pmatrix}, \tag{71}$$

the area is $A = |\det \Omega''| = \frac{2\pi}{g} R \Lambda \lambda = \frac{2\pi}{g} \Gamma \Lambda^2 \lambda$. (As described in Section 1.5, after their formation, primordia leave the region of pattern formation and mature into phylla as the plant shoot continues to grow. The size of the primordium/phyllo will then increase either exponentially if the radial plant growth is exponential, or at a constant rate if the radial plant growth is constant. The formula $A = 2\pi \frac{\lambda}{\gamma} \Gamma \Lambda^2$ describes primordium size, not the size of developed phylla.)

Our next goal is to determine how the coefficients σ and τ of the averaged elastic energy (68) depend on the above parameters. In the following, we again drop the primes on the non-dimensionalized parameters κ' and γ'.

4.2. The linear growth rates and the set of active modes

In this section, we examine how the linear growth rates $\sigma(l, m)$ depend on the parameters and determine the set $\mathfrak{A}$ of active modes. Recall that, in terms of the non-dimensionalized parameters, the linear growth of a mode with wavevector $\vec{k} = (l, m)$ is

$$\sigma(l, m) = \hat{\Delta}^2 + P \hat{\Delta}_\chi - \kappa - C^2 \frac{\hat{\Delta}_\rho^2}{\hat{\Delta}^2}, \tag{72}$$

where $\hat{\Delta} = l^2 + \frac{1}{\Gamma^2} m^2$, $\hat{\Delta}_\chi = \chi l^2 + \frac{1}{\Gamma^2} m^2$, and $\hat{\Delta}_\rho = l^2 + \frac{\rho}{\Gamma^2} m^2$. The analysis of Section 3 assumed that the stress parameter P is slightly above a critical value P_c, which is the minimum value of P for which there are modes with nonnegative linear growth rates. For $P > P_c$, there is a set of modes with positive linear growth rates. However, the nonlinear generation of weakly damped modes means that some of them must also be included in the active set. We define the active set $\mathfrak{A}$ to be the set of all modes $\vec{k} = (l, m)$ such that $\sigma(l, m) > -3\sigma(l_c, m_c)$, where $\vec{k}_c = (l_c, m_c)$ is the (a) wavevector of the mode(s) with the largest positive linear growth rate. The choice of 3 is not important to the outcome; the factor must be large enough to include all relevant modes.

We begin by studying the case $\rho = 1$ (describing the sphere or the inverted sphere). For this case, the growth relation simplifies, upon using the constraint $C^2 + \kappa = 1$, to

$$\sigma(l, m) = -\hat{\Delta}^2 + P \hat{\Delta}_\chi - 1, \tag{73}$$

which only depends on P, χ and Γ. For $\chi = 1$, the modes with the largest linear growth rates are those on the ellipse $l^2 + \frac{1}{\Gamma^2} m^2 = 1$ marked in Fig. 18(a and b). The growth rate of modes on this ellipse is given by $\sigma(l, m) = P - 2$. For $P > P_c = 2$ there is an annulus of modes with
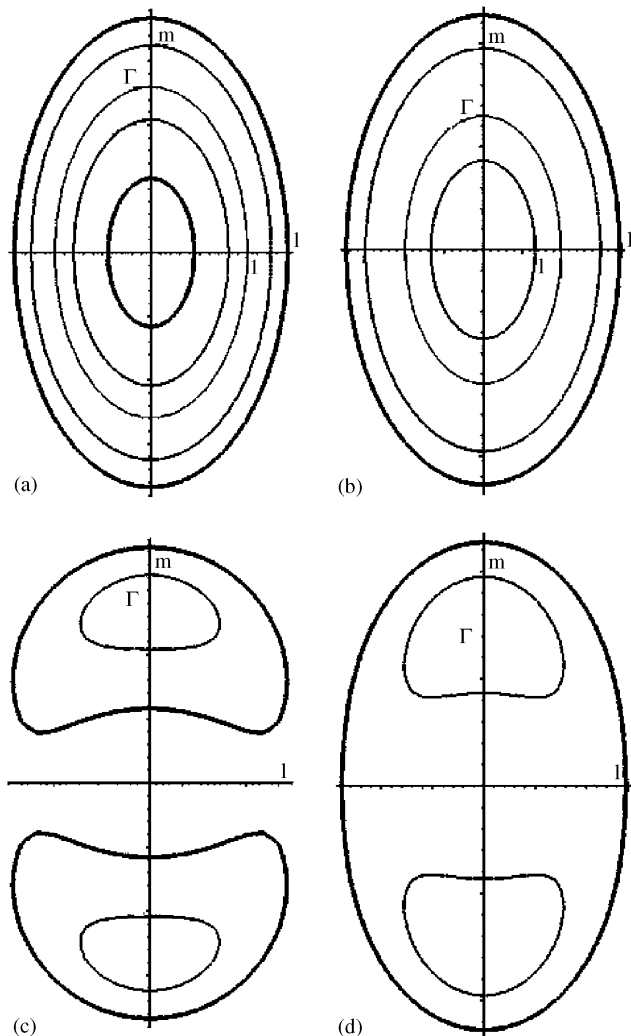
Fig. 18. The positive and active modes for the elliptic shell with $\rho = 1$ and $0 < \chi$. For (a,b) $\chi = 1$ and (c,d) $\chi = \frac{1}{2}$, and (a,c) $P = 2.2$ and (b,d) $P = 2.7$, the sets of modes with positive growth rates (bounded by thin lines) and the sets of active modes (bounded by thick lines) are shown. For $\chi = 1$, the modes with the largest growth rates are those that are on the middle ellipse that runs through the points $(0, \Gamma)$ and $(1, 0)$.

positive growth (Fig. 18(a and b)), and any mode (l, m) with $\sigma(l, m) > -3(P - 2)$ is included in the active set (Fig. 18(c and d)). For $\chi < 1$, the only neutral mode at $P = P_c$ is $\vec{k}_c = (0, \Gamma)$, and for $P > P_c$ the sets of positive-growth and active modes are parts of annuli concentrated about $\vec{k}_c$; see Fig. 18 for $\chi > 0$; details of $\chi < 0$ are given in (Shipman, 2004). In summary, then, the parameter Γ determines the center ellipse $l^2 + \frac{1}{\Gamma^2} m^2 = 1$, and the stress parameter P determines the width of the annulus of active modes (in the case $\chi = 1$) or part of an annular of active modes (in the case $\chi < 1$). Note that, for a fixed value of m and any $\chi \leqslant 1$, the maximum growth occurs for l such that (l, m) is on the middle ellipse.

For the hyperbolic shell described by $\rho < 0$, a mode with wavevector $\vec{k} = (l, m)$ is a neutral mode for

$$P = \frac{1}{\chi l^2 + \frac{1}{\Gamma^2} m^2}$$
$$\times \left(\left(l^2 + \frac{1}{\Gamma^2} m^2 \right)^2 + \kappa + C^2 \left(\frac{l^2 + \frac{\rho}{\Gamma^2} m^2}{l^2 + \frac{1}{\Gamma^2} m^2} \right)^2 \right). \quad (74)$$

For the case $\chi = 1$ of isotropic stress, P is minimized on the intersection of the loci $l^2 + \frac{\rho}{\Gamma^2} m^2 = 0$, $l^2 + \frac{1}{\Gamma^2} m^2 = \sqrt{\kappa}$; that is, $P_c = 2\sqrt{\kappa}$ and $\vec{k}_c = (\kappa)^{\frac{1}{4}} (\pm \frac{1}{\sqrt{2}}, \frac{\Gamma}{\sqrt{-2\rho}})$. For $0 < \chi < 1$, the results are qualitatively similar. The critical stress value $P_c = 2\sqrt{\kappa} < 2$ for a hyperbolic shell is thus less than that for an elliptic shell. The regions of wavevectors of modes with positive linear growth rates and of active modes for the hyperbolic shell described by $\chi > 0$, $\rho = -1$ and $\kappa = \frac{1}{2}, C = \sqrt{1 - \kappa^2}$ are shown in Fig. 19.

For $\rho = -1$, $\chi > 0$, the hyperbolic shell differs from the elliptic shell in that the critical wavevector has a non-zero radial component. However, for $\chi \simeq \rho < 0$, the critical wavevector for the hyperbolic shell is $\vec{k}_c = (0, \Gamma \sqrt{\kappa + C^2 \rho})$. Thus, for $\chi < 0$, the regions of positive and active modes for the hyperbolic shell are qualitatively similar to the regions for the elliptic shell (Shipman, 2004).

4.3. The coefficient $\tau(\vec{k}_r, \vec{k}_s, \vec{k}_{r+s} = \vec{k}_r + \vec{k}_s)$

The cubic coefficient

$$\tau(\vec{k}_r, \vec{k}_s, \vec{k}_{r+s} = \vec{k}_r + \vec{k}_s) = \tau(r, s, r + s)$$
$$= -\frac{C}{\nu \Gamma^2} (l_r m_s - l_s m_r)^2$$
$$\times \sum_{j=r,s,r+s} \frac{l_j^2 + \frac{\rho}{\Gamma^2} m_j^2}{(l_j^2 + \frac{1}{\Gamma^2} m_j^2)^2} \quad (75)$$

of the averaged energy has the following properties:

1. As $l_r m_s - l_s m_r = l_r m_{r+s} - l_{r+s} m_r = l_s m_{r+s} - l_{r+s} m_s$, $\tau(\vec{k}_r, \vec{k}_s, \vec{k}_{r+s})$ is a symmetric function of the wave-vectors.
2. What values of the radial wavenumbers maximize τ? For a fixed value of m_j, the fraction

$$\frac{l_j^2 + \frac{\rho}{\Gamma^2} m_j^2}{(l_j^2 + \frac{1}{\Gamma^2} m_j^2)^2}$$

is maximized for $l_j = 0$. If, however, two radial coordinates are equal to zero, then τ also equals 0 due to the factor $(l_r m_s - l_s m_r)^2$. *For fixed angular wavenumbers, the coefficient τ achieves local maxima at where exactly one of the radial coordinates is zero.* Writing the wavevectors in terms of the
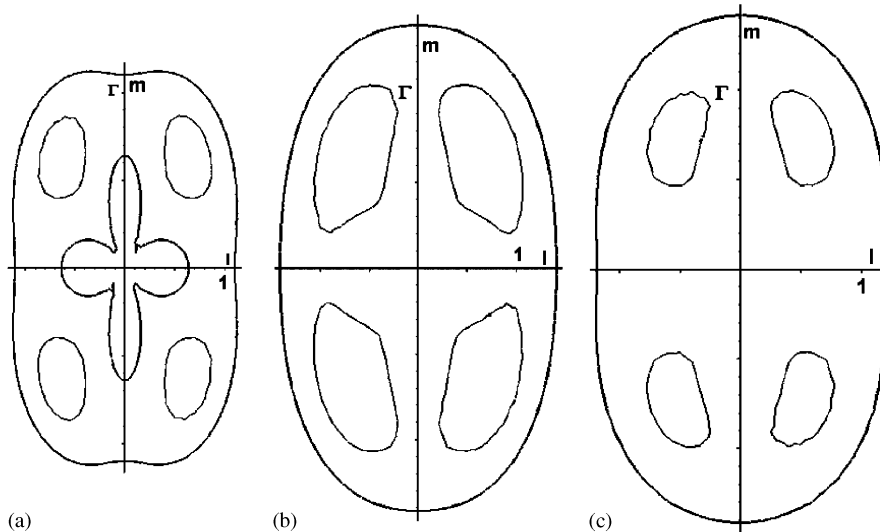
Fig. 19. The positive and active modes for the hyperbolic shell; $\rho = -1$, $\kappa = \frac{1}{2}$, $C = \sqrt{1 - \kappa^2}$. For $\chi = 1$, and (a) $P = 2.3\sqrt{\kappa}$, (b) $P = 2.7\sqrt{\kappa}$, the modes with positive growth rates are bounded by the thin lines, and the active modes by the thick lines. (c) For $\chi = \frac{2}{3}$, and $P = 2.7\sqrt{\kappa}$, the modes with positive growth rates are bounded by the thin lines, and the active modes by the thick lines.
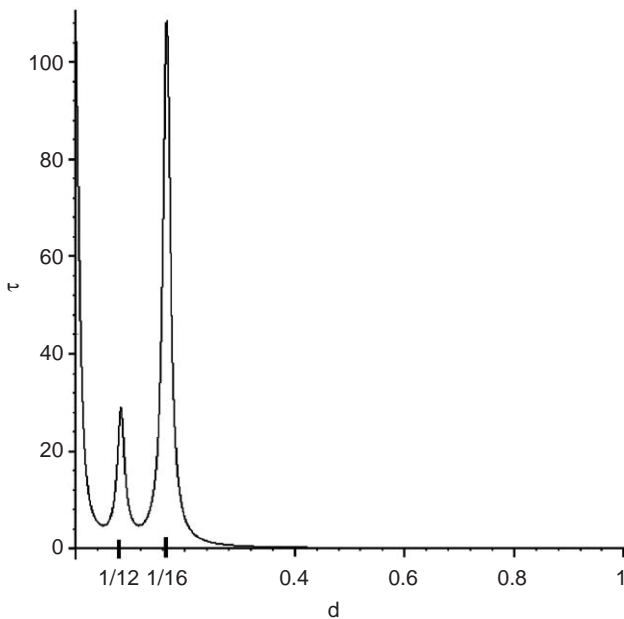

Fig. 20. The coefficient τ as a function of d for the inverted sphere. τ is evaluated at $\vec{k}_m = (\frac{2\pi}{\lambda}(q - md), m)$, $\vec{k}_n = (\frac{2\pi}{\lambda}(p - nd), n)$, $\vec{k}_{m+n} = \vec{k}_m + \vec{k}_n$ for $m = 6$, $n = 6$, $\lambda = \frac{3}{5}$, $\Gamma = 12$, $\rho = 1$, and $\frac{C}{v} = -1$.

phyllotactic coordinates as $\vec{k}_m = (\frac{2\pi}{\lambda}(q - md), m)$, $\vec{k}_n = (\frac{2\pi}{\lambda}(p - nd), n)$, $\vec{k}_{m+n} = (\frac{2\pi}{\lambda}(p + q - (m + n)d))$, this means that $\tau(m, n, m + n)$, as a function of d, achieves local maxima at the three values $d = \frac{p}{n}, \frac{q}{m}, \frac{p+q}{m+n}$ that make one of the radial coordinates equal to zero. In fact, τ is a very sensitive function of d, with a Dirac delta-function-like

nature, with extrema at the values of d that make one of the radial wavenumbers equal to zero, as illustrated in the graphs of τ for $\rho = 1$ (Fig. 20). This last expression is maximized at $|\tau| = \infty$ for $\lambda = 0$ or $d = \frac{q}{m}, \frac{p}{n}, \frac{p+q}{m+n}$. The coefficient τ is larger for smaller λ, or, equivalently, for larger values of the radial wavenumber.

We can also write $\tau(m, n, m + n)$ as a function of the phyllotactic coordinates d, λ, m, n and Γ as follows: for $\rho = 1$,

$$\tau = -\frac{C}{v}(2\pi)^2 \left[\frac{1}{2\pi(\Gamma\frac{q-md}{g})^2 + m^2\frac{\lambda^2}{g^2}} + \frac{1}{2\pi(\Gamma\frac{p-nd}{g})^2 + n^2\frac{\lambda^2}{g^2}} + \frac{1}{2\pi(\Gamma\frac{p+q-(m+n)d}{g})^2 + (m+n)^2\frac{\lambda^2}{g^2}} \right].$$

This last expression is maximized at $|\tau| = \infty$ for $\lambda = 0$ and $d = \frac{p+q}{m+n}$ or $\frac{p}{m}$ or $\frac{q}{n}$. The coefficient τ is larger for smaller λ–that is, for larger l_1, l_2.

3. What values of the angular wavenumbers maximize τ? Writing $\vec{k}_1 = (l_1, m_3 - m)$, $\vec{k}_2 = (l_2, m)$, $\vec{k}_3 = (l_1 + l_2, m_3)$, for $\rho = \pm 1$, fixed m_3 and arbitrary values of C and Γ, τ is maximized at $m = \frac{|l_2|m_3}{|l_1| + |l_2|}$. In particular, we will be interested in the case $l_1 = -l_2$, $\vec{k}_3 = (0, m_3 = \Gamma)$, for which τ is maximized at $\vec{k}_1 = (l, \frac{m_3}{2})$, $\vec{k}_2 = (-l, \frac{m_3}{2})$.

4. τ is proportional to the curvature constant C; when $C = 0$ the quadratic coefficient in the amplitude equations vanishes. This means that rolls are the only stable solutions of the amplitude equations when $C = 0$. Note that the appearance of C in the amplitude equations comes from there being non-zero curvature in the original, unbuckled shell.

4.4. Three-mode minimizers

We first analyse the simplest case, namely that when the active set $\mathfrak{A}$ contains just three modes

$$\vec{k}_m = \left(\frac{2\pi}{\lambda}\,(q - md), m\right), \quad \vec{k}_n = \left(\frac{2\pi}{\lambda}\,(p - nd), n\right),$$

$$\vec{k}_{m+n} = \vec{k}_m + \vec{k}_n.$$

Writing $\tau(m, n; m + n) = \tau$, the amplitude equations are

$$\frac{\partial A_m}{\partial t} = \sigma(\vec{k}_m)A_1 + \tau A_n^* A_{m+n} - 3\gamma A_m(A_m A_m^* + 2A_n A_n^*$$
$$+ 2A_{m+n}A_{m+n}^*),$$

$$\frac{\partial A_n}{\partial t} = \sigma(\vec{k}_n)A_2 + \tau A_m^* A_{m+n} - 3\gamma A_n(A_n A_n^* + 2A_m A_m^*$$
$$+ 2A_{m+n}A_{m+n}^*),$$

$$\frac{\partial A_{m+n}}{\partial t} = \sigma(\vec{k}_{m+n})A_{m+n} + \tau A_m A_n - 3\gamma A_{m+n}(A_{m+n}A_{m+n}^*$$
$$+ 2A_m A_m^* + 2A_n A_n^*). \qquad (76)$$

The critical points of $\mathfrak{E}(A_m, A_n, A_{m+n})$ are given by the stationary solutions of Eq. (76). The important results are

1. For $\chi < 1$ (as is experimentally determined for plants), the purely circumferential mode $\vec{k}_c = (0, \Gamma)$ maximizes $\sigma(l, m)$. For convenience of presentation, we will consider values of the size parameter Γ which are either even $2N$ or odd $2N + 1$ integers. Therefore, the most amplified mode is $\vec{k}_{m+n} = (0, m + n)$, which, in the absence of $\vec{k}_m$ and $\vec{k}_n$ would grow to an amplitude $A_{m+n} = \sqrt{\frac{\sigma_{m+n}}{3\gamma}}$ for $m + n = \Gamma = 2N$ or $2N + 1$.
2. However, near onset the ridge solution $A_{m+n} = \sqrt{\frac{\sigma_{m+n}}{3\gamma}}$, $A_m = A_n = 0$, can be linearly unstable to a triad of modes, namely an approximately hexagonal planform. The stability of ridge or hexagonal planforms is determined by the parameters $\xi_j = \frac{3\sigma(k_j)\gamma}{\tau^2}$ (see Section 3); for small values of ξ_j (i.e., for large values of the interaction coefficient τ), hexagons are the preferred planform.
3. For $\Gamma = 2N$, the triad which minimizes $\mathfrak{E}$ is $\vec{k}_m = (-l(\lambda), m = N)$, $\vec{k}_n = (l(\lambda), n = N)$, $\vec{k}_{m+n} = \vec{k}_c = (0, m + n = \Gamma = 2N)$, where $l(\lambda)$ is of order 1, and the amplitudes of the minimizer are such that $A_{m+n} > |A_m| = |A_n|$. The reasons for this follow from the properties of τ stated in Section 4.3. From $\vec{k}_3 = (\frac{2\pi}{\lambda}(p + q - (m + n)d), m + n) = (0, 2N)$ one sees that $d = \frac{p+q}{m+n}$; this is an optimal choice of d (Property 2). Also, the choice $m = n = N$ is optimal according to Property 3. In Fig. 21, we plot the ratio $\frac{|A_1|}{|A_3|}$ and the radial wavenumber $l(\lambda)$ as functions of χ. Note that $l(\lambda) \simeq 1$ is chosen as a compromise between the choices of l that maximize σ and τ. For small χ, σ is maximized at $l = 0$ ($\lambda = \infty$). It is therefore essential that τ depend on l, and (Property 2), τ is, in fact,

maximized at $l = \infty$ ($\lambda = 0$). Smaller values of χ yield smaller choice of l and also, due to smaller values of $\sigma(\vec{k}_1)$, $\sigma(\vec{k}_2)$ and τ, smaller values of the ratio $\frac{|A_1|}{|A_3|}$.

Thus, the purely circumferential deformation $\cos(\vec{k}_3 \cdot \vec{x})$ (corresponding to radial ridges) is more dominant for smaller χ. We also note that the chosen wavevectors $(\pm l(\lambda), N)$ lie well within the active range $\sigma(l, m) > -3\sigma_c$ so that the choice of the number 3 in defining the active region plays little role. We could have chosen the factor to have been 4 or 5 and obtained the same results. Recalling Property 4, the linear dependence of τ on C, we plot in Fig. 22 the graph of $\frac{|A_1|}{|A_3|}$ against $Q = \frac{C}{\sqrt{3\gamma\nu}}$. Note that, for $Q < 1$, the purely circumferential ridge solution is stable, but, as Q grows, the ratio approaches unity; the planform becomes approximately hexagonal.

(a)

(b)
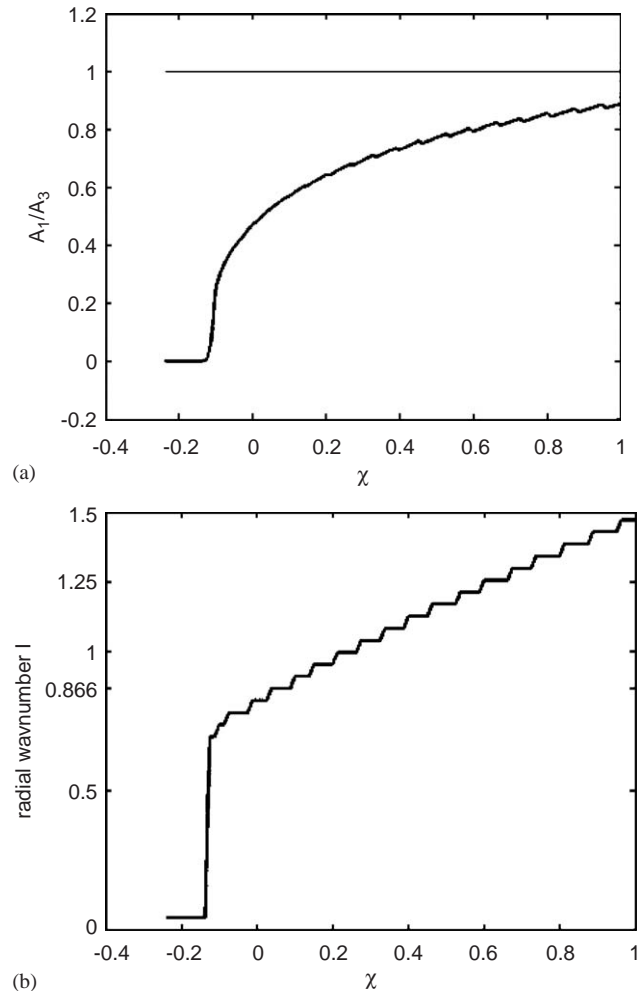
Fig. 21. For the parameters $\frac{C}{\nu} = 3$, $\gamma = 1$, $P = 2.3$ and angular wavenumbers 3,3,6, $\Gamma = 6$, the energy-minimizing choices of the amplitudes and the radial wavenumber l were found. (a) Plotted is the ratio $\frac{A_1}{A_3} = \frac{A_2}{A_3}$ as a function of $\chi = -\frac{1}{4}..1$. (b) The energy-minimizing choice of the radial wavenumber as a function of $\chi = -\frac{1}{4}..1$. For small χ, the choice is very close to $\frac{\sqrt{3}}{2} \simeq 0.866$.
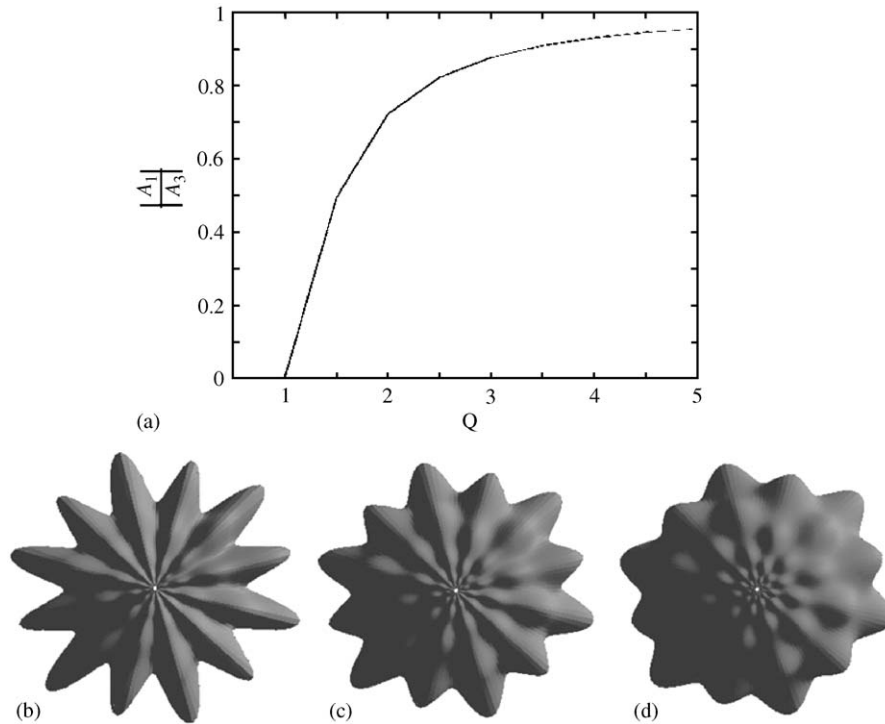
Fig. 22. (a) Parameters: $Q = 1..5$, $\chi = \frac{2}{3}$, $P = 2.4$ modes 6,6,12, $\Gamma = 12$. Plotted is the ratio $\frac{|A_1|}{|A_3|}$, which, as $\sigma(\vec{k}_1) = \sigma(\vec{k}_2)$, equals the ratio $\frac{|A_2|}{|A_3|}$. (b–d) For the values (b) $Q = 1.25$ and (c) $Q = 1.5$ the configurations determined by the experiment of (a) are plotted as deformations of a sphere. As Q gets large, the optimal configuration approaches that in which all three amplitudes are equal (d).

4. For $\Gamma = 2N + 1$, the energy-minimizing triad is $\vec{k}_m = (-l(\lambda), N)$, $\vec{k}_n = (l(\lambda), N + 1)$, $\vec{k}_{m+n} = (0, 2N + 1)$, and results similar to those plotted in Fig. 21 are obtained.

Our conclusions are that, depending on the curvature C and the ratio of radial to circumferential applied stress χ, an approximately hexagonal planform is preferred. For increasing Γ, we list in Table 1 the possibilities.

To use these results to produce a picture of a plant surface, we assume that the pattern formed in the generative region remains the same as the buckled tunica hardens and moves away from the shoot tip. (This is more accurate of an assumption for some plants (e.g. cacti) than it is for others (e.g. leafy plants); see Section 5.) Then, the graph of the function $w = |A_1| \cos(l_1 s + m_1\alpha) + |A_2| \cos(l_2 s + m_2\alpha) + |A_3| \cos(l_3 s + m_3\alpha)$, $0 < s < r_m$ if $s = r$ or $s = \ln(r)$, depending on whether the radial growth of the plant is constant or exponential, gives the deformation of the plant surface after the plant tip has grown a length r_m (if $s = r$) or e^{r_m} (if $s = \ln(r)$). Note that if $s = r$, the plant exhibits the plastochrone difference, and if $s = \ln(r)$, the plant exhibits the plastochrone ratio. Examples of a theoretical energy-minimizing configurations for the inverted sphere $C < 0$, together with a real cactus that they reproduces, are shown in Fig. 23. The inverted-sphere geometry is only

Table 1
Energy-minimizing parastichy numbers for small values of Γ

Γ	m	n	$m + n$	Type of pattern
2	1	1	2	Alternating 1-whorl
3	1	2	3	Fibonacci spirals
4	2	2	4	Alternating 2-whorl
5	2	3	5	Fibonacci spirals
6	3	3	6	Alternating 3-whorl
7	3	4	7	Lucas spirals
8	4	4	8	Alternating 4-whorl
9	4	5	9	
10	5	5	10	Alternating 5-whorl
11	5	6	11	
12	6	6	12	Alternating 6-whorl

relevant at the region of pattern formation; as the pattern moves out, this geometry gives way to a flatter or non-inverted sphere geometry. The reproduction in Fig. 23(d) is plotted as a deformation of a flat surface, whereas the reproduction of Fig. 23(b) is plotted as a deformation of a sphere. Similarly, in Fig. 22(b–d) we show the deformations of a sphere determined by increasing values of Q in the experiment of Fig. 22(a).

We next address the question of transitions between these configurations as the size of Γ increases. As Γ increases from $2N$ to $2N + 1$ and on up, the
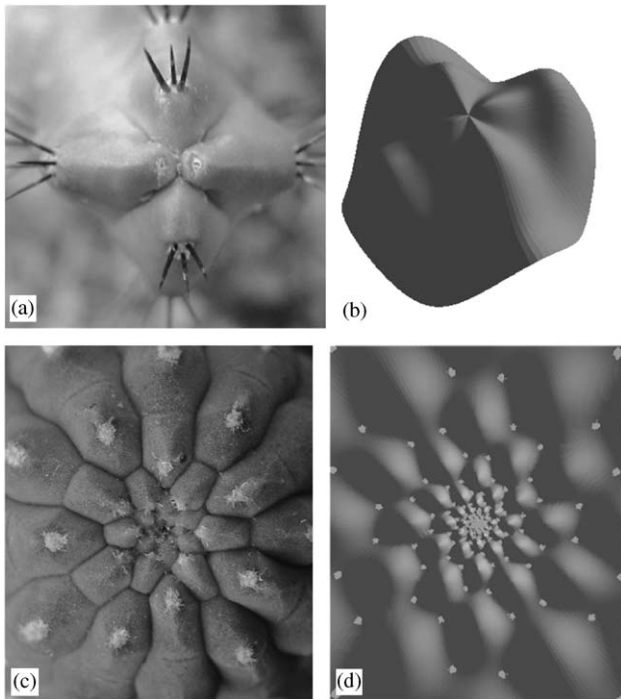
Fig. 23. (a) A cactus with alternating 2-whorl phyllotaxis and ridges and (b) a theoretical reproduction, the plot of $a_2 \cos \vec{k}_2 \cdot \vec{x} + a_2 \cos \vec{k}_2 \cdot \vec{x} + a_4 \cos \vec{k}_4 \cdot \vec{x}$ for $a_4 \gg a_2$. (c) A cactus with alternating 6-whorl phyllotaxis and (d) a theoretical reproduction, the plot of $a_6 \cos \vec{k}_6 \cdot \vec{x} + a_6 \cos \vec{k}_6 \cdot \vec{x} + a_{12} \cos \vec{k}_{12} \cdot \vec{x}$ for $a_{12} = a_6$.

Fig. 24. (a) The phyllotaxis on a plant that undergoes a (I,1) transition from a (2,2,4) alternating 2-whorl phyllotaxis (large values of s) to (2,3,5)-spiral phyllotaxis (small s) is shown along with the spiral families, one of which does not change during the transition. A penta–hepta pair is formed where the two dislocations in the other spiral families meet. The corresponding wavevectors are illustrated in (b) and (c) along with the typical boundary of the set of active modes.

energy-minimizing triad changes in the sequence

$$
\begin{array}{lll}
\vec{k}_N = (l, N) & \vec{k}_N = (l, N) & \vec{k}_{N+1} = (l, N+1) \\
\vec{k}'_N = (-l, N) \quad \rightarrow & \vec{k}_{N+1} = (-l, N+1) \quad \rightarrow & \vec{k}_{N+1} = (-l, N+1) \quad \rightarrow \cdots. \quad (77) \\
\vec{k}_{2N} = (0, 2N) & \vec{k}_{2N+1}(0, 2N+1) & \vec{k}_{2N+1} = (0, 2(N+1))
\end{array}
$$

As Γ increases from $2N$ to $2N+1$ and then from $2N+1$ to $2N+2$, there is an abrupt change in the optimal triad, but the triad always has the form $\vec{k}_m = (l, m), \vec{k}_n = (-l, n), \vec{k}_{m+n} = (0, m+n = \Gamma)$, where we find that l does not depend on Γ (l is of order 1 and does depend on χ as discussed above). Writing the wavevectors in the standard form $\vec{k}_m = (l_m = \frac{2\pi}{\lambda}(q - md), m), \vec{k}_n = (l_n = \frac{2\pi}{\lambda}(p - nd), n), \vec{k}_{m+n} = (\frac{2\pi}{\lambda}(p + q - (m+n)d), m + n)$, we see that $\vec{k}_{m+n} = (0, \Gamma)$ implies that $d = \frac{p+q}{m+n} = \frac{p+q}{\Gamma}$, and therefore $l = l_m = -l_n = \pm 2\pi \frac{q}{\lambda} \frac{1}{\Gamma}$. As l is constant with respect to Γ, the ratio $\frac{q}{\lambda}$ changes like Γ. As a consequence, the area $A = 2\pi \frac{\lambda}{q} \Gamma \lambda^2 = \frac{(2\pi\lambda)^2}{l}$ of a primordium is constant with respect to Γ.

These are transitions of type (I,1). As noted in the introduction, these transitions are observed in nature, particularly on plants (e.g. saguaro cacti) for which the configuration is dominated by ridges (i.e. on plants for which $\frac{|A_1|}{|A_3|}$ is small), although they can also be observed

on plants with hexagonal configurations, as in Fig. 10. Also note that one wavevector is preserved in each transition of the sequence (77). If one draws the curves joining the maxima of the surface deformation in adjoining regions with different patterns, one sees dislocations in two families of spirals, corresponding to the two wavevectors that changed, and a penta–hepta defect at the point where the two dislocations meet. In Fig. 24, we illustrate this in the (s, α)-plane, with the transition between the phyllotactic lattices of the alternating 2-whorl (2,2,4) and (2,3,5)-spiral patterns. A penta–hepta defect and the preservation of one family of spirals are illustrated in the plant of Fig. 10.

Although the (I,1) transition from the alternating 2-whorl (2,2,4) to the Fibonacci (2,3,5) spiral is commonly observed in nature, on a typical plant one observes (II,2) transitions $(2, 3, 5) \rightarrow (3, 5, 8) \rightarrow \cdots$ thereafter. The challenge is to find, within our picture, an explanation

for these (II,2) transitions. A hint of the answer lies within the planforms which are usually observed at the higher Fibonacci numbers. They tend to look more like parallelograms than like hexagons, as if they have been constructed by deformations which contain more than three wavevectors. And, of course, there is absolutely no a priori reason why the active set $\mathfrak{A}$ should be simply restricted to single triads.

4.5. Four- and five-mode energy minimizers

There are two reasons for us to consider more than one interacting triad in the active set.

Reason 1: First, let us imagine that we have included a countably infinite set of modes $\vec{k}_j$ in the active set, each of which is a member of a triad defined by $\vec{k}_r + \vec{k}_s = \vec{k}_{r+s}$. We note that the corresponding set of amplitude equations cannot be consistently reduced to that of a single triad $\vec{k}_m, \vec{k}_n, \vec{k}_{m+n} = \vec{k}_m + \vec{k}_n$ by setting all other amplitudes to zero. The reason is that any of the modes $\vec{k}_m \pm \vec{k}_{m+n}$, $\vec{k}_n \pm \vec{k}_{m+n}$ (recall that the value of τ for a second harmonic $\vec{k}_m + \vec{k}_m$ or zero harmonic $\vec{k}_m - \vec{k}_m$ is zero) can be driven by quadratic interactions. For very small stress P, the growth rate of these modes are so negative that their amplitudes are, while not exactly zero, very close to zero. However, for larger P, these modes are more likely to be members of the active set. To illustrate this, look at Fig. 25, which delineates in the (Γ, d)-plane for $P = 2.5, \chi = \frac{2}{3}$, and $\rho = 1$ which modes are active according to our $\sigma(l, m) > -3\sigma_c$ criterion. Notice that for $\Gamma \simeq 5$, there is a region in the plane for

Fig. 25. (a) The regions in the (Γ, d)-plane in which $\vec{k}_n$, for $n = 2, 3, 5, 8$, are active modes, given $\rho = 1$, $\chi = \frac{2}{3}$, $P = 2.5$.

which not only the modes $\vec{k}_2, \vec{k}_3$ and $\vec{k}_5$ are active, but also the mode $\vec{k}_8 = \vec{k}_3 + \vec{k}_5$. The mode $\vec{k}_7 = \vec{k}_2 + \vec{k}_5$ may also be a member of the active set. Which mode, $\vec{k}_7$ or $\vec{k}_8$, is more likely to play a role in the energy-minimizing configuration?

To answer this question, first recall that we have found that the most unstable triad is of the form $\vec{k}_m = (l, m), \vec{k}_n = (-l, n), \vec{k}_{m+n} = (0, m + n)$, where $m \simeq n$. For sufficiently large values of P, the wavevectors $\vec{k}_{2m+n} = \vec{k}_m + \vec{k}_{m+n}$ or $\vec{k}_{m+2n} = \vec{k}_n + \vec{k}_{m+n}$ may come into play. For $m = n$, $2m + n = m + 2n$, but if $n = m + 1$, the wavevectors $\vec{k}_{2m+n}$ and $\vec{k}_{m+2n}$ may not play symmetric roles; which mode is more likely to have a non-zero amplitude in an energy-minimizing configuration? The simplest way to check is to minimize the energy (68) restricted to the four modes with wavevectors $\vec{k}_m = (\frac{2\pi}{\lambda}, (q - md), m), \vec{k}_n = (\frac{2\pi}{\lambda}(p - nd), n), \vec{k}_{m+n} = \vec{k}_m + \vec{k}_n$ and either $\vec{k}_{2m+n} = \vec{k}_m + \vec{k}_{m+n}$ or $\vec{k}_{m+2n} = \vec{k}_n + \vec{k}_{m+n}$. The energy thus becomes a function of d and λ and our task is to find the energy-minimizing choices these parameters and the mode amplitudes for each choice of a fourth wavevector. Using our experience from the simple case of a single triad and the energy-minimizing choices $m \simeq n \simeq \frac{\Gamma}{2}$, consider the triads $\vec{k}_m, \vec{k}_{m+n}, \vec{k}_{2m+n}$ and $\vec{k}_n, \vec{k}_{m+n}, \vec{k}_{m+2n}$. The ratios $\frac{n,m+n}{m+2n}$ are closer to $\frac{1}{2}$ than are the ratios $\frac{m,m+n}{2m+n}$. For the choices $m = 2, n = 3$, for example, the ratios $\frac{2}{7}$ and $\frac{5}{7}$ are farther from $\frac{1}{2}$ than are the ratios $\frac{3}{8}$ and $\frac{5}{8}$. Although we do not have an analytic proof that this leads to a lower energy configuration with the wavevector choice $\vec{k}_{m+2n}$, it is confirmed by numerical experiments that this mode is energetically preferred. Consequently, the quadratic interaction which gives the strongest bias is the one in which one adds the second two modes of the existing triad. This, of course, is exactly the recipe for producing Fibonacci sequences. The particular member of the Fibonacci family which is chosen (regular Fibonacci $1, 1, 2, 3, 5, 8, 13, \ldots$, double Fibonacci $2, 2, 4, 6, 10, 16, 26, \ldots$, or Lucas $3, 4, 7, 11, 18, \ldots$) for a particular plant is determined by its choice of starting triad.

Reason 2: Bias plays a major role in choosing between various bifurcation options. This idea is not new, but was suggested over 50 years ago by Koiter (1963), who introduced the term *geometric imperfection* to describe the effect. The idea is simple. Imagine that one is compressing an elastic sheet. For supercritical loading P, it can in principle buckle to the left or to the right. But, if there is a bias or imperfection in the original shape and that bias has a non-zero projection in one of the two competitors (left or right), the amplitudes of the original imperfection will be continuously amplified. Such bifurcations are included in the amplitude equations by adding a constant bias term to the mode which has such a bias. In plant phyllotaxis, the bias occurs because the original pattern, for example, the (2,3,5) pattern, as it moves out of the compressed annulus, the
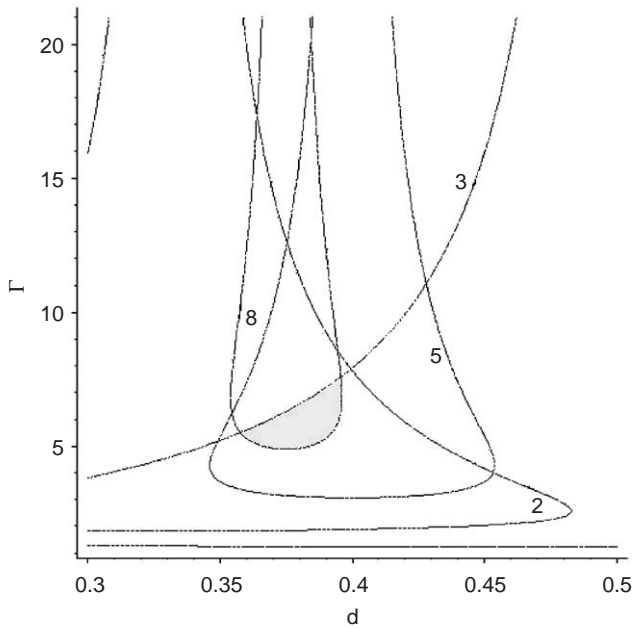
buckling zone, leaves a strong bias on the outer edge. This has two important consequences.

Firstly, prior pattern bias encourages overlapping triads. The reason for this is that, as the new configuration forms in the generative region, the bias arising from the previous pattern, say from modes with circumferential wavenumbers $(2, 3, 5)$, drives through quadratic interactions a new mode whose circumferential wavenumber is the sum $3 + 5 = 8$. Of course, as $2 + 5 = 7$, the mode with circumferential wavenumber 7 can also be driven. In the competition, however, it is the $(2, 3, 5, 8)$ quartet that prevails, particularly when there is a bias in the modes $(2,3,5)$. This is essentially because the 2 mode is so strongly linearly damped.

Secondly, Type II transitions, which are imperfect, are easier for a system to make because, as Γ increases, the original minimum of the energy landscape, which is the starting point for the system at the new value of Γ, is close to the new minimum. So, even though there may be deeper minima in the energy landscape, the one which has the starting point in its basin of attraction is the one which will be realized. This raises an important question. Under what conditions are Type I transitions favored over Type II transitions? The factors are related to the values of the parameters $\frac{P-P_c}{P_c}$, the amount by which the stress is above its critical value, and the curvature C of the generative region. If $\frac{P-P_c}{P_c}$ is too small, then overlapping triads are less favored because the modes at the ends of the two overlapping sequences (such as 2 and 8 in the quartet $(2,3,5,8)$) are very heavily damped. The stationary solutions of the amplitude equations corresponding to overlapping triads disappear. If C is too small, the quadratic interactions are greatly inhibited and then one finds minimizers which consist of ridge-dominated single triads. But, the picture is still incomplete; to give quantitative estimates of the choices of P and C and bias states that give rise to I or II transitions we need to run more simulations.

We now demonstrate with a concrete example a progression with Type II transitions. Take the five active modes (l_m, m), (l_n, n), $(l_m + l_n, m + n)$, $(l_m + 2l_n, m + 2n)$, and $(2l_m + 3l_n, 2m + 3n)$ for $m = 3$, $n = 5$, $l_3 = \frac{2\pi}{\lambda}(1 - 3d)$, and $l_5 = \frac{2\pi}{\lambda}(2 - 5d)$. We analyse the situation in which the stress in the angular direction is 35% above critical (i.e. $P = 2.7$) and there is no stress in the radial direction (i.e. $\chi = 0$). The active set consists of three overlapping triads with amplitudes A_3, A_5, A_8, A_{13}, and A_{21}. For values of Γ, $5 \leqslant \Gamma \leqslant 18$, we calculate the minimizers of $\mathfrak{E}(A_3, A_5, A_8, A_{13}, A_{21}; \lambda, d)$ and plot the energy-minimizing values of d and the amplitudes $|A_3|, |A_5|, |A_8|, |A_{13}|, |A_{21}|$ as functions of Γ in Figs. 26(a and b). We note that both d and the $|A_j|$ change continuously with Γ in (II,2) transitions, and the chosen values of d are, in contrast to the three-mode case, not typically rational numbers. We also note the shapes of the dominant planforms, as plotted in Fig. 27

(a)

(b)
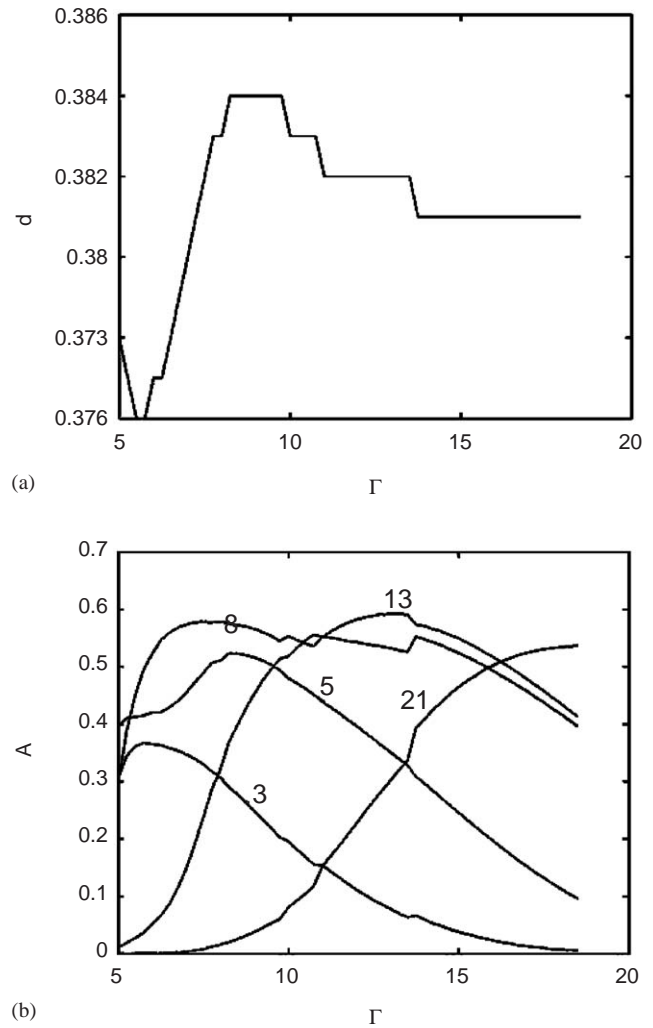
Fig. 26. For the parameters $Q = 3$, $\chi = 0$, $P = 2.7$ and modes with angular wavenumbers 3,5,8,13,21, we calculated (a) The energy-minimizing value of d as a function of Γ in the range $\Gamma = 5 \ldots 18$. (b) The amplitudes of the 3,5,8,13,21 modes in the energy-minimizing configuration as Γ increases.

for increasing Γ. For $\Gamma = 8$, four modes have significant amplitudes, but the center pair 5 and 8 are dominant. The corresponding pattern is that of parallelograms (Fig. 27(a)) that are arranged in two families of 5 and 8 spirals. For $\Gamma \simeq 11$, the three center modes 5,8, and 13 dominate with amplitudes $|A_3|, |A_{21}| \ll |A_5|, |A_8|, |A_{13}|$. Such configurations give rise to the staircase parallelograms seen in Fig. 27(b); the center mode 13 is manifested in the family of 13 spirals. For $\Gamma = 14$, again four modes have significant amplitudes, but now the dominant center pair is 8 and 13; thus in Fig. 27 one sees parallelograms arranged in families of 8 and 13 spirals.

For any choice of Γ, the energy-minimizing choice of amplitudes is such that the amplitudes $|A_n|$ of modes with angular wavenumber $n \simeq \Gamma$ are largest. For example, Fig. 28 shows the energy-minimizing choice
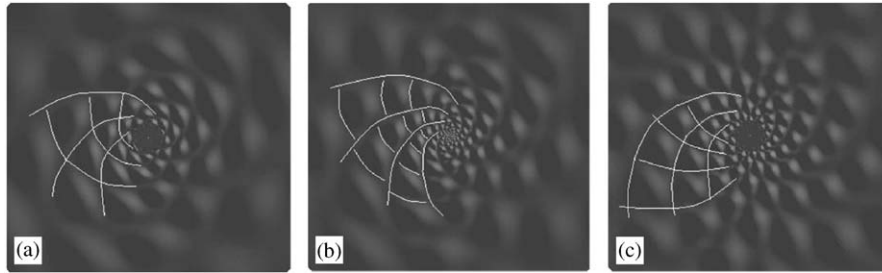
Fig. 27. Deformations $w = a_3 \cos(\vec{k}_3 \cdot x) + a_5 \cos(\vec{k}_5 \cdot x) + a_8 \cos(\vec{k}_8 \cdot x) + a_{13} \cos(\vec{k}_{13} \cdot x) + a_{21} \cos(\vec{k}_{21} \cdot \vec{x})$, where $\vec{x} = (s = \ln(r), \alpha)$ and for values of d and the amplitudes a_j as determined by the experiment of Fig. 26, (a) at $\Gamma = 8$, so that $d = 0.383, a_3 = 0.3, a_5 = 0.52, a_8 = 0.58, a_{13} = 0.3, a_5 = 0$, (b) at $\Gamma = 11$, so that $d = 0.3815, a_3 = 0.15, a_5 = 0.42, a_8 = 0.53, a_{13} = 0.53, a_{21} = 0.15$, and (c) at $\Gamma = 14$, so that $d = 0.3815, a_3 = 0.05, a + 5 = 0.32, a_8 = 0.54, a_{13} = 0.55, a_{21} = 0.38$.
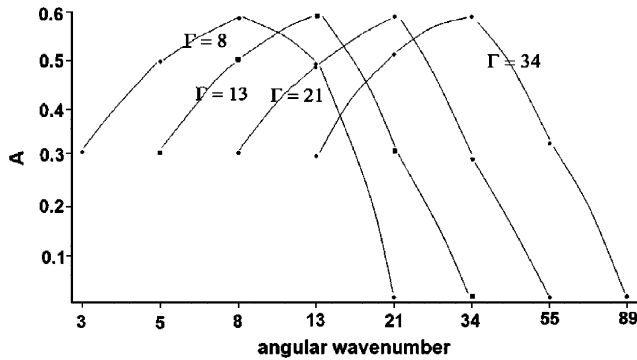
Fig. 28. The five-mode envelope. For the parameters $Q = 3$, $P = 2.7$, $\chi = 0$, and the choice $d = 0.3819$, the energy-minimizing amplitudes A_n of five successive modes in the Fibonacci sequence are plotted for successive values of Γ in the Fibonacci sequence.

Table 2
The predicted relationship between the number of modes with positive amplitudes in a deformation, the planform, and the types of transitions and values of d

Number of modes	Planform	Transition type	d
1	Ridges	(I,1)	Rational
3	Hexagons	(I,1) or (I or II,2)	Rational
4	Parallelograms	(II,2)	Irrational
5	Staircase parallelograms	(II,2)	Irrational

of amplitudes $|A_n|$ of five modes whose angular wavenumbers are consecutive members of the Fibonacci sequence; as Γ increases, the shape of the envelope of the five amplitudes stays approximately the same, but the maximum of the envelope is located at successively higher Fibonacci numbers.

As the final remarks of this subsection, we return to the observations made in Section 1.2 of the introduction, namely

1. The divergence angle $2\pi d$ and the parastichy numbers (m, n) observed in nature are related by $d \simeq \frac{p+q}{m+n}$. Typically, plants with strong ridge configurations have rational values of $d = \frac{p+q}{m+n}$ and undergo (I,1) transitions, whereas those with parallelogram deformations typically have irrational values of $d \simeq \frac{p+q}{m+n}$ and undergo (II,2) transitions.
2. The area $A = 2\pi \frac{\lambda}{g} \Gamma \Lambda^2$ of a newly formed primordium is locally independent of Γ.

Concerning Observation 1, we have shown that energy-minimizing ridge-dominated or hexagon configurations involve triads of the form $\vec{k}_m = (l, m), \vec{k}_n = (-l, n), \vec{k}_{m+n} = (0, m+n)$ and therefore rational values

of $d = \frac{p+q}{m+n}$. For larger values of P, C and under the influence of bias, overlapping triads, irrational values of d, and parallelogram or staircase parallelogram planforms constitute the preferred planform. Only if d and the amplitudes are allowed to change continuously through irrational values can Type II transitions take place; thus, we expect Type I transitions for ridge-dominated planforms and Type II transitions for planforms with overlapping triads. The intermediary case of hexagonal planforms is less clear. For example, if a hexagon $\vec{k}_2 = (l, 2), \vec{k}_3 = (-l, 3), \vec{k}_5 = (0, 5)$ planform forms and moves out to the edge of the generative region, the choices of P, C and the bias determine whether the mode with wavevector $\vec{k}_8$ is present in the new configuration forming in the generative region. Further simulations will be needed to determine the relative importance of the parameters. Table 2 summarizes these conclusions.

Concerning Observation 2, we have theoretically calculated the choices $d \simeq \frac{p+q}{m+n}$, $m + n \simeq \Gamma$, so that $\vec{k}_m = (\frac{2\pi}{\lambda}(q - md), m) \simeq (\frac{2\pi}{\lambda}\frac{q}{\Gamma}, m)$. Also, we have calculated the optimal choice $\vec{k}_m \simeq (1, \frac{\Gamma}{2})$. This gives us that $\frac{2\pi}{\lambda}\frac{q}{\Gamma}$ is of order 1 for all values of Γ, and thus $\frac{\lambda}{g}\Gamma$ is independent of Γ. Recalling that the area of a new primordium is given by $A = 2\pi \frac{\lambda}{g}\Gamma \Lambda^2$, we see that A is also independent of Γ. Notice that, in contrast to (I,1) transitions, in (II,2) transitions the whorl number g never changes; A is kept constant by decreasing the plastochrone ratio/ difference λ.

4.6. Brief comparison with the model of Douady and Couder

It is intriguing to compare the results of the mechanical model presented here with the model of DC as sketched in Section 2.2. A crucial result of both our model and that of DC is that (I,1) transitions (and the patterns of Table 1) are energetically preferred unless bias from previously formed configurations (deformations in our case or arrangements of primordia in the DC paradigm). Thus, we agree with DC that the pattern that is observed on a plant is the result of both the initial pattern that forms and the role that bias plays as the pattern develops. Douady and Couder (1996a–c) present detailed bifurcation diagrams for dependence of the phyllotactic coordinates on their parameter $\Gamma = \frac{d_0}{R}$. For our model, such bifurcation diagrams would necessarily involve both the phyllotactic coordinates and the amplitudes of the various modes. However, one advantage of our model is that it provides a rational and testable explanation for the appearance of bias (see Section 5).

Our model defines primordia of finite size, depending on the natural wavelength of the pattern; Douady and Couder (1996c) suggest that this should be part of any physiological model. The second key component of any physiological model, as suggested by DC, is that it gives the primordia a repulsive or inhibitory action. Instead of this second component, our analysis relies on the interaction of elementary triads of periodic modes. This allows us to examine polygonal planforms and phyllotaxis in the same model. Furthermore, it has potential consequences for differences between Type I and II transitions; in our model, Type II transitions rely on having overlapping triads.

As discussed in Section 2.2, DC interpret their results in terms of optimal packing. As we consider planforms, rather than primordia with a given disk shape, a new definition of packing would be needed to compare results. To interpret the DC definition for a pine cone or cactus with a parallelogram planform, for example, one has to redraw the parallelogram phylla as ellipses.

It is not trivial to compare the model of DC with ours and to determine to what extent the dynamical rules they study are contained in the mechanical model, but this would be an enlightening task for further work.

5. Discussion

In order to frame the summary and conclusions, we pose and address three questions, namely

1. What postdictions, namely explanations of behaviors already observed, and what predictions are consistent with and arise from our theory?

2. What observations should we encourage experimentalists to make?
3. How could, and to what degree should, our picture and the model used to capture the essential ingredients, be improved?

Before answering the first and second questions, we remind the reader again of the point we made in the overview and at the beginning of Section 4. The patterns seen on plants have much in common with patterns seen in laboratory experiments (e.g. Rayleigh–Bénard convection) and other places in nature (e.g. fingerprints and stripes and spots on wildcats); similar macroscopic patterns can form from a variety of microscopic mechanisms that share basic symmetries. Therefore, in considering the ramifications of the mechanical model for plant patterns analysed in this paper, it is important to distinguish between symmetries in the model that could also be present in, for example, reaction–diffusion models, and conclusions that are specific to the mechanical model. The keys to establishing the plausibility of our model are contained in the particular structures of the coefficients $\sigma(l, m)$, $\tau(m, n, m + n)$ of the quadratic and cubic terms in the elastic energy (4.1). The form of (4.1) is universal, but the choice of minimizers depends on the dependence of σ and τ on the wavevectors and other central parameters, Γ, C, χ, and ρ. In Section 4, we discussed this structure and were led to conclusions that we now summarize.

Conclusions, unique to our model, and suggestions for experiments, are as follows:

- The natural wavelength $2\pi\Lambda$ of the pattern is given by $\Lambda^4 = \frac{Eh^3\nu^2}{\kappa + \frac{Eh}{R_{\alpha}^2}}$, which, if $\kappa \leqslant \frac{Eh}{R_{\alpha}^2}$, is approximately the geometric mean $\sqrt{R_{\alpha}h}$ of the tunica thickness and the circumferential radius of curvature. This agrees with an observation of Steele (2000) who also noted that there is a linear relation between Λ^2 and h. To further determine the dependence of $2\pi\frac{\lambda}{g}\Gamma\Lambda^2$ on h, ν and E we suggest a new technique called elastography (McLaughlin and Yoon, 2004) for measuring elastic constants of biological tissue by following elastic waves using ultrasound imaging techniques. This might be used to good effect in the plant context.
- The quadratic coefficient $\sigma(l, m)$ determines a range of active wavevectors, as described in Section 4. It would be useful to map the range of wavevectors observed in plants to check consistency with our model.
- The cubic coefficient $\tau(m, n, m + n)$ and its structure is central to our model. Firstly, our theory predicts that the magnitude of τ is proportional to the circumferential curvature. If it is small, ridges dominate. If it is of order one, triads dominate. Secondly, $\tau(m, n, m + n)$ is a sensitive function of the divergence angle $2\pi d$.

This gives preference to the angles $2\pi\frac{p+q}{m+n}$ that converge to the golden angle as m, n become large Fibonacci numbers. Furthermore, τ depends on the plastochrone ratio λ. This is essential for the choice of non-zero radial wavenumbers for small values of χ. Indeed, recall that τ is maximized at $\lambda = 0$ (so that the corresponding radial wavenumbers are $l = \infty$), and for small χ the linear growth rate σ is maximized for $l = 0$ (that is, $\lambda = \infty$). The energy-minimizing choice of l of order 1 is a compromise between the choices that maximize σ or τ. A theory in which τ is constant as a function of λ predicts triads with wavevectors $\vec{k}_1 \simeq (0, m), \vec{k}_2 \simeq (0, n), \vec{k}_3 = (0, m+n)$; these are not observed in nature.

- Our theory supports the observation that the area $2\pi\frac{\lambda}{g}\Gamma\Lambda^2$ of a primordium is independent of the divergence angle and the size of a plant. As the plant grows (so that Γ increases) and its patterns undergo transitions, we have shown that λ or g change in such a way as to keep $\frac{\lambda}{g}\Gamma$ constant. Either the plastochrone ratio decreases as $\frac{1}{\Gamma}$ (this keeps the radial wavenumber of order one) or the whorl number g changes as Γ. The former can change continuously. Thus, transitions connected with it are more likely to be of second order. The latter changes in integer steps, and these transitions are more likely to be of first order. We emphasize again the remarkable property that in (I,1) transitions one wavevector (both the circumferential and radial wavenumbers) is invariant, and in (II,2) transitions two wavevectors are invariant, except for slight changes in the radial components. The radial structures of adjoining patterns in a large sample of plants should be checked to verify this conclusion.

- Our theory suggests that, if there is no bias of a previously formed configuration, the buckling configuration will be one described by $\vec{k}_1 = (-l, N), \vec{k}_2 = (l, N), \vec{k}_3 = (0, 2N)$ (the wavevectors of the alternating N-whorl) or $\vec{k}_1 = (-l, N), \vec{k}_2 = (l, N+1), \vec{k}_3 = (0, 2N+1)$. Hence, the first pattern to appear on a plant should be described by either of these choices. It would be worthwhile surveying the initial patterns formed in young plants to check this prediction. The choice of N will be such that the ratio of the circumference $2\pi R$ in the generative region to the natural wavelength $2\pi\Lambda$ is either $2N$ or $2N+1$. In addition, the fact that the number of spirals differs by at most one suggests, for example, that a plant that increases up the Lucas sequence $1, 3, 4, 7, 11, \ldots$ will exhibit the parastichy pair $(3, 4)$, and not the parastichy pair $(1, 3)$, when it first forms phylla.

- Our analysis suggests, and the authors' experience supports, the information summarized in Table 2. That is, plants that show strong ridge configurations are likely to undergo (I,1) transitions, whereas plants that show parallelograms are likely to undergo (II,2) transitions. Furthermore, plants with strong rib

configurations are likely to have rational values of d, whereas those with parallelograms are likely to have irrational values of d. These predictions can be checked by a large collection of data in the field.

The $(I, 2)$ and $(I, 0)$ transitions discussed in Sections 1.5.2 and 1.5.4, respectively, have not been fully explained by this model, although we suggest that $(I, 2)$ transitions are associated with planforms that involve a single triad and therefore can have properties of both $(I, 1)$ or $(II, 2)$ transitions, depending on the values of the parameters, particularly the stress, curvature and bias of previous configurations. Douady and Couder (1996c) suggest that the rarely observed $(I, 0)$ transitions can occur when the previous configuration exerts no bias on the newly forming configuration, and this is consistent with our picture.

- Although difficult to perform, experimental modification of the stress parameters P and χ and the curvature constant C could test the following predictions: smaller values of C (i.e. less curvature in the region of pattern formation) or of χ (i.e. less compressive stress in the radial direction) give preference to ribbed patterns, rational values of d, and (I,1) transitions. Larger values of the stress parameter P allow for more active modes, and therefore increase the likelihood of having parallelogram patterns and the (II,2) transitions that yield Fibonacci-like sequences.

Particularly suited to experiments are plants that naturally show transitions between various planforms. For example, pineapples are often described as having hexagonal planforms; a typical pineapple, however, shows regions in which the planform is better described as being a tiling of parallelograms. Thus, pineapples are, in our theory, the result of four-mode deformations with amplitudes $|A_1| \simeq |A_2| \simeq |A_3|$ and $|A_4| \simeq 0$ (in the hexagonal regions) or $|A_2| \simeq |A_3| > |A_1| \simeq |A_4|$ (in the parallelogram regions). Slight changes in the parameters C, P, χ may be able to produce pineapples with purely hexagonal or purely parallelogram planforms. Similar statements hold for totem pole cacti (which show transitions between ridge and hexagonal planforms), and sunflowers which often show transitions between parallelogram and staircase parallelogram planforms or between hexagon and parallelogram planforms. Notice that it is a verifiable prediction of our theory that transitions should be seen to occur between ridges and hexagons, between hexagons and parallelograms, and between parallelograms and staircase parallelograms, but not, for example, between ridges and parallelograms (without a sudden change in the parameters).

- Our theory makes definite and verifiable predictions on whether the dimples of the buckled surface form outward ($C < 0, \rho > 0$; $C > 0, \rho < 0$) or inward ($C > 0, \rho > 0$).

- By combining the notions of bias and the dominance of triad interactions, we are led naturally to Fibonacci sequences. Bias occurs as the old patterns moves, usually outward, relative to the annular zone of compression, and by its presence on the outer fringes of the new buckling zone influences the choice of the next pattern. It would be of interest to check experimentally the premises on which the arguments rely, namely that a pattern, once formed, moves out of the buckling zone and that the new buckling zone feels its influence. Careful measurements of the current position of a given pattern as a function of time and the position of the buckling zone as a function of time would be useful.

Before going on to answer the third question, we want to mention another potential source of the quadratic nonlinearity in the von Kármán equations (and corresponding cubic nonlinearity in the elastic energy) that would allow for triad interactions, but without the d-sensitivity or dependence on λ. Notice that, if $C = 0$, the FvKD equations are invariant under the change $\omega \mapsto -\omega$. The curvature terms break this symmetry when $C \neq 0$ and allow for the differing energy characteristics of hexagons whose centers point up or down. Another asymmetry that would achieve the same effect arises from the fact that the tunica is attached to a corpus foundation; pushing into this foundation may be harder than pushing out from this foundation. In our model, this would be included by adding to the potential $V(\omega) = \kappa\omega^2 + \frac{\gamma}{4}\omega^4$ of the elastic foundation a cubic term so that $V(\omega) = \kappa\omega^2 - \frac{\delta}{3}\omega^3 + \frac{\gamma}{4}\omega^4$. Then, the term $V'(\omega) = \kappa\omega - \delta\omega^2 + \gamma\omega^3$ in the FvKD equations would break the $\omega \mapsto -\omega$ invariance. For $\delta > 0$, this gives energetic preference to hexagons whose centers point away from the corpus. In a model of fingerprint pattern formation, also based on a study of the von Kármán equations, Kücken (2004) notes that such an asymmetry is indeed likely—fingerprints first form in a basal layer beneath the outermost layer in the skin, and differences in the extensibilities of the layers below and beneath this basal layer have been measured. It is interesting to note that hexagonal patterns are found in the fingerprints of some koalas; according to Kücken, it is large asymmetries in the stress tensor that make most of our fingerprints patterns of ridges. There is some evidence that, like fingerprints, primordia are initiated not in the outermost layer of the tunica, but one or two or three cell layers down. Palmer (1998) provides evidence for this in the sunflower, and Lyndon (1994) cites cell division changes in the tissues just below the tunica as the first evidence of primordium formation. Nevertheless, for small values of χ, this possible source of nonlinearity (for which the interaction coefficient τ is the constant δ) gives inaccurate predictions for the choice of the radial wavenumbers for the reasons given above.

We now turn to question number three. To preface our answer, we remind the reader that the magnitudes of the phylla and primordia observed on mature plants are larger than the magnitudes predicted by the shell-buckling theory. We argue, in accordance with Green (1999) and Dumais and Steele (2000), that buckling creates a template, a buckled surface with a non-uniform stress distribution on which further growth can occur due to processes not yet included in the model. An important process we have omitted is a description of the influence that a non-uniform stress distribution causes on the distribution of hormones such as auxin. A non-uniform hormone distribution would lead to a continued growth of the plant surface which would enhance the already existing pattern.

What would this change to our model involve? We should introduce a new variable $H(r, \alpha, t)$ which measures the concentration of the growth hormone relative to its spatial average. It would be driven locally by some functional of the local stress. We suggest $-\nabla^2 f$, the negative of the trace of the stress tensor relative to its spatial average, as it measures the variations in the compressive stress. We note, from the second FvKD equation (3.4) that its Laplacian is proportional to the total Gaussian curvature of the deformed surface. Hormone diffusion may also be a factor (one would need to compare the time it would take the hormone to diffuse across a primordium area with the buckling time) so that $H(r, \alpha, t)$ might satisfy an equation of the form

$$\frac{\partial H}{\partial t} - K_1 H - K_2 \nabla^2 H = -K_3 \nabla^2 f. \qquad (78)$$

In order to include the effect of growth on stress, a modification of the stress-strain relation would be made by including the concentration H in much the same way that one would include temperature if there were temperature variations in the elastic sheet. However, before embarking on the model upgrade, it would be worthwhile first establishing that (i) the buckling is the primary mechanism for plant patterns, and (ii) the relative time-scales associated with the processes of buckling and growth are comparable.

Two features of the upgraded model should be noted. Firstly, if the induced stress by buckling leading to growth leading to more stress feedback loop happens on the buckling time-scale, the winning deformation will not minimize the elastic energy, but rather a modified amplitude polynomial (4.1). Secondly, the growth-stress dynamics will continue after the pattern has left the buckling region.

The connection between non-uniform stress distribution and plant growth subsequent to the initial

pattern-forming stage may have other consequences. We have argued that the determining factor in generating ridge rather than hexagonal and parallelogram patterns is the curvature of the buckling region. Our model deals with the patterns seen close to the north pole, in or close to the generative region; at the north poles of the cacti in Fig. 29(a–c), one observes ridges, hexagons, and parallelograms, respectively. However, for all three of these cacti, ridges become dominant further away from the north pole. One possible source of this change is that the plant tip was flatter when the patterns in the older regions further from the plant tip were formed. However, a similar situation is demonstrated by the paper cactus depicted in Fig. 30. Figs. 30(a and b) show a young paper cactus pad with a parallelogram pattern; the two directions of largest amplitude are marked in Fig. 30(b). Recall that a parallelogram pattern is, in our theory, produced by a sum of four modes with amplitudes $|A_2| \simeq |A_3| > |A_1| \simeq |A_4|$; the spirals marked in Fig. 30(b) correspond to the modes with amplitudes $|A_2|, |A_3|$. As the pad gets larger, as in Fig. 30(c and d), one notices that a third amplitude is getting larger, and, as the pad continues to get larger, a hexagonal pattern develops, as in Fig. 30(e and f). In terms of amplitudes, what has happened is that the amplitude $|A_4|$ has increased, while $|A_1|$ has decreased. Mature paper cactus pads show a hexagonal configuration, as in Fig. 30(g and h). This indicates that different components of the plant's configuration are amplified differently by growth induced by a non-uniform hormone distribution brought about by
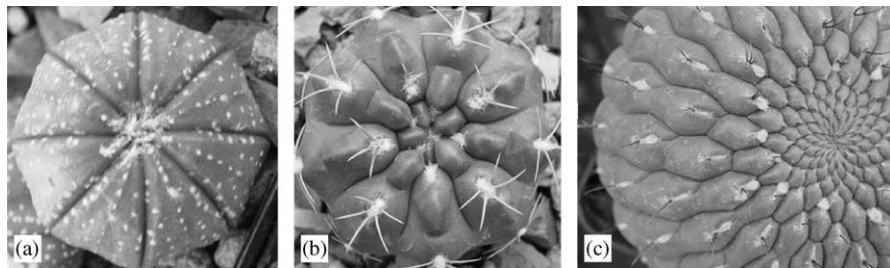

Fig. 29. These cacti show (a) ridge, (b) hexagonal, and (c) parallelogram configurations near their north poles, but further from the north pole, the purely radial deformation becomes more dominant in (b) and (c).
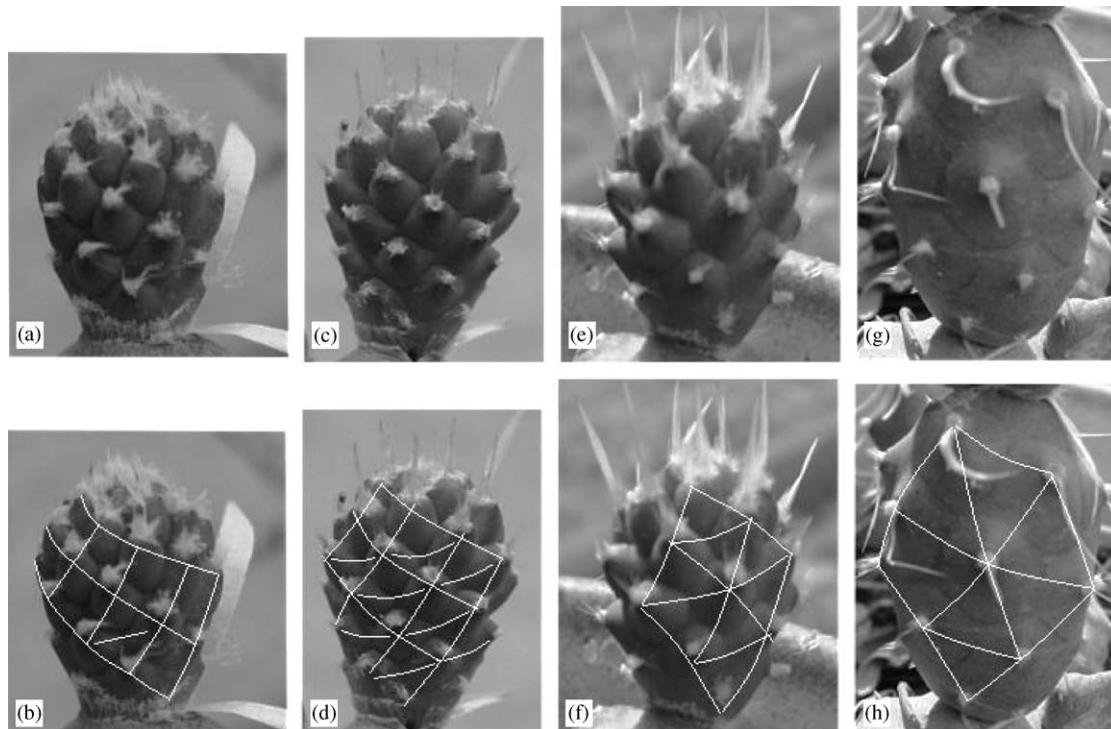

Fig. 30. Parallelograms (a,b), hexagons (g,h) and states in between (c–f) are seen on these pads of a paper cactus.

non-uniform stress. It may be that a slight dominance of the purely radial deformation at the plant tip may induce changes in cell division and cellulose orientation so that this deformation grows further via feedback mechanisms as the patterned plant material differentiates. This leads us to further suggestions for observations and experiments.

- Do the patterns of cellulose orientation and hormone distribution correspond to the ridge, hexagonal, or parallelogram configurations seen on plants, or may, for example, the pattern of cellulose orientation be ridge-like in a plant that exhibits a hexagonal planform? It would be useful to know, for example, in the cactus of Fig. 29(c), if the cellulose orientation or hormone concentrations achieve ridge-like configurations already at the plant tip, where one observes a parallelogram planform, and then influence the observed pattern so that the parallelograms give way to hexagons and then ridges.

- Sunflowers have long been studied by those interested in phyllotaxis, but careful observations of changes between hexagon, parallelogram, and staircase parallelogram planforms (all of which can be observed in sunflowers; see (Palmer, 1998)) have not been made. In the sunflower, the buckling zone moves inward relative to the earlier pattern, so that Γ decreases in time and the patterns which emerge move down,

rather than up, the Fibonacci sequence. Are there also differences in the transitions between the various planforms?

Cell growth patterns within the cactus SAM have been discussed by Mauseth and Niklas (1979) and Niklas and Mauseth (1980). Although these authors do not consider hyperbolic or inverted-sphere geometries, it is interesting that they relate cell division rates in the various zones of the SAM (such as those in Fig. 8) to the geometry, showing that the number of cell divisions in a tunica region is related to the tunica's curvature. The relation of this work to the role of curvature as a measure of nonlinearity in our model is a further question for future work.

Finally, another interesting question is raised by cactus stickers, which may form at the tips, the bottoms, or both places of a surface deformation; see Fig. 31. The maxima of the surface deformation are the regions of greatest compressive stress, and the minima the regions of the least compressive stress, but the details of how stress variation would lead to sticker formation are not known. The relevance of triad interactions to sticker formation is, however, further suggested by the cacti of Fig. 32. Fig. 32(a) shows a cactus with a hexagonal planform; the three periodic deformations that (in our theory) produce it are marked. Notice that the stickers follow along the
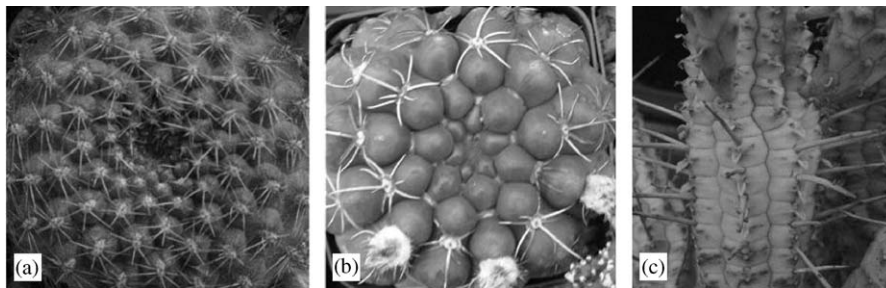
Fig. 31. Stickers can form (a) at the maxima or (b) at the minima of a surface deformation. (c) This succulent has stickers at the minima and leaves at the maxima of its hexagonal deformations.
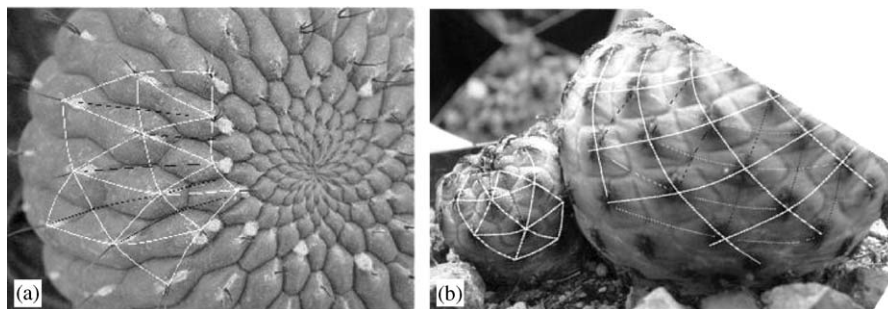
Fig. 32. Stickers mark modes too. (a) The hexagons on this cactus determine three families of spirals, marked in white and corresponding to periodic deformations with wavevectors $\vec{k}_1, \vec{k}_2, \vec{k}_3 = \vec{k}_1 + \vec{k}_2$. The stickers, however, follow the spirals, marked in black, corresponding to the wavevector $\vec{k}_4 = \vec{k}_2 + \vec{k}_3$. (b) The diamonds on this cactus determine two families of spirals, marked strongly in white and corresponding to periodic deformations with wavevectors $\vec{k}_2, \vec{k}_3$. The spirals determined by the wavevector $\vec{k}_1 = \vec{k}_3 - \vec{k}_2$ are marked faintly in white, and stickers follow along the directions determined by the wavevector $\vec{k}_4 = \vec{k}_2 + \vec{k}_3$, as marked in black.

lines that would mark the directions of the fourth periodic deformation whose amplification would produce a parallelogram pattern. In fact, near the very center of the plant the planform consists of parallelograms. The marked hexagonal configuration may then be a result of a change in an originally parallelogram pattern as described above, with evidence of the former presence of a fourth mode left by the stickers that formed. Again, to determine the biological differences that lead to the differences between these two plants, one needs to know the form of the pattern as it develops in the generative region and the subsequent changes in the pattern as the plant grows.

Acknowledgements

Appendix A. The phyllotactic vector sequences

Transitions of type (II,2) lead to a sequence of lattice generators. If a plant begins with a lattice generated by $\vec{\omega}_m = \frac{1}{g}(m\lambda, 2\pi(md - q))$, $\omega_n = \frac{1}{g}(n\lambda, 2\pi(nd - p))$ with $d \simeq \frac{p+q}{m+n}$, a (I or II,2) transition produces a new lattice generated by $\vec{\omega}_n = \frac{1}{g}(n\lambda, 2\pi(nd - p))$, $\omega_{m+n} = \vec{\omega}_m + \vec{\omega}_n = \frac{1}{g}((m+n)\lambda, 2\pi((m+n) - (p+q)d))$, and $d \simeq \frac{p+q}{m+n}$. Note that the only change in the lattice is that d has changed. After a sequence of (I or II,2) transitions occur, the lattice generators move up the *phyllotactic lattice generator sequence* (PLGS)

$$\vec{\omega}_m = \frac{1}{g}(m\lambda, 2\pi(md - q)),$$

$$\vec{\omega}_n = \frac{1}{g}(n\lambda, 2\pi(nd - p)),$$

$$\vec{\omega}_{m+n} = \frac{1}{g}((m+n)\lambda, 2\pi((m+n)d - (p+q))),$$

$$\vec{\omega}_{m+2n} = \frac{1}{g}((m+2n)\lambda, 2\pi((m+2n)d - (2p+q))),$$

$$\vec{\omega}_{2m+3m} = \frac{1}{g}((2m+3n)\lambda, 2\pi((2m+3n)d - (3p+2q))),$$

$$\vdots \qquad \vdots \tag{79}$$

Note that, for any two consecutive vectors

$$\vec{\omega}_M = \frac{1}{g}(M\lambda, 2\pi(Md - Q)), \quad \vec{\omega}_N = \frac{1}{g}(N\lambda, 2\pi(Nd - P))$$

in this sequence, $PM - QN = \pm\gcd(M,N) = \pm g$, and the chosen divergence angle is $d \simeq \frac{P+Q}{M+N}$. The dual

phyllotactic wavevector sequence (PWS) reads

$$\vec{k}_m = \left(\frac{2\pi}{\lambda}(q - md), m\right),$$

$$\vec{k}_n = \left(\frac{2\pi}{\lambda}(p - nd), n\right),$$

$$\vec{k}_{m+n} = \left(\frac{2\pi}{\lambda}(p + q - (m+n)d), m + n\right),$$

$$\vec{k}_{m+2n} = \left(\frac{2\pi}{\lambda}(2p + q - (m+2n)d), m + 2n\right),$$

$$\vec{k}_{2m+3m} = \left(\frac{2\pi}{\lambda}(3p + 2q - (m+3n)d), 2m + 3n\right),$$

$$\vdots \qquad \qquad \vdots \tag{80}$$

For example, taking $m = n = g$ for some integer g, we obtain the sequence

$$\vec{\omega}_g = \frac{1}{g}(g\lambda, 2\pi(gd - 1)),$$

$$\vec{\omega}'_g = \frac{1}{g}(g\lambda, 2\pi(gd)),$$

$$\vec{\omega}_{2g} = \frac{1}{g}(2g\lambda, 2\pi(2gd - 1)),$$

$$\vec{\omega}_{3g} = \frac{1}{g}(3g\lambda, 2\pi(3gd - 1)),$$

$$\vec{\omega}_{5g} = \frac{1}{g}(5g\lambda, 2\pi(5gd - 2)),$$

$$\vdots \qquad \vdots \tag{81}$$

which we will call the *special phyllotactic lattice generator sequence* (SPLGS). For consecutive vectors $\vec{\omega}_j = \frac{1}{g}(m\lambda, 2\pi(md - q))$, $\vec{\omega}_{j+1} = \frac{1}{g}(n\lambda, 2\pi(nd - p))$ of this sequence, $pm - qn = \pm\gcd(m,n) = \pm g$. The dual wavevector sequence reads

$$\vec{k}_g = \left(\frac{2\pi}{\lambda}(1 - gd), g\right),$$

$$\vec{k}'_g = \left(\frac{2\pi}{\lambda}(-gd), g\right),$$

$$\vec{k}_{2g} = \left(\frac{2\pi}{\lambda}(1 - 2gd), 2g\right),$$

$$\vec{k}_{3g} = \left(\frac{2\pi}{\lambda}(1 - 3gd), 3g\right),$$

$$\vec{k}_{5g} = \left(\frac{2\pi}{\lambda}(2 - 5gd), 5g\right),$$

$$\vdots \qquad \vdots \tag{82}$$

These last two sequences encode both the Fibonacci sequence if $g = 1$ and the double Fibonacci sequence $2, 2, 4, 6, 10, \ldots$ if $g = 2$. These are the two most commonly observed sequences in nature; according to the data collected by Jean (1994). about 92% of plants with spiral phyllotaxis exhibit the Fibonacci sequence,

and about 5% exhibit the double Fibonacci sequence. Another approximately 2% of plants exhibit the Lucas sequence $1, 3, 4, 7, \ldots$ encoded by choosing $m = 1, n = 3$ in Eqs. (79) and (80). These data, however, do not indicate what the original choice of m, n was on the plants. For example, a plant that starts with $m = 1, n = 1$ and continues up the sequence (79) will exhibit the Fibonacci sequence, but so will a plant that starts with any other consecutive Fibonacci numbers, such as $m = 1, n = 2$.

For a plant that exhibits the Fibonacci sequence, the divergence angle $2\pi d = 2\pi \frac{p+q}{m+n}$ will approach the golden angle $\frac{2\pi}{\beta^2}$, where β, the positive zero of $x^2 - x - 1$, is the golden number. To see this, denote the kth Fibonacci number by f_k. For $m = f_j$, $n = f_{j+1}$, what is $\frac{p+q}{m+n}$? By induction on j, prove that $f_{j-1}f_j - f_{j-2}f_{j+1} = \pm 1 = \gcd(m, n)$. The numbers $\frac{p+q}{m+n}$, then, can be chosen to be $\frac{f_{j-1}+f_{j-2}}{f_j+f_{j+1}} = \frac{f_j}{f_{j+2}}$ (the other possible p, q choices yield similar results). It turns out that $\frac{f_j}{f_{j+2}} \to \frac{1}{\beta^2} = \frac{1}{\beta+1}$ as $j \to \infty$. To show this, note that $\frac{f_{j+2}}{f_j} = \frac{f_j+f_{j+1}}{f_j} = \frac{f_{j+1}}{f_j} + 1$, so that it suffices to show that $\frac{f_{j+1}}{f_j} \to \beta = \beta^2 - 1$ as $j \to \infty$; that is, that $(\frac{f_{j+2}}{f_j})^2 - (\frac{f_{j+2}}{f_j}) - 1 \to 0$ as $j \to \infty$. To this end, calculate that $(\frac{f_{j+1}}{f_j})^2 - (\frac{f_{j+1}}{f_j}) - 1 = \frac{f_{j+1}^2 - f_{j+1}f_j - f_j^2}{f_j^2}$, and prove by induction on j that $f_{j+1}^2 - f_{j+1}f_j - f_j^2 = \pm 1$ for all j. Most divergence angles observed in nature are therefore approximately the golden angle $D = \frac{2\pi}{\beta^2}$.

References

Atanakovich, T.M., Guran, A., 2000. Theory of Elasticity for Scientists and Engineers. Birkhaeuser, Boston.

Barabé, D., Adler, I., Jean, R.V., 1997. A history of the study of phyllotaxis. Ann. Bot. 80, 231–244.

Bonnet, C., 1754. Recherches sur l'Usage des Feuilles dans les Plantes. Neuchatel.

Braun, A., 1831. Vergleichende Untersuchung über die Ordnung der Schuppen an den Tannenzapfen als Einleitung zur Untersuchung der Blattstellung überhaupt. Nova Acta Ph. Med. Acad. Cesar Leop. Carol. Nat. Curiosorum 15, 195–402.

Bravias, L., Bravais, A., 1837. Essai sur la disposition des feuilles curveseriees. Ann. Sci. Nat. Bot. Biol. Veg. 7, 42–110.

Busse, F.H., 1967. On the stability of two-dimensional convection in a layer heated from below. J. Math. Phys. 46, 140–150.

Douady, S., Couder, Y., 1992. Phyllotaxis as a physical self-organizing growth process. Phys. Rev. Lett. 68, 2098–2101.

Douady, S., Couder, Y., 1996a. Phyllotaxis as a dynamical self-organizing process, Part I: the spiral modes resulting from time-periodic iterations. J. Theor. Biol. 178, 255–274.

Douady, S., Couder, Y., 1996b. Phyllotaxis as a dynamical self-organizing process, Part II: the spontaneous formation of a periodicity and the coexistance of spiral and whorled patterns. J. Theor. Biol. 178, 275–294.

Douady, S., Couder, Y., 1996c. Phyllotaxis as a dynamical self-organizing process, Part III: the simulation of the transient regimes of ontogeny. J. Theor. Biol. 178, 295–312.

Dumais, J., Kwiatkowska, D., 2001. Analysis of surface growth in shoot apices. The Plant J. 31 (2), 229–241.

Dumais, J., Steele, C.R., 2000. New evidence for the role of mechanical forces in the shoot apical meristem. J. Plant Growth Reg. 19, 7–18.

Fleming, A.J., McQueen-Mason, S., Mandel, T., Kuhlemeier, C., 1997. Induction of leaf primordia by the cell wall protein expansin. Science 276, 1415–1418.

Gould, P.L., 1999. Analysis of Plates and Shells. Prentice-Hall, Upper Saddle River.

Green, P.B., 1992a. Pattern formation in shoots: a likely role for minimal energy configurations of the tunica. Int. J. Plant. Sci. 153, 59–75.

Green, P.B., 1992b. Expression of form and pattern in plants: a role for biophysical fields. Cell Dev. Biol. 7, 903–911.

Green, P.B., 1999. Expression of pattern in plants: combining molecular and calculus-based paradigms. Am. J. Bot. 86 (8), 1059–1076.

Green, P.B., Steele, C.S., Rennich, S.C., 1998. How plants produce patterns. A review and a proposal that undulating field behavior is the mechanism. In: Jean, R.V., Barabé, D. (Eds.), Symmetry in Plants. World Scientific, Singapore, pp. 359–392.

Harrison, L.F., 1987. Mini review: what is the status of reaction–diffusion theory thiry-five years after Turing? J. Theor. Biol. 125, 384.

Hejnowicz, Z., Sievers, A., 1996. Tissue stresses in organs of herbaceous plants, III: elastic properties of the tissues of the sunflower capitulum. J. Exp. Biol. 47, 519–528.

Hernández, L.H., Green, P.B., 1993. Transductions for the expression of structural pattern: analysis in sunflower. The Plant Cell 5, 1725–1738.

Hernández, L.H., Havelange, A., Bernier, G., Green, P.B., 1991. Growth behavior of single epidermal cells during flower formation: sequential scanning electron micrographs provide kinematic patterns for Anagallis. Planta 185, 139–147.

Hofmeister, W., 1868. Allgemeine Morphologie der Gewachse, Handbuch der Physiologischen Botanik. Engelmann, Leipzig.

Jean, R., 1994. Phyllotaxis. Cambridge University Press, Cambridge.

Koiter, W.T., 1963. Proc. K. Ned. Akad. Wet. B Phys. Sci. 66, 263.

Kücken, M., 2004. On the Formation of Fingerprints. Ph.D. Dissertation, University of Arizona.

Kücken, M., Newell, A.C., 2004. The formation of fingerprints. Europhys. Lett. 68 (1), 141–146.

Kwiatkowska, D.K., 1995. Ontogenetic changes of phyllotaxis in Anagallis Arvensis. L. Acta Soc. Bot. Pol. 64 (4), 319–325.

Kwiatkowska, D.K., 2004. Structural integration at the shoot apical meristem: models, measurements, and experiments. Am. J. Bot. 91 (9), 1277–1293.

Kwiatkowska, D., Dumais, J., 2003. Growth and morphogenesis at the vegetative shoot apex of Anagallis arvensis L. J. Exp. Bot. 54 (387), 1585–1595.

Kwiatkowska, D., Florek-Marwitz, J., 1999. Ontogenetic variation of phyllotaxis and apex geometry in vegetative shoots of Sedum Maximum (L.). Hoffm. Acta Soc. Bot. Pol. 68 (2), 85–95.

Lange, C.G., Newell, A.C., 1971. The post-buckling problem for thin elastic shells. SIAM J. Appl. Math. 605–629.

Lange, C.G., Newell, A.C., 1974. Spherical shells like hexagons; cylinders like diamonds—Part 1. J. Appl. Mech. No. 73-APM-7.

Levitov, L.S., 1991a. Energetic approach to phyllotaxis. Europhys. Lett. 14, 533–539.

Levitov, L.S., 1991b. Phyllotaxis of flux lattices in layered super-conductors. Phys. Rev. Lett. 66, 224–227.

Livio, M., 2002. The Golden Ratio. Broadway Books.

Lyndon, R. F., 1994. Control of organogenesis at the shoot apex. Tansley Review No. 74. New Phytol. 74, 1–18.

Mauseth, J.D., Niklas, K.J., 1979. Constancy of relative volumes of zones in shoot apical meristems in Cactaceae: implications

concerning meristem size, shape, and metabolism. Amer. J. Bot. 66 (8), 933–939.

McLaughlin, J.R., Yoon, J.R., 2004. Unique indentifiability of elastic parameters from time independent interior displacement measurement. Inverse Problems 20, 25–46.

Meicenheimer, R.D., 1998. Deccusate to spiral transitions in phyllotaxis. In: Jean, R.V., Barabé, D. (Eds.), Symmetry in Plants. World Scientific, Singapore, pp. 125–143.

Meicenheimer, R.D., Zagorska-Marek, B., 1989. Consideration of the geometry of the phyllotaxis triangular unit and discontinuous phyllotactic transitions. J. Theor. Biol. 139, 359–363.

Meinhardt, H., Koch, A.J., Bernasconi, G., 1998. Models of pattern formation applied to plant development. In: Jean, R.V., Barabé, D. (Eds.), Symmetry in Plants. World Scientific, Singapore, pp. 723–758.

Niklas, K.J., Mauseth, J.D., 1980. Simulations of cell dimensions in shoot apical meristems: implications concerning zonate apices. Amer. J. Bot. 67 (5), 715–732.

Palmer, J.H., 1998. The physiological basis of pattern generation in the sunflower. In: Jean, R.V., Barabé, D. (Eds.), Symmetry in Plants. World Scientific, Singapore, pp. 145–169.

Priestly, J.H., 1928. The meristemic tissues of the plant. Ann. Bot. 3, 1–20.

Reinhardt, D., Pesce, E.-R., Stieger, P., Mandel, T., Baltensperger, K., Bennett, M., Traas, J., Friml, J., Kuhlemeier, C., 2003. Regulation of phyllotaxis by polar auxin transport. Nature 426, 255–260.

Richards, R.J., 1948. The geometry of phyllotaxis and its origin. Symp. Soc. Exp. Biol. 2, 217–245.

Richards, R.J., 1951. Phyllotaxis: its quantitative expression and relation to growth in the apex. Philos. Trans. R. Soc. London B235, 509–564.

Rutishauser, R., 1998. Plastochrone ratio and leaf arc as parameters of a quantitative phyllotactic analysis in vascular plants. In: Jean, R.V., Barabé, D. (Eds.), Symmetry in Plants. World Scientific, Singapore, pp. 171–212.

Sachs, T., 1991. Pattern Formation in Plant Tissues. Cambridge University Press, Cambridge.

Schimper, C.F., 1830. Beschreibung des *Symphytum Zeyheri* und seiner zwei deutschen Verwandten der *S. Bulborum Schimp* und *S. tuberosum Jacq*. Geiger's Mag. Pharm. 29, 1–92.

Schimper, C.F., 1836. Geometrische Anordnug der um eine Axe periferischen Blattgebilde. Verhandl. Schez. Naturf. Ges. 21, 113–117.

Schüpp, O., 1914. Wachstum und formwechsel des sprossvegetationspunktes der angiospermen. Ber. dtsch. bot. Ges. 32, 328–339.

Schwendener, S., 1874. Das mechanische Prinzip in anatomischen Bau der Monocotyledonen mit vergleichenden Ausblicken auf die übrigen Pflanzenklassen. Engelmann, Leipzig.

Schwendener, S., 1878. Mechanischer Theorie der Blattstellungen. Engelmann, Leipzig.

Schwendener, S., 1883. Zur theorie der blattstellungen. Sitzungsber. Akad. Wiss. Berl. 741–773.

Schwendener, S., 1909. Theorie der Blattstellungen, Mechanische Probleme der Botanik. Engelmann, Leipzig.

Selker, J.M.L., Steucek, G.L., Green, P.B., 1992. Biophysical mechanisms for the morphogenetic progressions at the shoot apex. Dev. Biol. 153, 29–43.

Shipman, P.D., 2004. Plant patterns. Ph. D. Dissertation, University of Arizona.

Shipman, P.D., Newell, A.C., 2004. Phyllotactic patterns on plants. Phys. Rev. Lett. 92, 168102.

Snow, M., Snow, R., 1952. Minimum areas and leaf determination. Proc. R. Soc. B 139, 545–566.

Steele, C.R., 2000. Shell stability related to pattern formation in plants. J. Appl. Mech. 67, 237–247.

Steucek, G.L., Selker, J.L., Reif, W.E., 1992. Architecture of the plant shoot apex. In: Reiner, R. (Ed.), Natürliche Konstruktionen. Kurz and Co., Stuttgart.

Turing, A.M., 1952. The chemical basis of morphogenesis. Philos. Trans. R. Soc. London B 237, 37–72.

van Iterson, G., 1907. Mathematische und microscopisch-anatomische Studien ueber Blattstellungen, nebst Betraschungen ueber den Schalenbau der Miloiolinen. Gustav-Fisher-Verlag, Jena.

Wainwright, S.A., Biggs, W.D., Currey, J.D., Gosline, J.M., 1976. Mechanical Design in Organisms. Princeton University Press, Princeton, NJ.